

# A ballistics analysis of the Deep Impact ejecta plume: Determining Comet Tempel 1's gravity, mass, and density

James E. Richardson<sup>a,\*</sup>, H. Jay Melosh<sup>b</sup>, Carey M. Lisse<sup>c</sup>, Brian Carcich<sup>d</sup>

<sup>a</sup> Center for Radiophysics and Space Research, Cornell University, Ithaca, NY 14853, USA

<sup>b</sup> Lunar and Planetary Laboratory, University of Arizona, Tucson, AZ 85721-0092, USA

<sup>c</sup> Planetary Exploration Group, Space Department, Johns Hopkins University Applied Physics Laboratory, 11100 Johns Hopkins Road, Laurel, MD 20723, USA

<sup>d</sup> Center for Radiophysics and Space Research, Cornell University, Ithaca, NY 14853, USA

Received 31 March 2006; revised 8 August 2007

Available online 15 August 2007

## Abstract

In July of 2005, the Deep Impact mission collided a 366 kg impactor with the nucleus of Comet 9P/Tempel 1, at a closing speed of  $10.2 \text{ km s}^{-1}$ . In this work, we develop a first-order, three-dimensional, forward model of the ejecta plume behavior resulting from this cratering event, and then adjust the model parameters to match the flyby-spacecraft observations of the actual ejecta plume, image by image. This modeling exercise indicates Deep Impact to have been a reasonably “well-behaved” oblique impact, in which the impactor-spacecraft apparently struck a small, westward-facing slope of roughly  $1/3$ – $1/2$  the size of the final crater produced (determined from initial ejecta plume geometry), and possessing an effective strength of not more than  $\bar{Y} = 1$ – $10 \text{ kPa}$ . The resulting ejecta plume followed well-established scaling relationships for cratering in a medium-to-high porosity target, consistent with a transient crater of not more than 85–140 m diameter, formed in not more than 250–550 s, for the case of  $\bar{Y} = 0 \text{ Pa}$  (gravity-dominated cratering); and not less than 22–26 m diameter, formed in not less than 1–3 s, for the case of  $\bar{Y} = 10 \text{ kPa}$  (strength-dominated cratering). At  $\bar{Y} = 0 \text{ Pa}$ , an upper limit to the total ejected mass of  $1.8 \times 10^7 \text{ kg}$  ( $1.5$ – $2.2 \times 10^7 \text{ kg}$ ) is consistent with measurements made via long-range remote sensing, after taking into account that 90% of this mass would have stayed close to the surface and then landed within 45 min of the impact. However, at  $\bar{Y} = 10 \text{ kPa}$ , a lower limit to the total ejected mass of  $2.3 \times 10^5 \text{ kg}$  ( $1.5$ – $2.9 \times 10^5 \text{ kg}$ ) is also consistent with these measurements. The expansion rate of the ejecta plume imaged during the look-back phase of observations leads to an estimate of the comet's mean surface gravity of  $\bar{g} = 0.34 \text{ mm s}^{-2}$  ( $0.17$ – $0.90 \text{ mm s}^{-2}$ ), which corresponds to a comet mass of  $m_t = 4.5 \times 10^{13} \text{ kg}$  ( $2.3$ – $12.0 \times 10^{13} \text{ kg}$ ) and a bulk density of  $\rho_t = 400 \text{ kg m}^{-3}$  ( $200$ – $1000 \text{ kg m}^{-3}$ ), where the large high-end error is due to uncertainties in the magnitude of coma gas pressure effects on the ejecta particles in flight.

© 2007 Elsevier Inc. All rights reserved.

**Keywords:** Comet Tempel-1; Comets, nucleus; Cratering; Impact processes

## 1. Introduction

On July 4, 2005, the Deep Impact mission successfully collided a 366 kg impactor-spacecraft with the surface of 6 km diameter Comet 9P/Tempel 1, at an oblique angle of about  $56^\circ$  from the regional surface normal and a collision speed of  $10.2 \text{ km s}^{-1}$  (A'Hearn et al., 2005b). This impact produced a cratering event which was directly observed by a flyby-spacecraft which passed within 500 km of the comet, in two

viewing windows: an approach phase of observations, made from 0 to 800 s following the time of impact; and a look-back phase of observations, made from 45 to 75 min following the time of impact (A'Hearn et al., 2005a). The solid-particle ejecta plume produced by this cratering event, first visible at  $\sim 340 \text{ ms}$  after the impact (Medium Resolution Instrument (MRI) image MV9000910.069), rapidly emerged from the impact site and expanded to form a highly visible, cone-shaped cloud of launched particles, which dominates many of the subsequent images (Fig. 1). This prominent plume remained visibly “attached,” i.e., in very close proximity to the comet's surface as it rapidly extended longitudinally (away from the comet's sur-

\* Corresponding author. Fax: +1 607 255 3910.

E-mail address: [richardson@astro.cornell.edu](mailto:richardson@astro.cornell.edu) (J.E. Richardson).

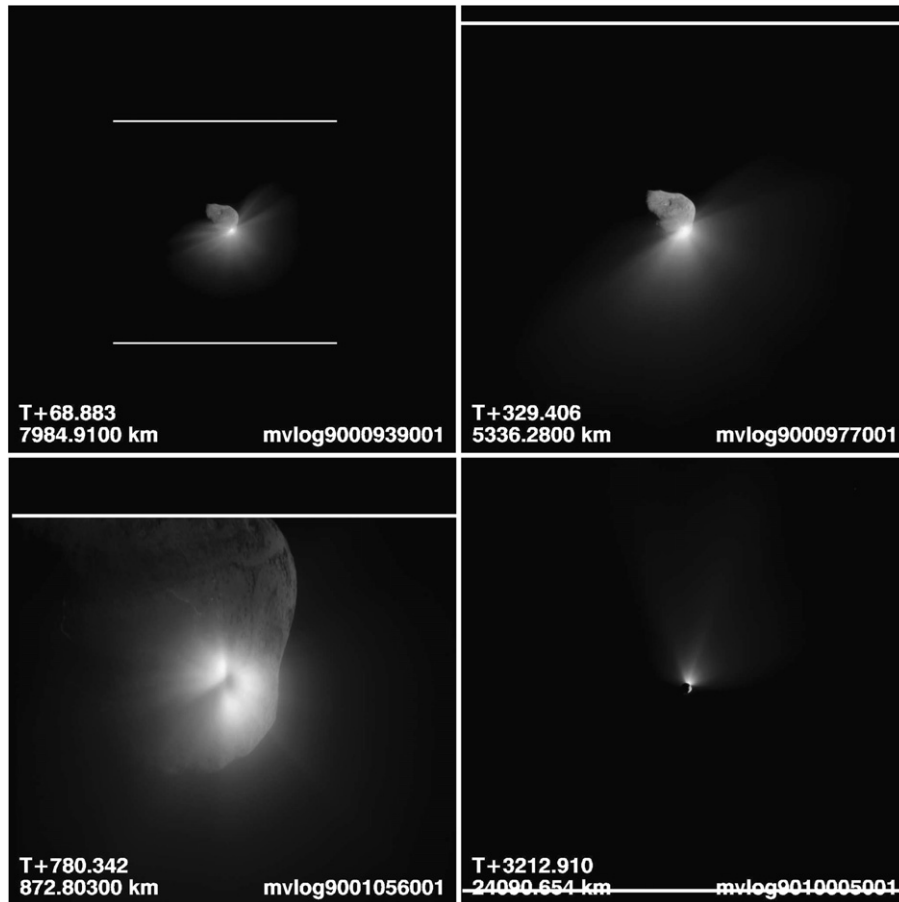


Fig. 1. The four viewing phases of the Deep Impact ejecta plume: imaged by the Medium Resolution Instrument (MRI). (*Upper left*) Early interior view (1): for the first 2 min after impact, the flyby-spacecraft viewed the full interior of the hollow ejecta cone, with ejecta rays extending in all directions. (*Upper right*) Edge-on view (2): from about 2 to 9 min after impact, the flyby-spacecraft viewed the upper left (west) side of the ejecta cone nearly edge-on, while the lower right (east) side of the ejecta cone interior was viewed nearly broad-side. (*Lower left*) Late interior view (3): from about 9 to 13 min after impact, the flyby-spacecraft viewed the deep interior of the ejecta cone, including the dark oval of the plume base. (*Lower right*) Look-back profile view (4): from about 45 to 75 min after impact, the flyby-spacecraft viewed the ejecta cone in near-profile, with its base just hidden behind the limb of the comet.<sup>1</sup>

face) and expanded laterally (along the comet's surface) over the course of the observations made by the flyby-spacecraft.

During the first 800 s following the impact, the hollow interior of the ejecta plume was viewed as the flyby-spacecraft approached the comet. During the look-back phase of observations, 45–75 min following the impact, the conical exterior of the ejecta plume was viewed as the spacecraft departed the comet (A'Hearn et al., 2005b). These later, look-back images permit measurements of the ejecta plume's lateral expansion rate over a time span of nearly half an hour, and thus provide a quantitative means for estimating the magnitude of Tempel 1's gravity field. This is because the observed ejecta plume consisted of billions of tiny ejecta particles, each one following its own ballistic trajectory under the influence of Tempel 1's gravity field, and as such, the lateral expansion rate of the collective ejecta plume is also a function of the comet's gravity field (Melosh, 2001). When coupled with a shape model for

Comet Tempel 1 (Thomas et al., 2007), a reasonable gravity estimate for Tempel 1 also permits an estimate of the comet's mass and bulk density.

This gravity estimate for Tempel 1 is made by developing a first-order, three-dimensional, forward model of the cratering event's ejecta plume behavior, and then adjusting the parameters of this model (over many iterations) to match the spacecraft observations of the actual plume behavior, image by image (Richardson et al., 2005). This forward model is, in turn, based upon well-established impact cratering event scaling relationships, which are described in detail in the following sections. In addition to gravity and density estimates for Comet Tempel 1, this model also permits us to estimate the particle velocity distribution and total mass ejected by the impact, and obtain a rough estimate of the comet's surface strength at the impact site.

### 1.1. The impact cratering process

Before describing the model developed for this work, it will be helpful to review the basic stages of the impact cratering process and describe how these stages relate to the observa-

<sup>1</sup> All included images have been re-centered on the impact site; re-scaled to the full instrument field-of-view; and are labeled with the time after impact (in seconds), the spacecraft range to the comet (in km), and the image number (sans decimal point).

tions conducted by the Deep Impact flyby-spacecraft. In our description, an impact cratering event can be loosely divided into three stages: a coupling stage, an excavation stage, and a modification stage. Below is a brief synopsis of each of these stages—detailed descriptions of the cratering process can be found in Chapman and McKinnon (1986) and Melosh (1989).

The coupling stage of an impact event begins the instant the impactor touches the target surface. During the coupling stage, the kinetic energy and momentum of the impactor are transmitted, or coupled, into the target material as the impactor pushes into and rapidly accelerates the target material, while at the same time the target material rapidly deforms and decelerates the impactor. These rapid velocity changes produce two shock-waves, which begin at the point of contact between impactor and target, and then rapidly propagate both forward into the target material and backward into the impactor. It is the forward propagating, hemispherical, compressive shock-wave in the target material that transmits the majority of the energy initially contained in the impactor to the target material. This shock-wave is followed almost immediately by a rarefaction-wave, which is the reflection of the compressive shock-wave off the free surface of the target. This coupling-phase energy transfer from impactor to target takes place within a region of the target of roughly a few times the volume of the impactor, and in a time of order  $d/v_i$ , where  $d$  is the diameter of the impactor and  $v_i$  is its velocity. In the case of the Deep Impact experiment, this amounts to the deposition of  $\sim 1.9 \times 10^{10}$  J of energy into a target volume of order 1–10 cubic meters in size, and in only 0.1–1 ms (depending upon penetration depth). Thus, this first stage of the cratering process was not directly observable by the flyby-spacecraft, which at that time had an image spatial resolution of only 35 m per pixel and a time resolution of 59 ms (A'Hearn et al., 2005a).

In the immediate vicinity of an impact site, shock pressures will greatly exceed the yield strength of the target material, while the amount of internal energy deposited in the target will greatly exceed that necessary to vaporize and/or melt this material (called shock heating). Additionally for Deep Impact, crushing of the highly porous cometary surface may also have transformed a large amount of kinetic energy into internal energy. The result of this rapid crushing and heating is the creation and expulsion of a rapidly expanding bubble of vaporized target material and entrained melt droplets from the impact site, which moves quickly away at speeds near to that of the original impactor. This marks the beginning of the excavation stage of the cratering process. The amount of material vaporized and melted by a given impact is highly dependent upon the nature of the target material, but in the case of the Deep Impact event, this amount was expected to be on the order of several impactor masses and encompass a volume around the impact site of a few impactor radii in extent (the impactor was about 1 m in diameter). The vapor plume produced by the Deep Impact experiment is clearly visible in MRI images MV9000910.067–MV9000910.077, and is the topic of a separate analysis by Melosh et al. (2006).

Outside of the vaporization and melt zone, the rapid compression and rarefaction produced by the passage of the ex-

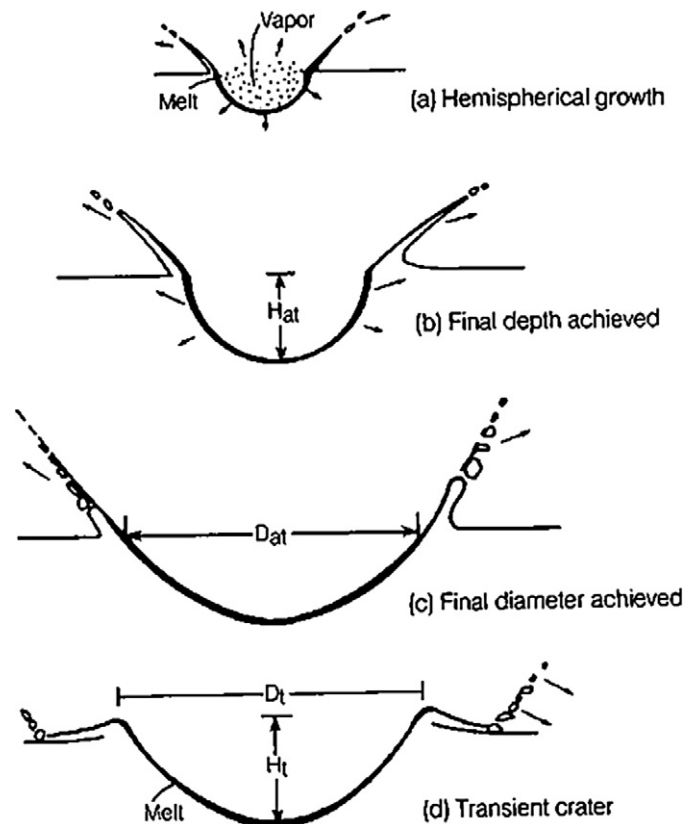


Fig. 2. The crater excavation stage shown in four steps (figure taken from Melosh, 1989). This stage begins with the upward release of the vapor plume, simultaneous with the establishment of a hydrodynamic flow of solid material, which excavates the bowl of the crater. This solid-ejecta flow forms an inverted, hollow cone of ballistically launched particles, attached at its base to the expanding rim of the growing crater. The growth of the crater and the launch of additional material into the ejecta plume is halted by either the downward force of gravity, the residual strength of the target material, material viscosity forces, or a combination of these three factors.

panding (and weakening) shock front does two things: first, it severely fractures and damages the target material as it passes, and second, it injects a large amount of residual kinetic energy into this material and as such, sets up a hydrodynamic (fluid-like) flow of solid particles which excavates the crater. This process is depicted pictorially in Fig. 2, in which the excavation flow is shown opening up a paraboloid bowl in the target, whose depth is roughly 1/3 its diameter, and from which material moves upward and radially outward to form a hollow, conical ejecta plume. As the shock front in the target expands away from the impact site (advancing far ahead of the excavation flow-field that it sets up), it weakens rapidly, such that the amount of damage done to the target material, and the amount of kinetic energy deposited in this material, rapidly falls off with increasing distance from the impact site. Therefore, although the crater initially grows quite quickly and the early ejecta are launched at high velocities, the crater growth rate falls off rapidly, accompanied by rapidly slowing ejecta velocities, with increasing distance from the impact site. The excavation flow finally comes to a halt, and the “transient” crater formed, when the upward and outward, hydrodynamic excavation flow is overcome by either the force of gravity, the post-

shock strength of the target material, target material viscosity (usually negligible in impacts involving solid, rocky materials), or a combination of these three factors.

In the case of the Deep Impact cratering event, the excavation stage was expected to last for between 1 and 600 s (10 min), depending upon the target material and the comet's gravity field, and was therefore expected to be observed in its entirety during the 800 s (13.3 min) of approach phase imaging. Unfortunately, the copious amount of fine particulate produced by the cratering event obscured the spacecraft's view of the impact area, and the crater formation process was not directly observed (A'Hearn et al., 2005b). However, there is still much information about this process that can be gleaned from the observations that were made, as we will discuss in the following sections.

The halt of crater excavation marks the beginning of the final stage in the process, called the modification stage. This stage comprises two processes which occur simultaneously. First, the plume of solid ejecta particles expelled during the excavation stage will gradually fall out under the influence of the target body's gravity onto its surface, and will thus form a blanket of material extending outward from the rim of the transient crater. Second, the transient crater itself, which is gravitationally unstable due to its steep sides, will collapse, with crater wall materials sliding downward and inward toward the center of the bowl and causing the crater to become wider and shallower as it attains its final shape: for small, simple craters, the final crater diameter is larger than the transient crater diameter by a factor of about 1.1–1.3, with a final depth  $H_f$  to diameter  $D_f$  ratio of about 1/5 (Melosh, 1989). The modification stage is complete when the crater has attained its final, stable form, and all of the impact ejecta have either been redeposited on the surface of the target body or have escaped from the target body's gravity-well.

With regard to the Deep Impact event, it was expected that very little, if any, of the transient crater collapse would be observed, for two reasons: first, this stage would only be captured in the last portion of the 800 s of approach phase imaging, after the excavation stage was complete; and second, the very low gravity field of Comet Tempel 1 (expected to be of order  $0.1\text{--}1.0\text{ mm s}^{-2}$ ) would cause such crater gravitational collapse to proceed quite slowly, and therefore would not be visible in the limited time available. However, it was expected that much of the expansion and fallout of the ejecta plume would be visible, during both the approach and look-back imaging phases, provided that the viewing geometry was favorable and the ejecta particle distribution was fine enough to produce an easily visible ejecta plume (Richardson et al., 2005), as proved to be the case (Fig. 1). Observations of the ejecta plume produced by the Deep Impact mission lasted from the moment of first emergence ( $\sim 340$  ms after impact) all the way to the final look-back images taken 75 min following the impact.

## 1.2. Basic cratering physics

In one respect, our understanding of the Deep Impact cratering event is much better constrained than that of the multi-

kilometer scale impact craters observed on the Earth and other moons and planets. Unlike the large craters that form a major part of the landscapes of most airless bodies, the relatively small Deep Impact event is a reasonably good match to our ability to compute or experimentally model such impacts. In this section, we lay out the basic concepts upon which the model used for this ballistics analysis is based.

Although complex and multi-staged, the physics involved in the formation of an impact crater is well understood, at least on the fundamental level. The impact and subsequent growth of the crater are governed by a set of classical differential equations known as the Navier–Stokes equations, which are supplemented by (1) an equation of state that describes the material thermodynamic properties, and (2) a set of constitutive equations that describe the rheologic properties of the materials—see Melosh (1989) for a detailed description and references. The Navier–Stokes equations express the conservation of mass, energy and momentum. The equation of state relates the pressure in all materials, and mixtures of materials, to their densities and internal energies. The constitutive equations define a material model that links stresses and strains. The principal uncertainties in using these equations directly are in the accuracy of both the equation of state and the material constitutive model. These relations are not well known for most natural materials, and thus makes finite-element, computational hydrodynamic (CHD) modeling of the Deep Impact event somewhat problematic, although such work should still be attempted for reasons outlined below.

Nonetheless, the basic Navier–Stokes equations themselves do offer some insight into the process. As in many such equations, they possess several “invariances”: changes of some variable that leaves the overall equation unchanged. If gravity or rate-dependent strength is not involved (which is too drastic a simplification in practice), one of the principal invariances is a coordinated relationship between length scales and time. For example, a 1 mm projectile striking a target at  $10\text{ km s}^{-1}$  will yield the same result as a 1 m projectile striking a similar target at the same speed, provided all distances are scaled by the same ratio of 1000 and all times are multiplied by the same factor. Thus, if the 1 mm laboratory projectile makes a crater 10 cm in diameter in 100 ms, the 1 m Deep Impact projectile should create a 100 m diameter crater in 100 s. In this scaling relationship, velocities, densities, and strengths are unchanged, and the target from which the problem is scaled must be very similar to the actual, larger-scaled target. This simple scaling invariance thus opens the door to detailed experimental study of the Deep Impact cratering event, providing that we can find close matches to the actual material of the comet and achieve velocities similar to that of the Deep Impact collision. Laboratory studies using two-stage light gas guns are limited to about  $6\text{ to }8\text{ km s}^{-1}$ , but this is not very far from the actual conditions. Schultz et al. (2007) describe a detailed laboratory simulation approach using just this correspondence.

The main factors that inhibit this experimental approach are (1) target materials that possess a rate-dependent material strength, and (2) the target body's gravity. Although many target materials do not have this first problem, rate-dependence



is observed for carbonates (Larson, 1977) and other materials (Melosh et al., 1992), so caution in selecting a comet-simulant material is necessary. If gravity is important in limiting the crater's growth, then the previous, simple invariance does not hold. Gravity is a function of (distance)/(time)<sup>2</sup>; so, for a strictly correct comparison between the laboratory and the actual Deep Impact event, the acceleration of gravity must be scaled as the inverse of the distance or time ratio. Thus, the 1 mm projectile in a terrestrial gravity field corresponds to a 1 m projectile in a gravity field of 1/1000 of Earth's surface gravity. This is certainly a step in the right direction for experimentally modeling Deep Impact, but to simulate the comet impact exactly under Earth's gravity, we really need a projectile about 10–100  $\mu\text{m}$  in diameter, made of the same materials as the impactor–spacecraft and striking a target of the same composition as the comet's surface at 10.2  $\text{km s}^{-1}$ . Even the grain size of the comet-simulant material must be reduced by the same factor of  $10^{-5}$ – $10^{-6}$  from the grain size in the actual comet. This is a much more difficult set of conditions to match for experimental studies, and may require the CHD numerical methods mentioned above to help bridge the gaps. Conversely, any numerical computations should be checked by experimental findings wherever possible. For the work described in this paper, however, we opted for a third route of model development.

### 1.3. Cratering event scaling relationships

Although it is often difficult to satisfy the requirements of the exact space/time/material invariance in the Navier–Stokes equations, an approximate form of invariance has been long recognized in impacts and explosions. This invariance ultimately stems from the fact that the final crater is usually much larger than the projectile, such that projectile-specific properties (such as diameter, shape, and composition) do not affect the final outcome: a concept referred to as “late-stage equivalence” (Dienes and Walsh, 1970). In this case, only a single, dimensional “coupling parameter,” which depends upon the projectile's total energy and momentum, will affect the size and shape of the end cratering result (Holsapple and Schmidt, 1987). When this is the case, a number of power-law scaling relationships have been observed in experimental impacts, and derived mathematically as point-source solutions, that link impacts of different sizes, velocities and gravitational accelerations. The derivation of these crater scaling relationships is based upon the Buckingham  $\pi$  theorem of dimensional analysis (Buckingham, 1914) and have undergone extensive development over the years, as described in Holsapple and Schmidt (1980, 1982), Housen et al. (1983), Holsapple and Schmidt (1987), Schmidt and Housen (1987), and the review work, Holsapple (1993). Below is a brief summary of this work.

This approach begins with the assumption that the desired parameter for which we wish to find a functional relationship can be accurately described by a few key impact variables. For example, we assume that the transient crater volume  $V$  can be described by

$$V = f(a, \rho_i, v_i, g, \rho_t, Y), \quad (1)$$

where  $a$ ,  $\rho_i$ , and  $v_i$  are the impactor's radius, density, and velocity, respectively;  $g$  is the gravity field magnitude at the impact site; and  $\rho_t$  and  $Y$  are the target material's density and strength, respectively. This gives us seven total parameters (including the desired volume), which are described using three units of measure (mass, length, and time). According to the  $\pi$  theorem of dimensional analysis, we can reduce the number of parameters in this function down to  $7 - 3 = 4$  dimensionless parameters.

In impact cratering, the most commonly used set of four dimensionless parameters are

$$\pi_V = \frac{\rho_t V}{m_i}, \quad (2)$$

where  $\pi_V$  is called the cratering efficiency and  $m_i$  is the mass of the impactor, given by  $m_i = (4/3)\pi\rho_i a^3$ ;

$$\pi_2 = \frac{g}{v_i^2} \left( \frac{m_i}{\rho_i} \right)^{\frac{1}{3}} = 3.22 \left( \frac{ga}{v_i^2} \right), \quad (3)$$

where  $\pi_2$  is called the gravity-scaled size, and is a measure of the importance of gravity in the cratering event. The factor of  $(4\pi/3)^{1/3} = 3.22$  is often neglected, or written as 1.61 if the impactor is placed in terms of its diameter  $d$  rather than its radius  $a$ ;

$$\pi_3 = \frac{Y}{\rho_t v_i^2}, \quad (4)$$

where  $\pi_3$  is called the non-dimensional strength, and is a measure of the importance of target strength in the cratering event. Many early works use the projectile density  $\rho_i$  in place of target density  $\rho_t$  in the denominator, so one must carefully note which form is being used in each study. And lastly

$$\pi_4 = \frac{\rho_t}{\rho_i}, \quad (5)$$

where  $\pi_4$  is the density ratio between target and impactor, and is often assumed to be  $\approx 1$  in many applications (and is therefore negligible).

Using these four dimensionless variables and invoking late-stage equivalence (the existence of a physically meaningful coupling parameter), we could describe our desired crater volume function as a power-law relationship, having the form:

$$\pi_V = K_V \pi_2^{-\alpha} \pi_3^{-\beta} \pi_4^{-\gamma}, \quad (6)$$

where  $K_V$ ,  $\alpha$ ,  $\beta$ , and  $\gamma$  are undetermined constants. However, a more useful form of this equation is obtained by placing all of the impactor related variables into a single, explicit coupling parameter, defined in Holsapple and Schmidt (1987) as  $C = av_i^\mu \rho_i^\nu$ . This gives the following (Holsapple, 1993):

$$V = f(av_i^\mu \rho_i^\nu, g, \rho_t, Y), \quad (7)$$

for our desired volume function. Performing dimensional analysis using this form eventually leads to a new formulation of Eq. (6), given in Holsapple (1993) as

$$\pi_V = K_1 \left[ \pi_2 \pi_4^{\frac{6\nu-2-\mu}{3\mu}} + \left[ K_2 \pi_3 \pi_4^{\frac{6\nu-2}{3\mu}} \right]^{\frac{2+\mu}{2}} \right]^{-\frac{3\mu}{2+\mu}}. \quad (8)$$

In practice,  $\nu$  can generally be taken as equal to  $1/3$  at all times, while  $\mu$  is variable between  $1/3 \leq \mu \leq 2/3$ , depending upon whether the cratering event is primarily governed by the impactor's kinetic energy ( $\mu = 2/3$ ) or momentum ( $\mu = 1/3$ ) (Holsapple and Schmidt, 1987). If we further assume that  $K_2$  is close enough to unity to permit the quantity  $K_2 Y$  to equal an “effective” material strength  $\bar{Y}$ , then we can simplify Eq. (8) to give (Holsapple, 1993):

$$\pi_V = K_1 \left[ \pi_2 \pi_4^{-\frac{1}{3}} + \bar{\pi}_3^{\frac{2+\mu}{2}} \right]^{-\frac{3\mu}{2+\mu}}, \quad (9)$$

where  $\pi_2 = (ga/v_i^2)$  and  $\bar{\pi}_3 = (\bar{Y}/\rho_t v_i^2)$ .

Bringing everything together, we solve for our originally desired function for the transient crater volume:

$$V = K_1 \left( \frac{m_i}{\rho_t} \right) \left[ \left( \frac{ga}{v_i^2} \right) \left( \frac{\rho_t}{\rho_i} \right)^{-\frac{1}{3}} + \left( \frac{\bar{Y}}{\rho_t v_i^2} \right)^{\frac{2+\mu}{2}} \right]^{-\frac{3\mu}{2+\mu}}, \quad (10)$$

where  $K_1$ ,  $\mu$ , and  $\bar{Y}$  are experimentally derived properties of the target material. The transient crater volume  $V$  can be related to the more easily measured transient crater diameter  $D$  or radius  $R$  by

$$V = \frac{1}{24} \pi D^3 = \frac{1}{3} \pi R^3, \quad (11)$$

where we assume that the transient crater depth  $H$  is roughly  $1/3$  its diameter  $D$ : in experiments this is somewhat variable, between  $1/4$  and  $1/3$  (Schmidt and Housen, 1987; Melosh, 1989).

If the force of gravity  $g$  is much greater than the effective yield strength of the target material  $\bar{Y}$ ; that is, if it takes much more energy to loft the material out of the crater bowl than it takes to effectively break the material apart, then Eq. (10) can be simplified to

$$V_g = K_1 \left( \frac{m_i}{\rho_t} \right) \left( \frac{ga}{v_i^2} \right)^{-\frac{3\mu}{2+\mu}} \left( \frac{\rho_t}{\rho_i} \right)^{\frac{\mu}{2+\mu}}, \quad (12)$$

a condition called gravity-dominated cratering. If the force of gravity  $g$  is much smaller than the effective yield strength of the target material  $\bar{Y}$ ; that is, if it takes much less energy to loft the material out of the crater bowl than it takes to effectively break the material apart, then Eq. (10) can be simplified to

$$V_s = K_1 \left( \frac{m_i}{\rho_t} \right) \left( \frac{\bar{Y}}{\rho_t v_i^2} \right)^{-\frac{3\mu}{2}}, \quad (13)$$

a condition called strength-dominated cratering. These two cratering “regimes” are frequently treated as separate end-members in the development of crater scaling relationships, again neglecting the effects of viscosity (Holsapple and Schmidt, 1982).

Utilizing Eqs. (10) and (11), Fig. 3 presents estimates of the transient crater diameter  $D$  produced by a Deep Impact-like event in a variety of Earth-based target materials resting in a variable Tempel 1 gravity field, plotted as a function of comet bulk density  $\rho_t = 100$ – $1500 \text{ kg m}^{-3}$  for a spherical comet of radius  $3.0 \text{ km}$ . The basic properties of these generic target mate-

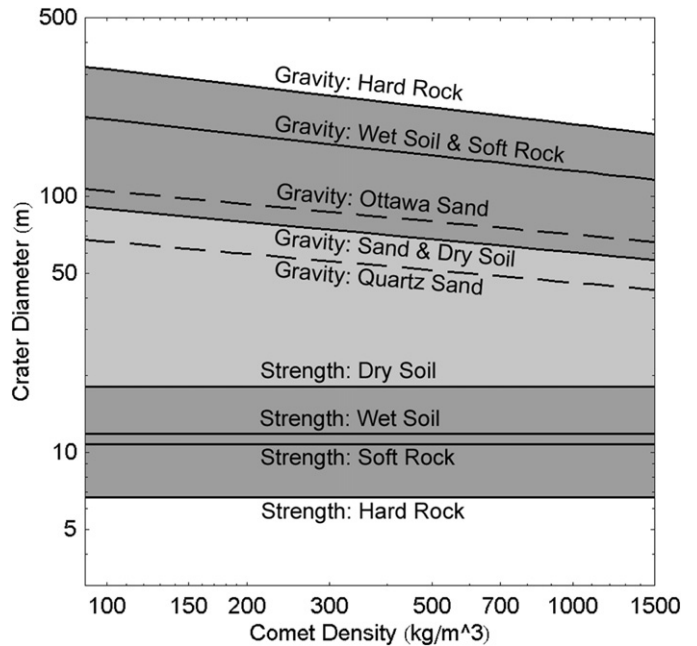


Fig. 3. Several estimates of the transient crater diameter  $D$  produced by a Deep Impact-like event in a variety of Earth-based target materials resting in a Tempel 1 gravity field (varied as a function of comet bulk density  $\rho_t$ ). The solid curves were produced using Eq. (10) and the material constants listed in Table 1, while the dashed curves were produced using Eq. (12) and material constants for quartz and Ottawa sand contained in Melosh (1989). The upper set of curves, labeled “Gravity,” include zero material strength, and thus represent upper limits to the size of craters possible in these materials. The lower set of curves, labeled “Strength,” include nominal values for the strength of these materials (Table 1), and thus represent lower limits to the size of craters possible in these materials.

Table 1  
Common target properties: Holsapple (1993)

| Material  | $K_1$ | $\mu$ | $\bar{Y}$ (MPa) | $\rho_t$ ( $\text{kg m}^{-3}$ ) |
|-----------|-------|-------|-----------------|---------------------------------|
| Water     | 2.30  | 0.55  | 0.0             | 1000                            |
| Sand      | 0.24  | 0.41  | 0.0             | 1750                            |
| Dry soil  | 0.24  | 0.41  | 0.18            | 1500                            |
| Wet soil  | 0.20  | 0.55  | 1.14            | 2000                            |
| Soft rock | 0.20  | 0.55  | 7.6             | 2250                            |
| Hard rock | 0.20  | 0.55  | 18.0            | 2500                            |

rials are listed in Table 1, and are taken directly from Holsapple (1993). In general, when all material strengths are set to zero, the comet's low gravity dominates the halt of the excavation flow and craters of order 100–200 m diameter result. When material strengths are set to their Table 1 values, strength dominates the halt of excavation flow and craters of order 10–20 m diameter result. Smaller values of material strength (less than those listed in Table 1) will fill in the area bounded by these two sets of curves, to give us a spectrum of possible crater diameter outcomes.

Another useful scaling relationship is the crater formation time  $T$ ; that is, how much time passes between the beginning of the coupling phase to the end of the excavation stage. Schmidt and Housen (1987) give the following expression for gravity-dominated cratering:

$$T_g = K_{Tgl} \left( \frac{a}{v_i} \right) \left( \frac{\rho_t}{\rho_i} \right)^{-\frac{1}{3(2+\mu)}} \left( \frac{ga}{v_i^2} \right)^{-\frac{1+\mu}{2+\mu}}, \quad (14)$$

along with a more convenient “short-form” solution:

$$T_g = K_{Tg} \sqrt{\frac{V^{1/3}}{g}}. \quad (15)$$

A proportionality constant value of  $K_{Tgl} = 1.6$  is given by Melosh (1989), derived from the data presented in Schmidt and Housen (1987), while in Fig. 9 of Schmidt and Housen (1987), an experimentally determined value of  $K_{Tg} = 0.8$  is provided. Due to the “self-similarity” of all gravity-scaled craters, these constants are applicable to the full spectrum of impact environments and target materials (from sand to hard rock), and we shall make use of constant  $K_{Tg}$  in Section 2.

With regard to strength-dominated cratering, Schmidt and Housen (1987) give the following long-form equation for the crater formation time:

$$T_s = K_{Tsl} \left( \frac{a}{v_i} \right) \left( \frac{\rho_t}{\rho_i} \right)^{-\frac{1}{3}} \left( \frac{\bar{Y}}{\rho_t v_i^2} \right)^{-\frac{1+\mu}{2}}. \quad (16)$$

while in Housen et al. (1983) we find the equivalent “short-form” version:

$$T_s = K_{Ts} V^{\frac{1}{3}} \sqrt{\frac{\rho_t}{\bar{Y}}}. \quad (17)$$

However, no values for the strength-dominated proportionality constants  $K_{Tsl}$  or  $K_{Ts}$  have been published in the literature, and even if they were, due to the non-similarity of strength-dominated craters, such constants would be limited to very similar experiments only.

Utilizing Eqs. (14) and (15), Fig. 4 presents estimates of the gravity-dominated formation times  $T_g$  for the crater produced by a Deep Impact-like event in a variety of Earth-based target materials resting in a variable Tempel 1 gravity field, plotted as a function of comet bulk density. The dotted line across the top of the graph represents the time limit on the approach phase of flyby-spacecraft images, and demonstrates that for all but the very largest craters, produced in the weakest comet gravity fields, the full crater formation time should have been observed by the flyby-spacecraft through the obscuring dust. As with the upper curves shown in Fig. 3, these curves represent an upper limit to the crater formation time, when the material strength  $\bar{Y}$  is essentially zero, such that a formation time on the order of a few hundred seconds results. Adding strength to the material can reduce this crater formation time significantly. For example, if we assume constant values of unity (1.0) for  $K_{Tsl}$  and  $K_{Ts}$  in Eqs. (16) and (17), respectively, we get strength-dominated crater formation times of  $< 1$  s for all of the materials shown in the lower curves of Fig. 3.

The key question presented by both Fig. 3 and Fig. 4 is: to what degree did gravity or strength dominate the growth of the crater produced by Deep Impact? One method for gauging the relative contribution of each of these factors is to plot the cratering efficiency  $\pi_V$  (Eq. (9)) vs the gravity-scaled size  $\pi_2$  (Eq. (3)) over a range of expected gravity field magnitudes  $g$  and potential material strengths  $\bar{Y}$ . This type of plot

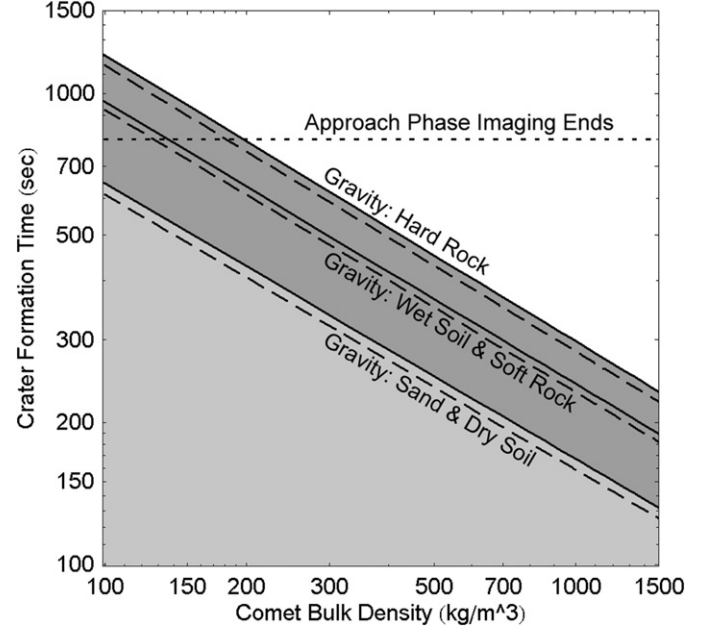


Fig. 4. Several estimates of the transient crater formation time  $T$  produced by a Deep Impact-like event in a variety of Earth-based target materials resting in a Tempel 1 gravity field (varied as a function of comet bulk density  $\rho_t$ ). The dashed curves use the long-form, gravity-dominated solution, Eq. (14), while the solid curves use the short-form, gravity-dominated solution, Eq. (15), one pair of curves for each material. These curves do not include any of the strengths given in Table 1, and thus represent upper limits to the crater formation time in these target materials. Strength-dominated crater formation times for these materials, produced using the strengths listed in Table 1 and assumed proportionality constants of 1.0 for Eqs. (16) and (17), are  $< 1$  s in duration, and would therefore be low off the scale of this plot.

is shown in Fig. 5, where each curve represents a different material strength  $\bar{Y}$ , and both  $\pi_V$  and  $\pi_2$  are plotted as functions of the comet bulk density  $\rho_t = 10\text{--}10,000 \text{ kg m}^{-3}$  for a spherical comet of radius 3.0 km. Wherever  $\pi_V$  varies as a direct power-law function of  $\pi_2$  (a diagonal line in log-log space), then gravity-dominated cratering is indicated. Wherever the cratering efficiency  $\pi_V$  is constant as a function of  $\pi_2$  (a horizontal line in log-log space), then strength-dominated cratering is indicated. Curving lines indicate the transition from one form of dominance to the other. As Fig. 5 demonstrates, it should take very little strength, on the order of  $\bar{Y} = 10\text{--}100 \text{ Pa}$ , to cause the crater created by the Deep Impact mission to transition from one dominated by gravity to one dominated by target strength.

This transition strength  $Y_t$  can also be estimated by setting the gravity and strength terms in Eq. (10) equal to each other, as suggested in Holsapple (1993). This gives

$$Y_t = \rho_t v_i^2 \left[ \left( \frac{ga}{v_i^2} \right) \left( \frac{\rho_i}{\rho_t} \right)^{\frac{1}{3}} \right]^{\frac{2}{2+\mu}}. \quad (18)$$

In similar fashion to Fig. 5, Eq. (18) indicates a transition strength of  $Y_t = 5\text{--}50 \text{ Pa}$  for the range of cometary gravities and material constants we are considering. Obviously, a strength-dominated event is likely, and must be carefully dealt with in any model and analysis of this cratering event.

To add another complication, the entire concept of what is meant by “strength” in impact cratering is presently somewhat

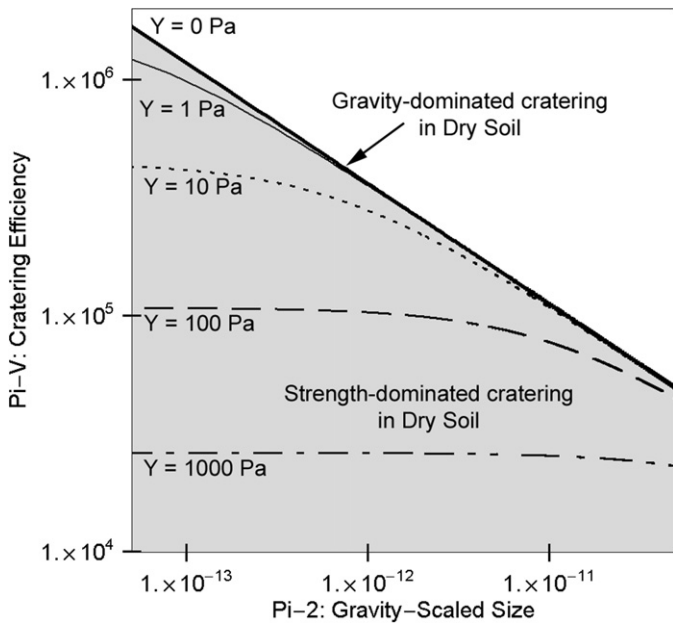


Fig. 5. A plot of cratering efficiency  $\pi_V$  (Eq. (2)) versus gravity-scaled size  $\pi_2$  (Eq. (3)) for a Deep Impact-like event, where both  $\pi_V$  and  $\pi_2$  are plotted as functions of comet Tempel 1's bulk density  $\rho_t$ , ranging from 10 to 10,000  $\text{kg m}^{-3}$ . Dry soil is used for the basic material parameters, and each curve represents a different value of the effective material strength  $\bar{Y}$ . The upper, bold curve shows the result of  $\bar{Y} = 0$  Pa and gravity-dominated cratering. Increasing this strength incrementally (the remaining curves) reveals a transition zone from gravity to strength domination between about 10 and 100 Pa (curved lines), with strength dominating the cratering event completely at strengths above these values (such as the  $\bar{Y} = 1000$  Pa line).

fuzzy. Modern theories of dynamic fracture indicate that the actual failure strength of a material should be strongly rate dependent (Grady and Kipp, 1987), a factor not included in the derivation of the crater scaling relationships. Additionally, CHD modeling indicates that the strength of the material surrounding an impact is often strongly degraded by shock-wave passage long before the excavation flow clears this material out of the crater interior, such that the excavation stage is governed more by a target's "post-shock" strength than its initial strength (Croft, 1981; Asphaug and Melosh, 1993; Nolan et al., 1996). Furthermore, impact energy expended in the compaction of porous target material will also manifest itself as a form of "strength," since our current scaling relationships include only a generic stress variable  $Y$ , equivalent to an energy expended per unit volume during crater formation, which does not specify how that energy was actually used (Housen and Holsapple, 2003; Holsapple and Housen, 2007). We must therefore be careful to refer to any determined strength for the surface of Tempel 1 as an "effective" strength  $\bar{Y}$ , and note that the value obtained will be more of a nebulous yield strength (or energy density) than a specific laboratory-referenced material strength—tensile, compressive, shear, or otherwise. With this qualification in mind, in the next section we continue to make use of derived cratering event scaling relationships to develop a model of cratering excavation flow, which will include the effects of target material strength.

## 2. Model theoretical development

The primary focus of this study is, in effect, to solve a ballistics problem: where in this case we are not able to actually see the individual projectiles (ejecta particles) in flight, but can instead only monitor the collective behavior of the ejecta particles as they form a hollow, expanding, cone-shaped cloud. Nonetheless, as with all ballistics problems, the primary variables fall into two major categories: (1) the particle launch conditions, given by starting position, time, velocity, and launch angle; and (2) the forces on the particle in flight, dominated by the gravity field of the comet, but also including smaller forces, such as solar radiation pressure. It is therefore convenient to break the description of the model into two sections, one describing the theoretical development of the model (this section), which goes into establishing the launch conditions of the impact ejecta particles; and one describing the computational development of the model (Section 3), which determines the forces on individual particles once launched, and traces their flight over time to either landing or escape.

### 2.1. The Maxwell Z-model of excavation flow

As mentioned in Section 1.1, the excavation flow-field established by the passage of the initial shock-wave and its surface reflection (rarefaction-wave), has very fluid-like (hydrodynamic) properties. These properties were first modeled and explored in detail for explosion craters by Maxwell and Seifert (1974) and then extended to impact craters by Maxwell (1977), in what became known as the Maxwell Z-model of crater excavation. While our work is not a direct application of the Maxwell Z-model, there are many features of excavation flow first recognized in that model which we will take advantage of in this work.

As stated in Maxwell (1977), there are two key, experimentally observed features of the cratering excavation flow:

- The transit of the ground shock through the incipient cratering region initiates a cratering flow-field that persists long after the impulsive stresses have decayed.
- The associated cratering process can be approximated as incompressible flow along stationary streamlines.

Fig. 6 shows a graphical representation of the early stages of crater excavation flow using the Maxwell Z-model, and depicts 18 tracer particles strung like beads along seven different flow streamlines (the arrowed lines) to illustrate the key features. These are:

- All particles at a given radial distance  $r$  from the impact site will *begin* motion at the same speed. This is represented by the three contour lines (isotachs) connecting particles 1 and 4, then 2 and 5, and finally 3 and 6, respectively, in time-step (a).
- For a normal-incidence (vertical) impact into a horizontally flat target, all streamlines will be axially symmetric about the impact-point's surface normal vector, producing



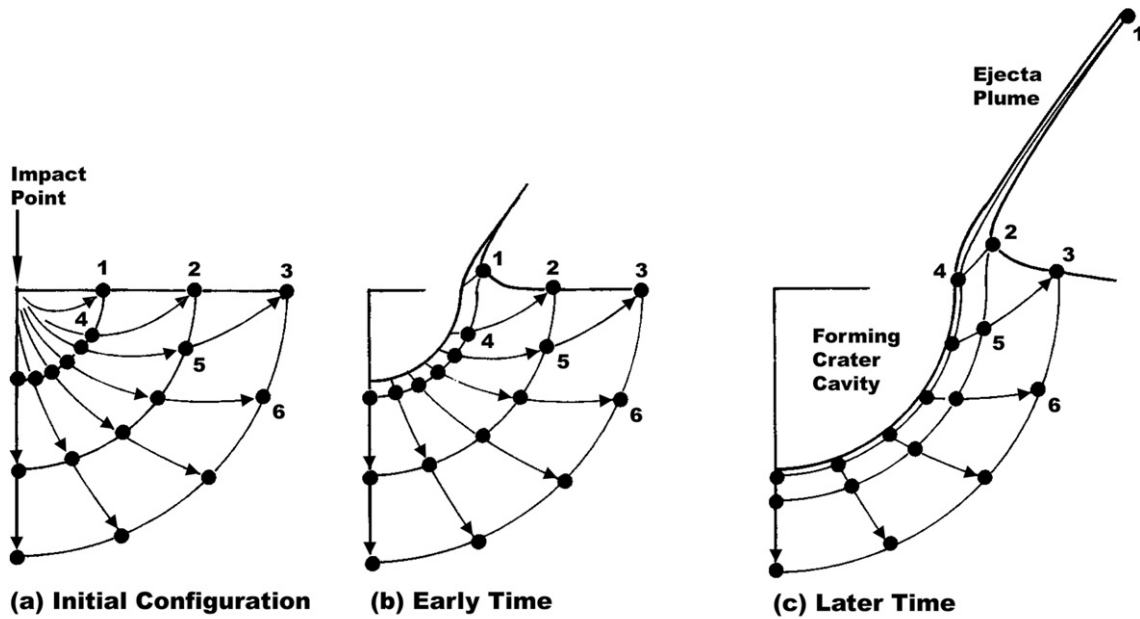


Fig. 6. Graphical representation of the Maxwell Z-model of excavation flow, adapted from a similar figure in Maxwell (1977). Depicted is the motion of 18 tracer particles (six are numbered) over a short time period from the time of impact, as they move along seven hydrodynamic streamlines (the arrowed lines). All tracer particles begin motion immediately after impact and flow-field establishment, and fall on three velocity contours: the three lines of constant radius shown in part (a). These streamlines are axially symmetric, producing “streamtubes” in three dimensions, such that the tracer particles will decelerate as they progress along their respective streamlines, which maintains the continuity of mass in a 3-D streamtube of increasing area. All particles in a given streamline, emerging from the ground surface at some distance  $r$  from the impact site, will have the same ejection velocity (that of particles 1, 2, and 3).

“streamtubes” in three dimensions. As such, to maintain incompressible flow and satisfy the continuity equation (conservation of mass), flow velocity along each streamtube must necessarily decrease with increasing distance from the impact site, as the streamtube surface area increases.

- All particles in a given streamline will emerge from the surface at the same, final, ejection velocity. That is, all particles passing through the original ground surface at some radial distance  $r$  from the impact site will have the same emergence velocity  $v_e$  (speed and ejection angle). Thus, although particles 2 and 4 begin motion at different speeds, they will both be ejected at the same speed (that of particle 2). The same thing holds true for particles 3 and 5, which also emerge at the same speed (that of particle 3).
- Although the flow in each streamline is steady-state and incompressible, it is not inviscid: frictional forces between the particles, and in particular, between particles in adjacent streamlines, contribute to slowing the particles as they move radially outward and curve upward.
- Once the particles in each streamline have moved above the original, ground surface level, they are considered to be ballistically launched and all frictional forces between particles are assumed to become negligible.

Each streamline in Fig. 6 has both a “leading edge,” indicated by particles 1, 2, and 3, and a “trailing edge” indicated by the wall of the expanding crater cavity. As each streamline approaches and then breaks the surface completely, shown by the streamline containing particle 1 in time-step (b) and then by the streamline containing particles 2 and 4 in time-step (c), the trail-

ing edge of that streamline will evolve from forming part of the cavity wall, to marking the cavity rim (upon emergence), and finally to forming part of the ballistically launched ejecta plume. Also note that particles on the leading edge of each streamline become ballistically ejected immediately upon flow-field establishment.

With time and the development of computational hydrodynamic (CHD) codes, the Maxwell Z-model lost much of its utility because at its best, it represents only a good first-order description of cratering excavation flow and lacks many of the finer variations present in even a simple cratering event (Croft, 1980; Austin et al., 1980). Nonetheless, many of the experimentally observed features contained in the Maxwell Z-model continue to be valid, and we shall refer to this section frequently in the development of our own, scaling-relation based model. In contrast to the Z-model, our model will deal only with particle behavior at the point of launch (that is, as the particles leave the level of the original ground surface), and thereafter. Excavation flow-field behavior prior to this point (below the ground surface) is left to the CHD modelers, who have a much more capable tool for handling those details.

## 2.2. Impact ejecta scaling relationships

Our first task is to determine the correct particle ejection (launch) velocities for a given impact event. To accomplish this we utilize eight of the equations given in Table 1 of Housen et al. (1983), which were developed using the dimensional analysis techniques described in Section 1.3 to scale and model the behavior of impact ejecta. These scaling relationships, how-

ever, lack numerical values for their proportionality constants, and we must therefore find a way to fix each constant's value in terms of some experimentally determined constants. For this exercise, we will continue to use the material constant  $\mu$  from Section 1.3, and include the constant  $K_{Tg}$  from Eq. (15) (Schmidt and Housen, 1987).

To describe the launch position, time, and velocity of both leading and trailing edge ejecta in the gravity-dominated cratering regime, we will use four of the relationships from Table 1 of Housen et al. (1983), beginning with the equation for the crater formation time  $T_g$ :

$$T_g = C_{Tg} \sqrt{\frac{R_g}{g}}, \quad (19)$$

where  $R_g$  is the gravity-dominated transient crater radius determined from Eqs. (10) and (11). We can immediately recognize the similarity of Eq. (19) to Eq. (15) and determine that

$$C_{Tg} = K_{Tg} \left( \frac{\pi}{3} \right)^{\frac{1}{6}}, \quad (20)$$

for a crater in which the transient crater has a depth to diameter ratio of 1/3. In effect,  $C_{Tg} \approx K_{Tg}$  within experimental accuracy.

Now we take advantage of the relationship of Eq. (19) to the given equation for plume position  $r$  as a function of time  $t$  in Housen et al. (1983):

$$r(t) = C_{pg} R_g \left( t \sqrt{\frac{g}{R_g}} \right)^{\frac{\mu}{\mu+1}}, \quad (21)$$

where  $t$  is the time after impact, and we have replaced the given exponent  $\alpha$  with its equivalent form of  $\alpha = 3\mu/(2 + \mu)$  from Holsapple and Schmidt (1987). There are two important things to note about Eq. (21). First, we define the “plume position” referred to in Table 1 of Housen et al. (1983) as the base of the *trailing edge* of the ejecta plume, which progresses in near power-law fashion from the impact site toward the transient crater rim. Second, as discussed in Section 2.1, the base of the trailing edge of the ejecta plume also marks the cavity rim position, such that the bowl of the growing crater and the trailing edge of the ejecta plume form a continuous, moving surface during crater growth (Fig. 6).

We can solve for the constant  $C_{pg}$  by assuming that the crater exhibits power-law growth *all* the way out to the transient crater rim at  $R_g$ . This is not entirely the case, due to the forces of strength and/or gravity slowing the growth near the transient crater rim (Holsapple and Schmidt, 1987; Schmidt and Housen, 1987), but this approximation works reasonably well, especially since the cavity rim approaches this point asymptotically. Accepting this assumption, we set  $t = T_g$  and  $r = R_g$  in Eq. (21) to obtain the following expression for the constant  $C_{pg}$ :

$$C_{pg} = C_{Tg}^{-\frac{\mu}{\mu+1}}. \quad (22)$$

The cavity rim position expression, Eq. (21), is also useful in that the speed at which the crater rim advances must necessarily be equal to the horizontal velocity component  $v_{eh}$  of the

ejecta which is, at that moment, just leaving the rim to join the ejecta plume (Section 2.1). Thus, by taking the first derivative of Eq. (21) we obtain:

$$v_{eh}(t) = C_{pg} \left( \frac{\mu}{\mu+1} \right) \sqrt{g R_g} \left( t \sqrt{\frac{g}{R_g}} \right)^{-\frac{1}{\mu+1}}. \quad (23)$$

The total ejection velocity can be obtained if we know the particle ejection angle  $\psi$  (measured from the horizontal) by using  $v_e = v_{eh} \sec \psi$ . For this constant derivation exercise, we adopt a mean ejection angle of  $\bar{\psi} \approx 45^\circ$ , an assumption which dates back to the original Z-model (Maxwell and Seifert, 1974). Actual ejection angles vary with distance  $r$  (Section 2.4), but this assumption holds reasonably well for the materials that we are considering here. This gives

$$v_e(t) = C_{Tg}^{-\frac{\mu}{\mu+1}} \sqrt{2} \left( \frac{\mu}{\mu+1} \right) \sqrt{g R_g} \left( t \sqrt{\frac{g}{R_g}} \right)^{-\frac{1}{\mu+1}}, \quad (24)$$

which has the same form as that given in Housen et al. (1983) for the ejection velocity as a function of time:

$$v_e(t) = C_{vtg} \sqrt{g R_g} \left( t \sqrt{\frac{g}{R_g}} \right)^{-\frac{1}{\mu+1}}, \quad (25)$$

and by comparison we find that

$$C_{vtg} = C_{Tg}^{-\frac{\mu}{\mu+1}} \sqrt{2} \left( \frac{\mu}{\mu+1} \right). \quad (26)$$

At this point we have obtained an expression for the particle ejection velocity as a function of time  $t$  for the trailing edge of the ejecta plume (at the advancing cavity rim). However, the ejecta on the leading edge of the ejecta plume are launched immediately (effectively at time  $t = 0$ ), so we must next obtain an expression for the particle ejection velocity  $v_e$  as a function of position  $r$ . To do this, we first rearrange the cavity rim position Eq. (21) to solve for the time  $t$ :

$$t(r) = C_{Tg} \sqrt{\frac{R_g}{g}} \left( \frac{r}{R_g} \right)^{\frac{\mu+1}{\mu}}. \quad (27)$$

Note that if we let  $r$  go to  $R_g$  in Eq. (27), we recover our previous expression for the gravity-dominated crater formation time  $T_g$  (Eq. (19)). Equation (27) serves two important purposes in our model: first, it gives us the ejection time  $t$  as a function of rim position  $r$  for particles on the trailing edge of the ejecta plume; second, it serves as a good approximation for the crater formation time  $T_s$  in strength-dominated cratering events, by letting  $r = R_s$  and solving for the time  $t$ .

If we substitute the ejection time expression, Eq. (27), into the ejection velocity expression, Eq. (25), we obtain an expression for the ejection velocity  $v_e$  as a function of position  $r$ :

$$v_e(r) = \frac{\sqrt{2}}{C_{Tg}} \left( \frac{\mu}{\mu+1} \right) \sqrt{g R_g} \left( \frac{r}{R_g} \right)^{-\frac{1}{\mu}}. \quad (28)$$

Equation (28) has the same form as that given in Housen et al. (1983) for the gravity-dominated ejection velocity as a function

of position:

$$v_e(r) = C_{vpg} \sqrt{g R_g} \left( \frac{r}{R_g} \right)^{-\frac{1}{\mu}}, \quad (29)$$

and by comparison, we obtain an expression for the proportionality constant:

$$C_{vpg} = \frac{\sqrt{2}}{C_{Tg}} \left( \frac{\mu}{\mu + 1} \right). \quad (30)$$

Thus, we can now describe the launch position, time, and velocity of both leading and trailing edge ejecta in the gravity-dominated cratering regime. We can perform this same exercise for the four equations describing impact ejecta behavior in the strength-dominated cratering regime, given in Table 1 of Housen et al. (1983), to obtain:

Crater formation time (strength regime):

$$T_s = C_{Ts} R_s \sqrt{\frac{\rho_t}{\bar{Y}}}, \quad (31)$$

where  $R_s$  is the strength-dominated transient crater radius, determined using Eqs. (10) and (11), and

$$C_{Ts} = K_{Ts} \left( \frac{\pi}{3} \right)^{\frac{1}{3}}. \quad (32)$$

Ejecta plume trailing edge, or cavity rim position (strength regime):

$$r(t) = C_{ps} R_s \left( \frac{t}{R_s} \sqrt{\frac{\bar{Y}}{\rho_t}} \right)^{\frac{\mu}{\mu+1}}, \quad (33)$$

where

$$C_{ps} = C_{Ts}^{-\frac{\mu}{\mu+1}}. \quad (34)$$

Ejecta velocity as a function of time for the plume trailing edge (strength regime):

$$v_e(t) = C_{vts} \sqrt{\frac{\bar{Y}}{\rho_t}} \left( \frac{t}{R_s} \sqrt{\frac{\bar{Y}}{\rho_t}} \right)^{-\frac{1}{\mu+1}}, \quad (35)$$

where

$$C_{vts} = C_{Ts}^{-\frac{\mu}{\mu+1}} \sqrt{2} \left( \frac{\mu}{\mu + 1} \right). \quad (36)$$

Ejection velocity as a function of emergence position (strength regime):

$$v_e(r) = C_{vps} \sqrt{\frac{\bar{Y}}{\rho_t}} \left( \frac{r}{R_s} \right)^{-\frac{1}{\mu}}, \quad (37)$$

where

$$C_{vps} = \frac{\sqrt{2}}{C_{Ts}} \left( \frac{\mu}{\mu + 1} \right). \quad (38)$$

There is, however, an important distinction between these four equations for the strength regime and the previous four

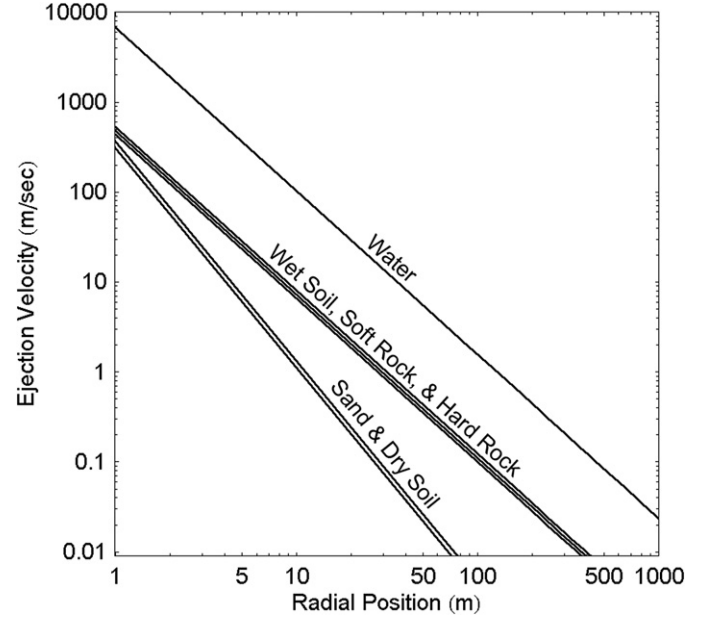


Fig. 7. Ejecta emergence velocity  $v_e$  (Eq. (29)) plotted as a function of radial distance  $r$  from the Deep Impact-like impact of a 1 m diameter,  $700 \text{ kg m}^{-3}$  density sphere striking a variety of Earth-based target materials resting in a low gravity field of  $0.42 \text{ mm s}^{-2}$  (corresponding to a Tempel 1 bulk density of  $\rho_t = 500 \text{ kg m}^{-3}$ ). The steeper sloped lines correspond to the lower value of  $\mu = 0.41$  for sand and dry soil, as compared to the shallower sloped lines corresponding to  $\mu = 0.55$  for the other materials. Small vertical displacements between materials having the same  $\mu$  value are due to material  $K_1$  and target density  $\rho_t$  variations (Table 1). With only frictional losses included, no mechanism for stopping crater growth is present (gravity or strength), such that these curves are not bounded moving to the right and down.

equations for the gravity regime. Due to the self-similarity of all gravity-dominated craters, the proportionality constant  $C_{Tg}$  is invariant across both similar and non-similar impacts, and has an experimentally determined value of 0.8–0.9 (Schmidt and Housen, 1987; Holsapple and Housen, 2007). Unfortunately, strength-dominated craters do not share this property and the value of  $C_{Ts}$  is only invariant across similar impacts. However, because Eqs. (29) and (37) are *equivalent* far from the crater rim, where both gravity and strength effects are small compared to the excavation flow inertia, we can estimate the value of  $C_{vps}$  for each impact environment, given a value of  $C_{vpg}$ :

$$C_{vps} = C_{vpg} \left[ \frac{\rho_t g R_g}{\bar{Y} + Y_t} \right]^{\frac{1}{2}} \left( \frac{R_g}{R_s} \right)^{\frac{1}{\mu}}, \quad (39)$$

where the addition of  $Y_t$  (Eq. (18)) to the denominator maintains equation stability below the transition from strength- to gravity-dominated cratering (low values of  $\bar{Y}$ ). This expression also permits us to estimate the value of  $C_{Ts}$ , using Eq. (38).

At this point, we now have two equivalent ejecta velocity  $v_e$  equations as a function of distance  $r$  from the impact site, as shown for a number of Earth-based target materials in Fig. 7. These functions, however, contain no mechanism for stopping the crater's growth, and will run out to infinitely large crater radii to produce infinitely small ejection velocities. The problem lies in that although these equations do implicitly contain the effect of frictional forces within the streamlines, by solving

for the streamline *emergence* velocity  $v_e$ , they do not contain the effects of gravity and material strength, which are what ultimately halts the growth of the crater. This issue will be addressed in the next section.

### 2.3. The end of crater excavation

To bring in the effects of gravity  $g$  and strength  $\bar{Y}$  and halt the crater's growth, we take advantage of a basic concept described in the Maxwell Z-model (Section 2.1); namely, that the ejecta flow emerging from the surface at some radius  $r$  from the impact site represents a hydrodynamic streamline, which is steady state and incompressible. If we also assume that frictional forces *beyond* those implicit in Eqs. (29) and (37) are small compared to the forces of inertia, gravity, and strength (that is, inviscid flow), we can use Bernoulli's principle at the point of ejecta emergence to form an energy balance equation:

$$\frac{1}{2}\rho_t v_{ef}^2 = \frac{1}{2}\rho_t v_e^2 - K_g \rho_t g r - K_s \bar{Y}, \quad (40)$$

where  $v_e$  is the emergence velocity (after losses due to friction), and  $v_{ef}$  is the effective ejection velocity that we desire (after losses due to gravity and strength). Beginning on the left, the first two terms describe the kinetic energy (or stagnation pressure) of the excavation flow in a single streamline, assuming that upon emergence, the hydrostatic pressure in the flow is zero. The third term describes the mean amount of gravitation potential energy needed to loft each unit volume in the flow (a function of surface radius  $r$ ), and the fourth term describes the amount of energy needed to fracture or “break loose” each unit volume in the flow (a function of effective target strength  $\bar{Y}$ ). We do, however, have two new constants to solve for:  $K_g$  and  $K_s$ .

By substituting Eq. (29) for  $v_e$  in Eq. (40), we can solve for the value of  $K_g$  by setting the target strength  $\bar{Y}$  to zero (assume gravity-dominated cratering) and then let the crater radius  $r$  go to  $R_g$  as the effective velocity  $v_{ef}$  goes to zero (halting crater growth). This gives us  $K_g = C_{vpg}^2/2$ . In similar fashion, we can substitute Eq. (37) for  $v_e$  in Eq. (40), and solve for the value of  $K_s$  by setting the target gravity  $g$  to zero (assume strength-dominated cratering) and then let the crater radius  $r$  go to  $R_s$  as the effective velocity  $v_{ef}$  goes to zero. This gives  $K_s = C_{vps}^2/2$ . Plugging these values into Eq. (40) yields:

$$v_{ef}(r) = \left[ v_e^2 - C_{vpg}^2 g r - C_{vps}^2 \frac{\bar{Y}}{\rho_t} \right]^{\frac{1}{2}}. \quad (41)$$

In examining Eqs. (40) and (41), we can ask: do our values for  $K_g$  and  $K_s$  make physical sense? The value of  $K_g r$  represents a mean streamline excavation depth, and ranges from  $r/9.0$  (at  $\mu = 0.40$ ) to  $r/5.8$  (at  $\mu = 0.55$ ) for a  $C_{Tg}$  value of 0.85. This implies maximum streamline excavation depths of  $r/4.5$  to  $r/2.9$ , which is certainly reasonable: usual values range from  $r/5$  to  $r/4$  (Melosh, 1989). The value of  $K_s \bar{Y}$  represents a post-shock “yield” strength for the target material and, due to the variant nature of  $C_{Ts}$ , can range from  $\bar{Y}/3$  to  $\bar{Y}/15$ , with values from  $\bar{Y}/5$  to  $\bar{Y}/10$  being typical. These values are less than the Tresca maximum shear stress criteria of  $Y/2$  (Turcotte

and Schubert, 2002), assuming that the primary stress during excavation flow is shear stress between adjacent streamlines, but could be reasonable for such “pre-damaged” target material. Both of these constants ( $K_g$  and  $K_s$ ) are deliberately consistent with the previous crater-size scaling relationships (Section 1.3), such that as the computed transient crater rim distance  $R$  is approached, determined by Eqs. (10) and (11), ejecta velocities are properly slowed to zero.

Another way to check our velocity braking function is to look for “overturn-flap” behavior near the rim of gravity-dominated events (Croft, 1980; Melosh, 1989). That is, near the rim of simple, gravity-dominated craters, the last material to be ejected and then redeposited moves in such a way as to maintain its radial and vertical integrity, and thus produces a hinge-like overturn-flap of material visible at the final crater rim. This can be described functionally by a simple ballistics equation:

$$v_o = \left[ \frac{2g(R_g - r)}{\sin(2\psi)} \right]^{\frac{1}{2}}, \quad (42)$$

where  $v_o$  is the velocity necessary to land a particle at the same distance beyond the transient crater rim as it began inside of the transient crater rim, in an environment with a flat surface and uniform gravity field. Our effective ejection velocity  $v_{ef}$  function (Eq. (41)) shows good agreement with this overturn-flap function  $v_o$  (Eq. (42)) over the final 10–20% of crater growth in gravity-dominated events, consistent with the geological observations. Conversely, by insisting upon good agreement with the overturn-flap function (Eq. (42)) over the final stages of transient crater growth, we can constrain the value of constant  $K_{Tg}$  to a range of 0.75–0.95, in good agreement with this constant's experimentally determined values of 0.8–0.9 (Schmidt and Housen, 1987; Holsapple and Housen, 2007).

Fig. 9 shows a set of fits comparing our ejecta velocity model to a series of laboratory experiments described in Cintala et al. (1999), displaying good agreement over the range of data points collected. Moving from the laboratory scale to our desired scale, Fig. 8 shows this ejecta velocity model applied to the Deep Impact event, where here we also introduce our selected simulant material for the surface of Comet Tempel 1: using material constants consistent with those of dry soil and sand,  $\mu = 0.4$  and  $K_1 = 0.2$  (Holsapple, 1993; Holsapple and Housen, 2007), but having a low comet-like density of  $\rho_t = 100\text{--}1500 \text{ kg m}^{-3}$  (Section 4.2) and an expected strength of order  $\bar{Y} = 0\text{--}100 \text{ kPa}$  (Section 4.3). That is, we have selected the material constants consistent with a fine, granular material having a medium porosity and weak strength, where we are limited by those material constants which have been determined experimentally. However, we can also follow the trend evident in Table 1, and observe that as a material's porosity increases, its  $\mu$  value approaches the theoretical limit of  $1/3$  (initially described in Holsapple and Schmidt, 1987), while its cratering efficiency proportionality constant  $K_1$  value decreases (recently shown by the CHD modeling described in Wünnemann et al., 2006). Therefore, we will explore  $\mu$  values of 0.35–0.40 and  $K_1$  values of 0.1–0.2, extending the known values of these constants toward their possible lower limits, but keeping in mind that this is relatively unknown experimental



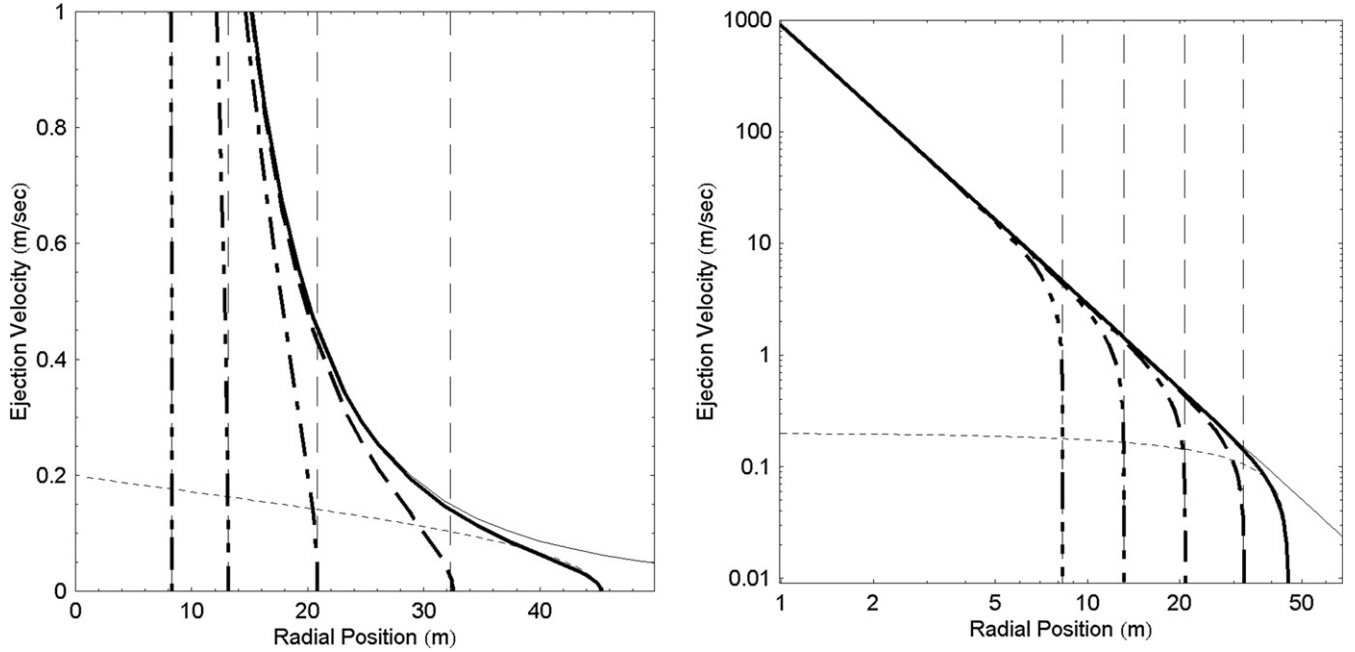


Fig. 8. Modeled ejecta velocities as a function of radial distance  $r$  from the Deep Impact-like impact of a 1 m diameter,  $700 \text{ kg m}^{-3}$  density sphere striking a comet-simulant target ( $\rho_t = 500 \text{ kg m}^{-3}$ ) resting in a low gravity field of  $0.42 \text{ mm s}^{-2}$ : shown in both linear (left) and log (right) format. Legend: *thin solid line* = emergence velocity curve  $v_e$  (Eq. (29)); *thin dotted line* = overturn-flap function  $v_o$  (Eq. (42)), hinged at the computed gravity-dominated crater radius  $R_g$ ; *thick solid line* = zero-strength (gravity-dominated) effective velocity curve  $v_{ef}$  (Eq. (41)); *thick dot-dash lines* = effective velocity curve  $v_{ef}$  (Eq. (41)) at strengths of (0 dot) 0.5 kPa, (1 dot) 5 kPa, (2 dots) 50 kPa, and (3 dots) 500 kPa; *thin dashed lines* = computed strength-dominated crater radii  $R_s$  for these same strength values.

territory. Table 2 lists the input parameters that we have developed for the model so far.

#### 2.4. Impact ejecta launch angles

To determine a useful expression for the particle ejection angle  $\psi$  (measured from the horizontal target surface) as a function of distance  $r$  we will need to rely heavily upon past experimental results and fits to their data. There are currently no scaling relations known for this aspect of impact cratering, and in fact, Housen et al. (1983) simply assume an unspecified, constant ejection angle. Much of the literature on this topic is in regard to excavation flow studies using the Maxwell  $Z$ -model, where the particle ejection angle is related to the parameter  $Z$  by (Maxwell and Seifert, 1974; Maxwell, 1977):

$$\psi = \tan^{-1}(Z - 2), \quad (43)$$

such that for  $Z = 3$ ,  $\psi = 45^\circ$ . Most instances in the literature place  $Z$  at between 2.5 and 4 near the surface, for ejection angles of between  $27^\circ$  and  $63^\circ$ . Here is a summary of the highlights:

- Thomsen et al. (1980b) found that for an impact which penetrates below the surface, ejection angles should decrease as a function of  $r$  in hyperbolic fashion; rapidly at first, and then leveling off. They obtained  $Z$  values of 3–4 ( $\psi = 45^\circ$ – $63^\circ$ ) near the surface for their experiment.
- Thomsen et al. (1980a) determined a best-fit surface  $Z = 2.7$  ( $\psi = 35^\circ$ ) from one experiment.

- Croft (1980) determined a best-fit surface  $Z = 2.5$ – $2.9$  ( $\psi = 35^\circ$ – $39^\circ$ ) from crater and ejecta-blanket models of the Meteor Crater and Prairie Flat events.
- Austin et al. (1981) found, in Lagrangian calculations of excavation flow, that  $Z$ -values near the surface fall into the range of  $Z = 2.5$ – $3.0$  ( $\psi = 35^\circ$ – $45^\circ$ ) by simulating small laboratory experiments.
- Cintala et al. (1999) used strobed laser-light images to directly measure the flight of large, coarse sand particles in normal-incidence laboratory impacts, to find that ejection angles generally decrease over crater growth: beginning at about  $45^\circ$ – $55^\circ$  at  $0.2 R_g$  and dropping to about  $35^\circ$ – $45^\circ$  at  $0.6 R_g$  (Figs. 9 and 11).
- Anderson et al. (2003) used a laser imaging system to directly measure the flight of fine sand particles in normal- and oblique-incidence laboratory impacts, to find that normal-incidence ejection angles generally decrease over crater growth: beginning at about  $52^\circ$  at  $0.2 R_g$  and dropping to about  $44^\circ$  at  $0.5 R_g$ .

There seems to be widespread agreement in the literature that particle ejection angles decrease over the course of crater growth, but the form of that decrease is not so clear. Early modelers, such as Thomsen et al. (1980b) assumed that  $Z$  near the surface is constant, but that the initial depth-of-burial of the impactor would create initially high ejection angles, which then rapidly decrease with increasing  $r$  to stabilize at some constant value. More recent laboratory experiments, such as those described in Cintala et al. (1999) and Anderson et al. (2003), show a roughly linear decrease in ejection angles over the first half of

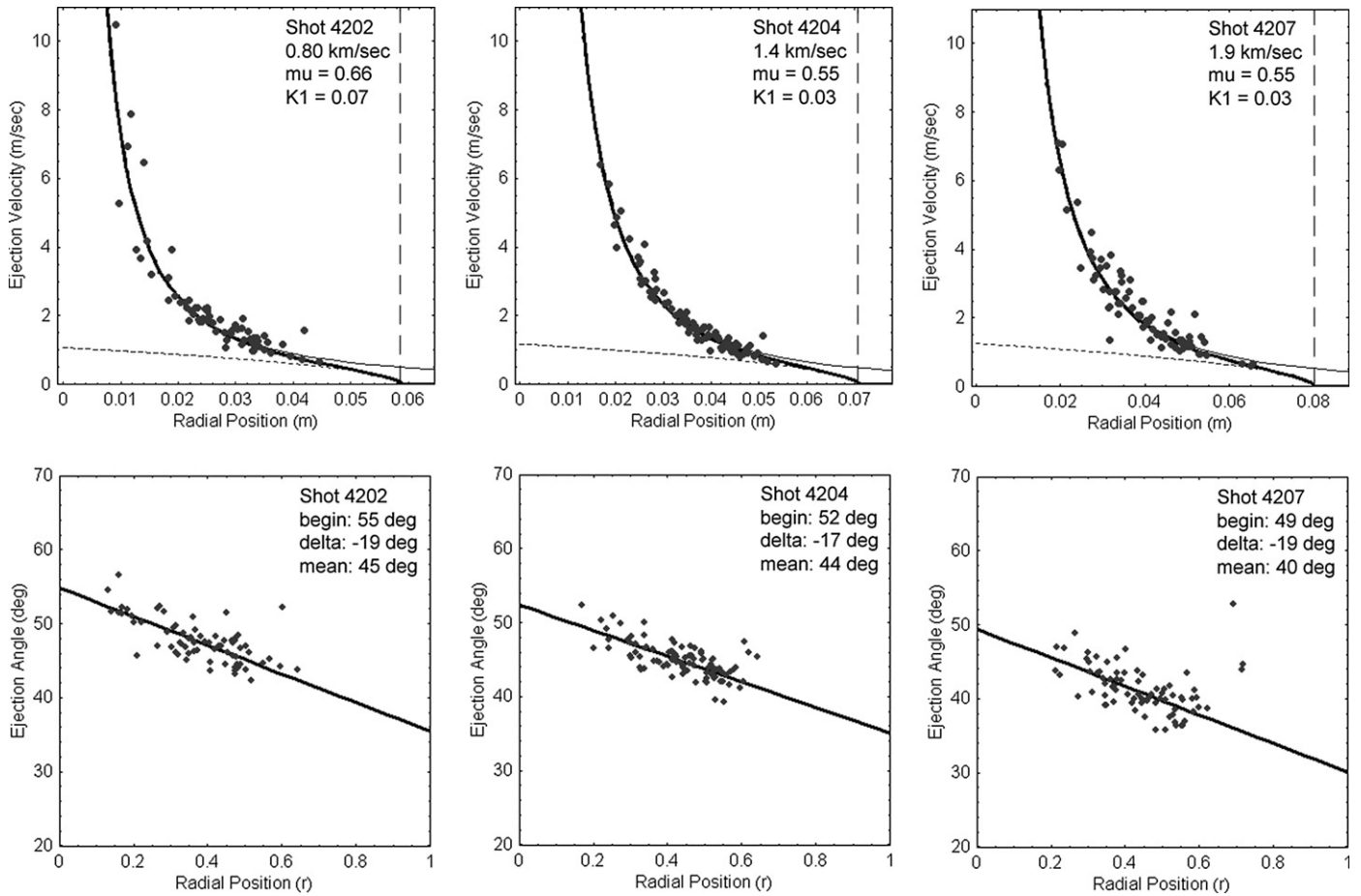


Fig. 9. *Top row*: a comparison of our ejecta velocity model (Eq. (41)) with three of the seven shots described in Cintala et al. (1999), showing good agreement with each. Legend: *thin solid line* = emergence velocity curve  $v_e$  (Eq. (29)); *thin dotted line* = overturn-flap function  $v_o$  (Eq. (42)), hinged at the computed gravity-dominated crater radius  $R_g$ ; *thick solid line* = zero-strength (gravity-dominated) effective velocity curve  $v_{ef}$  (Eq. (41)); *thin dashed line* = computed gravity-dominated crater radius  $R_g$ . *Bottom row*: linear, least-squares fits to the ejection angle data from three of the seven shots described in Cintala et al. (1999), demonstrating that a linearly decreasing ejection angle as a function of radius  $r$  is a reasonable assumption for each shot.

Table 2  
Model input parameters

| Name             | Symbol   | Nominal value           | Value range |
|------------------|----------|-------------------------|-------------|
| Impactor radius  | $a$      | 0.5 m                   | –           |
| Impactor density | $\rho_i$ | 700 kg m <sup>-3</sup>  | –           |
| Impactor mass    | $m_i$    | 366 kg                  | –           |
| Impactor speed   | $v_i$    | 10.2 km s <sup>-1</sup> | –           |
| Impact angle     | $\phi$   | 34°                     | 29°–39°     |
| Scaling constant | $\mu$    | 0.4                     | 0.35–0.4    |
| Scaling constant | $K_1$    | 0.2                     | 0.1–0.2     |
| Scaling constant | $K_{Tg}$ | 0.85                    | 0.75–0.95   |

cavity growth, but these appear to level off or even turn upward again as cavity growth continues. However, because these laboratory experiments take place in small target containers, these experiments may be seeing the effects of shock-wave reflection from the bottom and sides of those containers. The shock-wave reflection from the bottom of the container would tend to add to the vertical component of ejecta velocities, while the shock-wave reflection from the side of the container would tend to subtract from the radial component of ejecta velocities: both effects tending to increase particle ejection angles. The low-

est speed ejecta, near the end of crater growth, would be the most susceptible to this effect, such that the leveling-off, and in particular, the upturn in ejection angles near the end of crater growth may be an artifact of the laboratory environment.

Very recent CHD modeling, described in Collins and Wünnemann (2007), indicates a continuous, monotonically decreasing ejection angle with cavity growth. Their numerical simulations display a drop of about 5°–10° between 0.2 and 0.8  $R_g$ , without any leveling-off or upturn, and where the initial ejection angle is dependent upon the material's internal friction coefficient. For our first-order ejecta plume model, therefore, we adopt a simple, linearly decreasing ejection angle  $\psi_n$  for impacts at normal incidence, as a function of distance  $r$  from the impact site:

$$\psi_n(r) = \psi_o - \psi_d \left( \frac{r}{R_g} \right), \quad (44)$$

where the values for the starting angle  $\psi_o$  and total drop  $\psi_d$  will be adjusted during the course of our forward model iterations (Section 4.1.2). As a starting point, we will use the seven laboratory shots described in Cintala et al. (1999), which in their linear, least-squares fits show starting angles of  $\psi_o = 52.4^\circ \pm 6.1^\circ$

and total angular drops of  $\psi_d = 18.4^\circ \pm 8.2^\circ$ , using  $2\sigma$  errors (Fig. 9).

### 2.5. The effects of oblique impact

The last ingredient needed prior to handing the model off to the three-dimensional motion integrator (Section 3) is to add in the first-order effects of an oblique impact. This is important to this study because the impactor–spacecraft for Deep Impact struck the regional surface at an impact angle of  $\phi = 34^\circ \pm 5^\circ$  (measured from the horizontal). Such an oblique impact will affect the cratering event in four basic ways: the transient crater volume and size will be smaller; particle ejections angles will be lowered on the down-range side of the ejecta plume; particle ejection velocities will be higher on the down-range side of the ejecta plume; and the ejecta plume mass-loading will be shifted toward the down-range side. The first three of these effects can be reasonably approximated and included in our model.

For some time now, it has been recognized that craters produced by oblique impacts will maintain their circular shape and paraboloid profiles all the way down to impact angles of  $\phi \approx 10^\circ\text{--}15^\circ$  (Gault and Wedekind, 1978; Pierazzo and Melosh, 2000). This is because, as described in Sections 1.1 and 2.1, the established excavation flow-field is a function of two things: the outwardly propagating shock-wave generated by the impact, which will maintain a hemispherical shape and appear to originate from a point-source even in oblique impacts; and the rarefaction-wave, which is a function of shock-wave reflection from the free surface of the target (regardless of impact angle). The obliqueness of the impact does, however, play an important role in determining the amount of impactor energy and momentum which goes into setting up the overall crater excavation. In an extensive series of experiments, Gault and Wedekind (1978) showed that it is the *vertical component* of the impactor’s kinetic energy and momentum which governs the crater size, following a simple sine relationship: a result also supported by more recent work (Chapman and McKinnon, 1986; Elbeshhausen et al., 2007). As such, our applications of the crater (Section 1.3) and ejecta (Section 2.2) scaling relations will use  $v_i \sin \phi$  to obtain the applicable component of the impactor’s velocity.

On the other hand, some fraction of the *horizontal component* of the impactor’s kinetic energy and momentum is transferred to the excavation flow-field, such that it causes an increase in down-range directed, horizontal particulate motion and manifests itself as an overall increase in velocities and a lowering of particle ejection angles on the down-range side of the ejecta plume. With regard to how much ejection angles and velocities change with impact obliqueness, there are no scaling relationships to draw upon: only direct experimentation and some three-dimensional CHD models. For this work, we will make use of the recently published experimental data on ejection angles and velocities contained in Anderson et al. (2003), Anderson et al. (2004), and Schultz et al. (2005) to produce an empirical rule for use in our model. This function uses an altitude-azimuth coordinate system, where  $r$  is the particle distance from the impact site,  $\theta$  is the particle azimuth as mea-

sured from the direction of the incoming projectile, and  $\phi$  is the impact angle of the projectile (normal incidence occurs at  $\phi = 90^\circ$ ):

$$\psi_f(r, \theta) = \psi_n - \left[ 30^\circ (\cos \phi) \left( \frac{1 - \cos \theta}{2} \right) \left( 1 - \frac{r}{R_g} \right)^2 \right]. \quad (45)$$

The change in the overall ejection velocity for a particle is determined directly from this change to its ejection angle (Eq. (45)), assuming that all of this ejection angle change is the result of an addition made to the *horizontal* velocity component of the particle. The final ejection velocity  $v_f$  at oblique-impact incidence, as a function of the final ejection angle  $\psi_f$ , is thus given by:

$$v_f(r, \theta) = \left[ (v_{ef} \sin \psi_n)^2 + \left( \frac{v_{ef} \sin \psi_n}{\tan \psi_f} \right)^2 \right]^{\frac{1}{2}}. \quad (46)$$

Fig. 10 shows a plot of Eqs. (45) and (46) for a projectile coming in at  $\phi = 30^\circ$ , as compared to the experimental data published in Anderson et al. (2003). While the fit is reasonable, it is certainly not excellent, particularly where velocities are concerned in the later stages of measured plume expansion. However, this is at least a first step toward incorporating these effects into an impact ejecta model, and the fit does verify that the majority of the change in ejection angles and velocities occurs through a down-range directed addition to the horizontal velocity component of the ejecta.

One final effect which will *not* be included in this model is the down-range shift in ejecta plume mass-loading that is seen both in experiments and in its effect on the ejecta blankets of existing simple craters (Melosh, 1989; Pierazzo and Melosh, 2000). Below about  $\phi = 45^\circ$ , the ejecta plume (and resulting ejecta deposit) becomes increasingly asymmetrical and begins to develop a gap in its up-range side, called a “forbidden zone” or “zone-of-avoidance.” This gap becomes larger and more prominent at lower impact angles, and at very low impact angles ( $\phi < 5^\circ$ ), the ejecta plume also develops a down-range gap, which produces a “butterfly” pattern in the resulting ejecta blanket (Pierazzo and Melosh, 2000). The Deep Impact event, impacting at  $\phi = 34^\circ \pm 5^\circ$  above the regional horizon, almost certainly produced an asymmetrical ejecta distribution, and hints of an up-range gap can be seen in the ejecta plume images. However, at this stage in the science, we lack the means to include even a simple, empirically based modification to the model to incorporate this effect, and this omission should be kept in mind when comparing the simulation to the actual images.

### 3. Model computational development

Up to this point, we have described only the theoretical development of the model, which goes into establishing the launch conditions of the impact ejecta particles. In this section, we describe the computational development of the model, which determines the forces on the individual particles once launched, and traces their flight over time to either landing or escape.

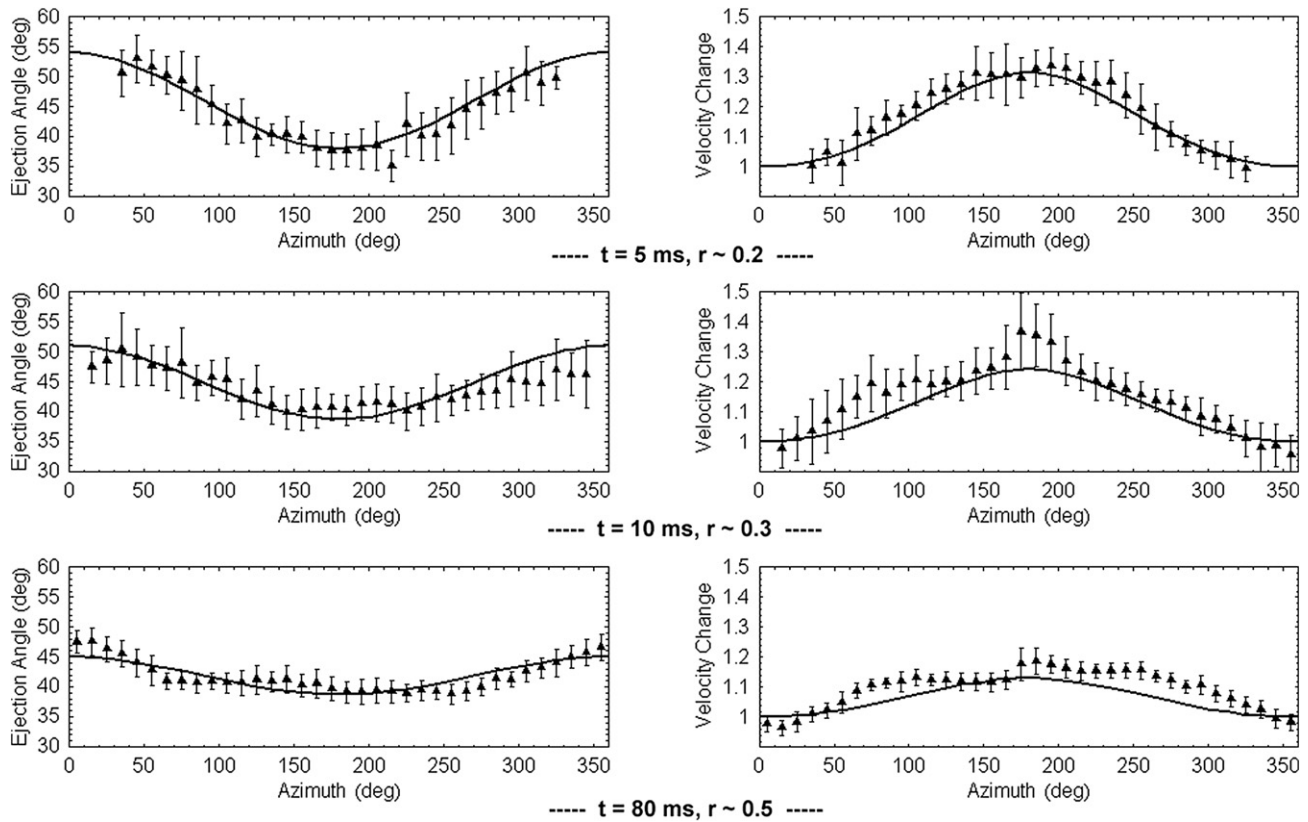


Fig. 10. The effects of a  $\phi = 30^\circ$  oblique impact on particle ejection angles (left) and normalized ejection velocities (right), both shown as a functions of azimuth angle from the impactor direction  $\theta$ , where each pair of curves shows the effect on ejecta produced at different distances  $r$  from the impact site. The data points are taken from Anderson et al. (2003), shown with  $1\sigma$  error bars, while the curves represent our empirical function fit to this data set, given by Eqs. (45) and (46). For this data set, the best fit to  $\psi_n$  (Eq. (44)) occurs at  $\psi_o = 60^\circ$  and  $\psi_d = 30^\circ$ .

### 3.1. Ejecta plume behavior in two dimensions

The simplest form of this ejecta behavior model is one which operates in two spatial dimensions (horizontal and vertical motion only), under the influence of a uniform gravity field. This permits us to use the standard equations of motion for ballistic flight (flat target-surface and no atmospheric drag effects) to simulate the ejecta behavior produced by small, vacuum-chamber, laboratory experiments done on Earth. Under these simple conditions, the equations of motion become:

$$x(t) = x_l + v_f \cos \psi_f (t - t_l), \quad (47)$$

$$y(t) = v_f \sin \psi_f (t - t_l) - \frac{1}{2} g (t - t_l)^2, \quad (48)$$

where  $x$  and  $y$  are the horizontal and vertical ejecta particle positions, respectively;  $x_l$  is the horizontal launch position of the ejecta particle; and  $t_l$  is the launch time of the ejecta particle.

To start the model, ten inputs are required: four for the impactor ( $a$ ,  $\rho_i$ ,  $v_i$ ,  $\phi$ ), four for the target surface ( $\rho_t$ ,  $\bar{Y}$ ,  $\mu$ ,  $K_1$ ), the gravity field magnitude  $g$ , and the crater-centered azimuth of the ejecta plume “slice” to be studied  $\theta$ . From these inputs, the transient crater volumes  $V_g$  and  $V_s$  are computed using Eq. (10), for both the condition of zero strength and the user supplied strength value  $\bar{Y}$ . These two volumes are then converted to transient crater radii  $R_g$  and  $R_s$  (Eq. (11)), respectively, where both crater radii are needed by the ejecta scaling

relationships (Sections 2.2 and 2.3). Next, the desired crater radius  $r$  is populated with two sets of several thousand tracer particles, each assigned a launch position  $x_l$  between the projectile radius  $a$  and transient crater radius  $R_s$ , with a launch velocity  $v_f$  (Eq. (46)) and ejection angle  $\psi_f$  (Eq. (45)) computed for each particle. One set of tracer particles are used to mark the position of the leading edge of the ejecta plume, and are launched at time  $t_l = 0$ . The second set of tracer particles are used to mark the position of the trailing edge of the ejecta plume, and are launched sequentially at time  $t_l = t(r)$  from Eq. (27). This form of the model is easily handled by a computational mathematics package, such as *Maple*, *Matlab*, or *Mathematica*, with the result displayed using standard plotting techniques.

Fig. 11 shows a comparison of this form of the model to a small laboratory shot described in Cintala et al. (1999). The upper two panels of this figure show a one-to-one matching of the model to the photograph of shot 4035, with excellent agreement (only the leading edge of the ejecta plume is depicted in these panels). The lower two panels expand upon this laboratory-shot recreation and show both the leading and trailing edges of the ejecta plume, along with the trajectories of some individual tracer particles, under conditions of both gravity- and strength-dominated cratering. The model does a very good job of displaying the evolution of the ejecta plume shape throughout crater growth, without having to model the streamline flow below ground level (compare the lower left panel of Fig. 11



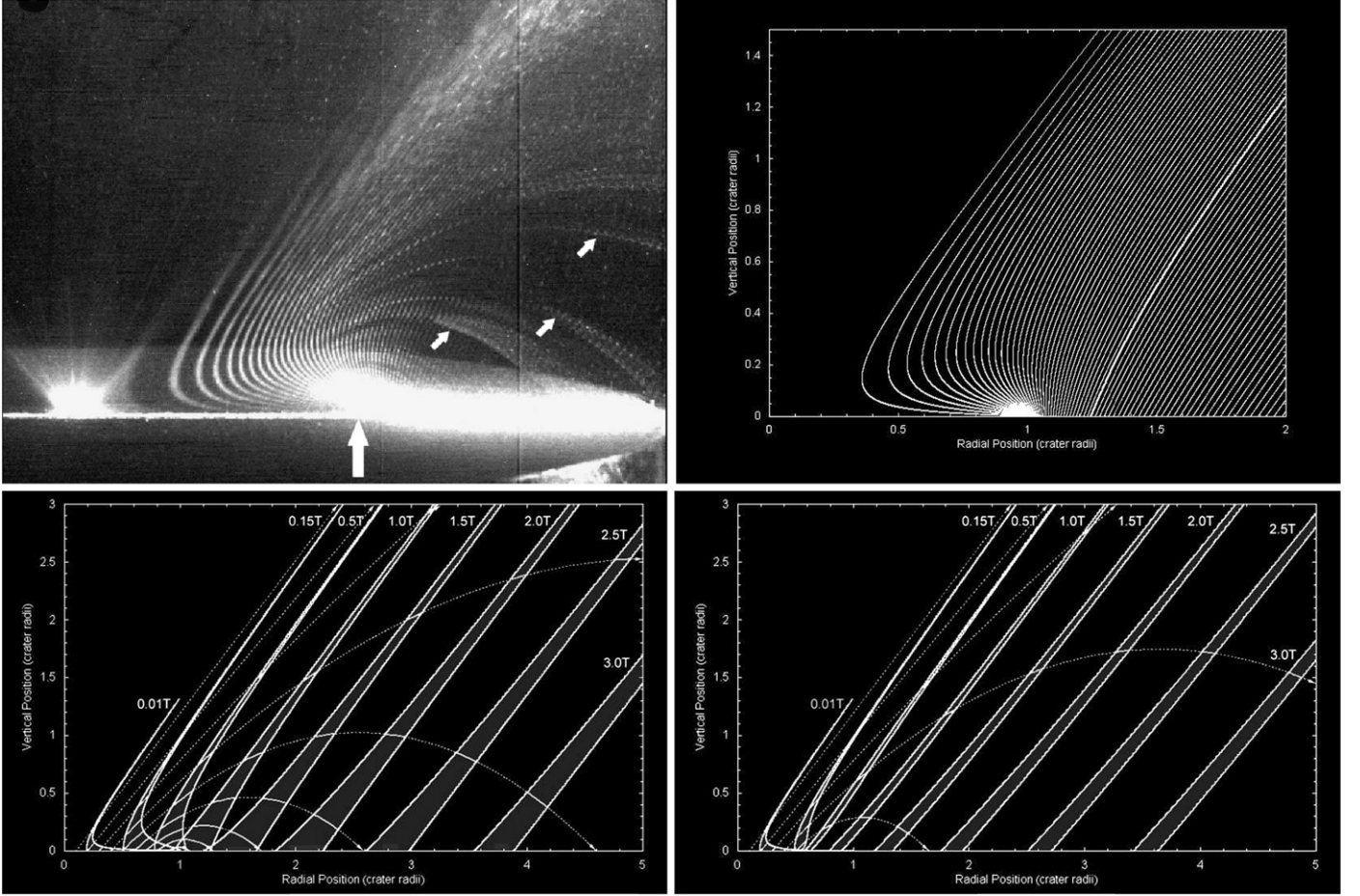


Fig. 11. (*Upper left*) A photograph of shot 4035 from Cintala et al. (1999), into fine sand, where the leading edge of the impact ejecta plume is illuminated from the right by a vertical sheet of laser light, which was turned on for 0.2 ms at 2 ms intervals. The large arrow marks the approximate location of the transient crater rim, while small arrows mark the ballistic path of a few large particles. (*Upper right*) A model recreation of shot 4035 (Cintala et al., 1999), with the position of the ejecta plume's leading edge shown at 2 ms intervals. The bold line marks the position of the plume at crater formation time  $T_g$ . All distances in these plots are normalized to the crater radius  $R_g$ . (*Lower left*) A model of the same shot, only in these lower plots, larger scales are shown and both leading and trailing ejecta plume edges are modeled (and filled between). Dotted lines mark the ballistic path of the particles in nine individual streamlines. All times are normalized to the crater formation time  $T_g$ . (*Lower right*) A model of the same shot again, but with  $\bar{Y} = 10$  kPa of strength added to the target. Although this creates a crater of about half the diameter as before, and a much thinner ejecta plume, the plume advances at roughly the same rate.

to Fig. 6). Of key importance to the analysis of the Deep Impact event is the effect of adding strength to the model (the lower right panel): while the mass-loading in the ejecta plume is significantly decreased, resulting in a thinner ejecta plume in the simulation, the advancement rate of the plume is not significantly affected. This is because the particles which make up the plume in its later advancement stages are ejected early enough in the process to have a high inertia (kinetic energy) and are not significantly effected by either strength or gravity in Eq. (41). To simulate the Deep Impact event, however, a more sophisticated form of the model is required, which operates in three spatial dimensions and can trace the motion of each tracer particle under the influence of the non-uniform gravity field produced by a small, rotating, irregular target body.

### 3.2. The ejecta plume as a polygon shape-model

To bring our ejecta plume model into three dimensions, we introduce the concept of modeling the ejecta plume as a poly-

gon shape-model. Rather than using thousands of randomly placed tracer particles to mark the ejecta plume, such as in previous studies (Geissler et al., 1996; Durda, 2004), we instead launch two networks of tracer particles, one network to depict the leading edge of the ejecta plume, and one to depict the trailing edge of the ejecta plume. The tracer particles in each network are connected to form the vertices of triangular polygons which are, in turn, connected to form a continuous surface for both leading and trailing sides of the plume. To be more specific, the polygon ejecta plume is made by placing two meshes of 1800 regularly spaced tracer particles on the starting surface area of the computed transient crater, such that 3540 triangular polygons are formed in each mesh (these meshes initially lie one directly on top of the other). For each mesh, this arrangement creates 59 radial rings of 60 polygons each, ranging from one projectile diameter  $d$  to the transient crater radius  $R_s$  in distance from the impact site. The  $2d$  diameter hole in the center of the mesh is intentional, to avoid the region of potential vapor plume creation (Section 1.1). Particles in the top mesh are

ejected immediately after impact (time  $t = 0$ ) and mark the position of the leading edge of the ejecta plume, while particles in the bottom mesh are ejected sequentially at time  $t(r)$  from Eq. (27), and mark the position of the trailing edge of the ejecta plume.

An opacity (or transparency) is computed for each plume polygon at each time-step in the simulation, which is a function of three things: (a) its mass-loading, (b) its surface area, and (c) the ejecta particle size distribution (PSD). That is, as the ejecta plume expands and the mass of ejecta represented by a given plume polygon is spread out over a much larger area, the opacity of that polygon will decrease.

We calculate the mass of ejecta that each polygon represents by dividing the excavated portion of the transient crater into a series of simple paraboloid shells. The mass of material injected into each ring of polygons is thus given by

$$m_{ri} = \frac{1}{9}\pi\rho_t(r_{i+1}^3 - r_i^3), \quad (49)$$

where  $m_{ri}$  is the mass injected into ring  $i$  and we assume that the excavation depth of the transient crater is about  $D/9$  or  $R/4.5$  (Melosh, 1989). This paraboloid shell approach is an approximation to the more exact way of computing the excavated mass, done by using a numerical integration between streamtubes in the Maxwell Z-model (Section 2.1). Comparison between the two methods has shown that the paraboloid shell approximation yields results that are within 3–4% of the numerical Z-model integration (depending up Z value), such that the added accuracy of a full integration was deemed not worth the additional computation time.

We define the mass per individual polygon in a given ring as  $m_\Delta = m_{ri}/120$  (there are  $2 \times 60 = 120$  polygons per ring), with the mass divided equally between leading and trailing edge plume polygons. This mass-loading per polygon  $m_\Delta$  will remain constant throughout the simulation, while the surface area of each polygon  $\Lambda_\Delta$  will change dramatically throughout its flight.

Along with the target density  $\rho_t$  and an individual particle density  $\rho_p$ , the model also requires a particle size distribution (PSD) description, given in the form of a segmented (piecewise), cumulative power law. This is done by providing values for the smallest and largest particle diameters at the boundary of each segment in the PSD, along with a cumulative power-law exponent for that segment. Each segment of the distribution is described by the expression:

$$dN = Km_p^{-b} dm_p, \quad (50)$$

where  $N$  is the cumulative number of particles,  $K$  is a temporary constant,  $m_p$  is the particle mass, and  $b$  is the supplied power-law exponent.

From this expression, we can derive the basic optical scattering properties of each ejecta plume polygon, which is a function of the optical scattering properties of each individual particle. The reflection-surface area of an individual particle is given by

$$\Lambda_p = \pi \left( \frac{3m_p}{4\pi\rho_p} \right)^{\frac{2}{3}}. \quad (51)$$

Building upon this, the plume's surface area per unit volume  $\Lambda_v$  can be found by solving the differential equation  $d\Lambda_v = \Lambda_p dN$ , which yields

$$\Lambda_v = \pi \left( \frac{3}{4\pi\rho_p} \right)^{\frac{2}{3}} \left[ \frac{K}{\frac{5}{3} - b} \right] \left[ m_l^{\frac{5}{3}-b} - m_s^{\frac{5}{3}-b} \right], \quad (52)$$

where  $m_l$  and  $m_s$  are the mass of the largest and smallest particles, respectively, in that segment of the particle distribution.

We can eliminate the temporary constant  $K$  by first placing it in terms of the plume's mass per unit volume  $m_v$ , which is found by solving the differential equation  $dm_v = m_p dN$ . This gives

$$m_v = \left[ \frac{K}{2-b} \right] \left[ m_l^{2-b} - m_s^{2-b} \right]. \quad (53)$$

We now divide the expression for the surface area per unit volume,  $\Lambda_v$  (Eq. (52)), by the expression for the mass per unit volume  $m_v$  (Eq. (53)) to eliminate  $K$  and obtain an expression for the plume's surface area per unit mass  $\Lambda_m$ . This gives

$$\Lambda_m = \frac{\Lambda_v}{m_v} = \pi \left( \frac{3}{4\pi\rho_p} \right)^{\frac{2}{3}} \left[ \frac{2-b}{\frac{5}{3}-b} \right] \left[ \frac{m_l^{\frac{5}{3}-b} - m_s^{\frac{5}{3}-b}}{m_l^{2-b} - m_s^{2-b}} \right], \quad (54)$$

where the surface area per unit mass  $\Lambda_m$  is an intrinsic property of the ejecta plume, independent of the mass-loading  $m_\Delta$  or surface area  $\Lambda_\Delta$  of each plume polygon. This calculation is done for each segment of the particle distribution, and the results combined linearly, such that  $\Lambda_m = \Lambda_{m1} + \Lambda_{m2} + \dots$ .

To determine the opacity of an individual ejecta plume polygon as a function of its changing surface area  $\Lambda_\Delta$ , we make use of the Lambert exponential absorption law (Chamberlain and Hunten, 1987):

$$I_f = I_o e^{-\frac{\Lambda_m m_\Delta}{\Lambda_\Delta}}, \quad (55)$$

where  $I_o$  is the initial light intensity, and  $I_f$  is the final light intensity. The exponent  $(\Lambda_m m_\Delta)/\Lambda_\Delta$  is dimensionless and equivalent to the optical depth of the plume polygon. Normalizing this light intensity gives us an opacity  $O_\Delta$  equation for each ejecta plume polygon:

$$O_\Delta = 1 - e^{-\frac{\Lambda_m m_\Delta}{\Lambda_\Delta}}, \quad (56)$$

where  $\Lambda_\Delta$  is a function of time and the position of the three tracer particles which make up the plume polygon's vertices, while  $\Lambda_m$  and  $m_\Delta$  remain constant. In addition to computing its opacity  $O_\Delta$ , the rendering of each plume polygon (in each model-produced synthetic image) includes a simple Lambertian photometric function (McEwen, 1991) as part of the *OpenGL* model viewer. This plume brightness computation, however, does *not* take into account the variable albedo of the particles to different light wavelengths, nor the difference in scattering properties between back-scattered and forward-scattered light at various phase angles. Therefore, our simple plume brightness model represents only a first approximation to an actual ejecta plume; and as such, the results presented in Section 4 will be qualified to take this into account.

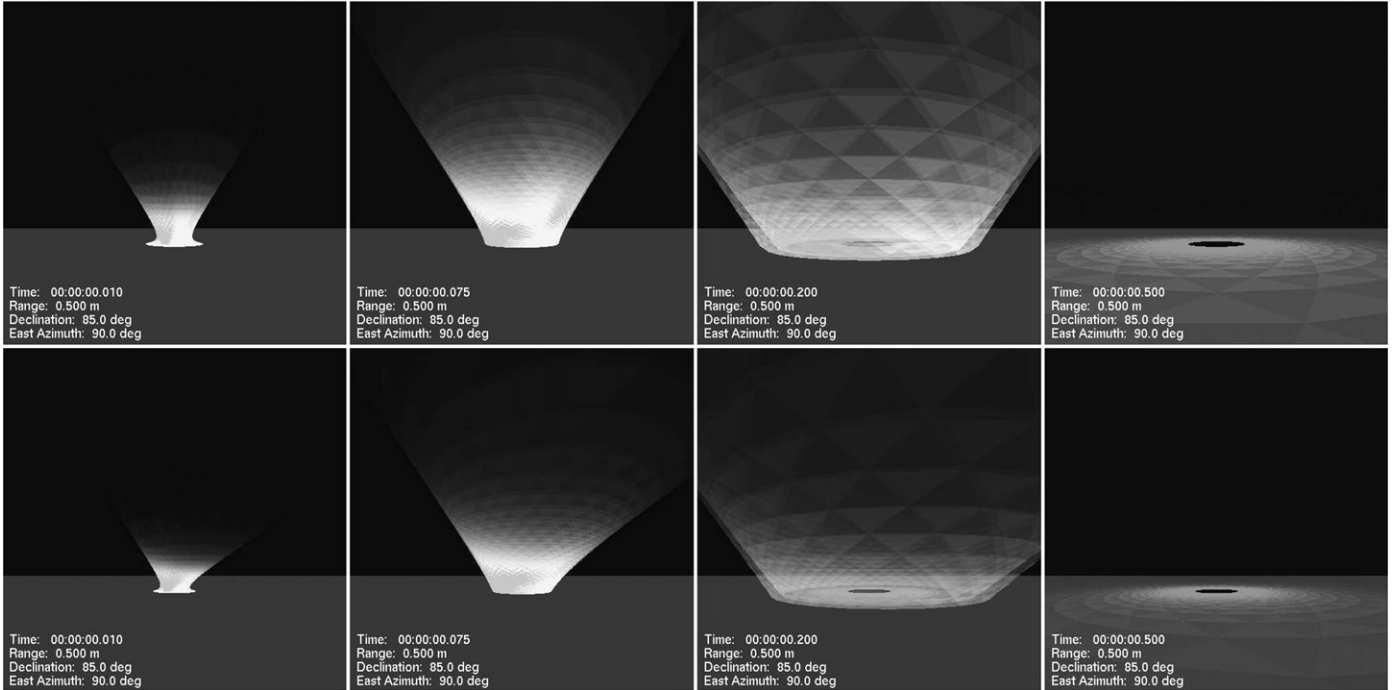


Fig. 12. A three-dimensional model of a small laboratory shot (a 3 mm impactor traveling at  $1.25 \text{ km s}^{-1}$  striking a fine-grade sand target) for both normal-impact incidence  $\phi = 90^\circ$  (upper images) and oblique-impact incidence  $\phi = 30^\circ$  (lower images). The projectile enters from the left ( $0^\circ$  East azimuth) in both simulations. The ejecta plume is rendered via *OpenGL*, using two networks of tracer particles to mark both its leading and trailing edges, which are then connected to form triangular polygons. The opacity of each plume polygon is a function of its changing surface area, its initial mass-loading, and the given particle size distribution (PSD). In this case, sand particles of 0.5–1.0 mm diameter were simulated, with a power-law exponent of  $b = 1.0$  and an individual particle density of  $\rho_p = 2500 \text{ kg m}^{-3}$ .

Fig. 12 shows a demonstration of this three-dimensional polygon-plume ejecta model for two simulated laboratory experiments: one at normal incidence, and one at oblique incidence (displaying the effects described in Section 2.5). The oblique impact produces a crater which is smaller, and the resulting ejecta plume is therefore thinner and less opaque than the one produced by the impact at normal incidence. In both cases, a fine grade (0.5–1.0 mm diameter grain) sand target was simulated, with an assumed power-law exponent of  $b = 1.0$  and a grain density of  $\rho_p = 2500 \text{ kg m}^{-3}$ .

### 3.3. The comet as a polygon shape-model

As part of the Deep Impact mission, mapping and shape-modeling were performed for the nucleus of Comet 9P/Tempel 1 using the methodology described in Thomas et al. (2005) and with the final results described in Thomas et al. (2007). For our ejecta plume modeling, we make use of the  $6^\circ$  ( $\sim 300 \text{ m}$ ) resolution polygon shape-model of Tempel 1 produced from that work, which is now part of the Planetary Data System (PDS). In addition, we make use of the provided information on the impact site, mean radius, and rotation state of the comet (Thomas et al., 2007). This information allows us to simulate the ejecta plume produced by an impact on the rotating shape-model at a given location on the body, from an impactor coming in at a given speed and direction, with the entire scene illuminated from a specified sun direction. What is needed next then, is a method for computing the non-uniform gravitational force from

this small, irregular body on each ejecta tracer particle, at each time-step after launch.

The most common method for computing the gravitational acceleration at some given location outside of an irregular body is to perform a numerical integration over the volume of the body, which has been filled with thousands of tiny, individual mass elements (Geissler et al., 1996). This method is computationally expensive, however, and for this study we make use of the surface-polyhedron gravity technique developed by Werner (1994), which takes advantage of Gauss's Law applied to a shape whose surface has been divided into individual polyhedron elements. Using this method, the integration occurs over the surface area of the body, which saves significant computation time and produces a result which is of better quality than most volume integrators (Werner, 1994). In addition to computing the gravitation force on each tracer particle, the model can include a specified acceleration due to solar radiation pressure, which will be applied to each tracer particle (not in the comet's shadow) in the anti-solar direction. At each time-step in the simulation, these two forces are computed for each tracer particle, with the particle's ballistic flight then tracked using a standard Bulirsh–Stoer ODE integrator (Press et al., 1992). The model tracks all tracer particles until they have either left the gravitational sphere of influence of the nucleus (escaped) or landed again on the comet's surface.

In addition to modeling the comet nucleus, its gravity field, and the ejecta plume resulting from Deep Impact as a function of time, we make use of the instrument specifications described in Hampton et al. (2005), the comet and spacecraft



trajectory information contained within the *SPICE* system, and the telemetry and image information provided as part of each image produced by Deep Impact to model the image sequence captured by the flyby-spacecraft's High Resolution Instrument (HRI). That is, while the impact ejecta plume model is running, we “fly” our model viewer's camera past the scene in such a way as to simulate the views captured by the actual Deep Impact flyby-spacecraft. Examples of this HRI image-sequence simulation can be seen in Figs. 14, 16, 20, 21, and 22.

#### 4. Deep Impact modeling results

The primary advantage of the Deep Impact mission, as an impact-cratering experiment, is that the properties of the impactor-spacecraft ( $a$ ,  $\rho_i$ ,  $m_i$ ,  $v_i$ ) are fully known, along with several impact properties for which we can make reasonable estimates ( $\mu$ ,  $K_1$ ,  $K_{Tg}$ ,  $\phi$ ): these are summarized in Table 2. This leaves the impact-related properties of the comet's surface ( $g$ ,  $\rho_t$ ,  $\bar{Y}$ ) as the principal unknowns to be found. Using the model described in the previous three sections, our primary goal is to place constraints on the magnitude of the gravity field  $g$  in which the ejected particles were ballistically traveling—leading to a measure of the mass  $m_t$  and bulk density  $\rho_t$  of Comet Tempel 1. To achieve this, however, we must first place constraints on the position of the ejecta cone axis  $\chi$  as seen from the flyby-spacecraft, and on the particle ejection angles  $\psi$  produced by the crater excavation flow. Additionally, we will address the issues of the effective yield strength  $\bar{Y}$  of the comet's surface at the impact site, as well as the likely magnitude of accelerations due to solar radiation pressure and other forces on the ejected particles.

##### 4.1. Ejecta plume geometry

The view of the emerging and expanding solid-particle ejecta plume provided to us by the flyby-spacecraft places relatively tight constraints on the range of possible particle ejection angles and the overall position of the axis of the conical ejecta plume. Fig. 1 shows the four basic phases of progression through which our view of the Deep Impact ejecta plume evolved over the course of the observation. In phase 1 (upper left panel), the emerging ray structure of the ejecta plume indicates that during the first  $\sim 2$  min after the impact, the flyby-spacecraft viewed the *interior* of the ejecta cone. By phase 2 (upper right panel), which lasted from about 2 to 9 min after the impact, this view had changed to one which showed the ejecta plume almost, but not quite, in profile view: with the east (lower right) portion of the ejecta cone seen nearly broadside and the west (upper left) portion of the ejecta cone seen nearly edge on. Near the time of closest approach, from about 9 to 13 min after the impact, the view shifted to that shown in phase 3 (lower left panel), in which the flyby-spacecraft was again looking into the interior of the ejecta cone and was able to peer all the way down to the bottom and image the dark, oval outline of the expanding plume base against the comet's surface. Finally, in phase 4 (lower right panel), the flyby-spacecraft viewed the exterior of the slowly expanding ejecta cone, at a

near-profile (near-perpendicular) angle to the camera, without extreme foreshortening.

##### 4.1.1. Ejecta plume axis orientation

In addition to reconciling these four viewing phases over which the ejecta plume evolved over the course of the observations, two additional factors play an important role in constraining the axis orientation of the ejecta plume: (1) the position angle, shape, and width of the shadow cast by the emerging ejecta plume on the surface of the nucleus (Fig. 13), and (2) the time at which the base of the conical ejecta plume, as seen from its interior, first became visible in the images (Fig. 14). Throughout this parameter search, an effort was made to find the solution which was simplest, and followed well-known (canonical) behavior for impacts into relatively low-strength target materials.

To investigate the shadow cast by the newly emerging ejecta plume we opted to use the Persistence of Vision Raytracer (*POV-Ray*, <http://www.povray.org>) model viewer rather than our own *OpenGL*-based model viewer. The advantage in using *POV-Ray* is that lighting and shadowing is computed down to the sub-polygon, pixel level, while our own routine only handles this down to the polygon level (and therefore has much lower shadow resolution). Fig. 13 shows the result of this exercise, in which the ejecta plume is depicted as a simple right-circular cone, anchored at its point to the impact site, and divided into two regions of different transparency. Three free parameters are used in the fit: the opening half-angle of the cone, its west–east tilt angle  $\chi_w$ , and its north–south tilt angle  $\chi_n$ : where directions are with reference to the comet shape-model coordinate system (in Fig. 13, north is to the upper right, west to the upper left) and the “tilt” is a measure of the degree of deviation from the direction of the regional surface normal vector at the impact site. Our goal was to match three things: the initial interior view of the ejecta cone, the clock position of the shadow cast by the ejecta cone, and the width of the shadow cast by the ejecta cone. Our initial expectation was that the ejecta cone axis should be coincident with the regional surface normal vector ( $\chi_w = 0^\circ$ ,  $\chi_n = 0^\circ$ ); however, this proved not to be the case, as panels A and B of Fig. 13 demonstrate. The best fit to all three conditions proved to be an ejecta cone which was tilted severely to the west,  $\chi_w = 45^\circ \pm 5^\circ$  and  $\chi_n = 0^\circ \pm 5^\circ$ , indicative of an impact on a westward-facing slope on a scale smaller than that used to create the comet's shape-model ( $< 300$  m). This is because, as mentioned in Sections 1.1, 2.1, and 2.5, the excavation flow direction is a function of not just the outwardly propagating shock-wave from the impact point, but also the shock-wave's reflection from the free surface of the target, which will follow the local topography near the impact site. This exercise also indicated an initial ejecta cone opening half-angle of  $30^\circ \pm 5^\circ$ , such that initial particle ejection angles  $\psi_f$  (Sections 2.4 and 2.5) should be relatively close to those seen in laboratory experiments (Figs. 9–12).

This severe ejecta cone axis tilt angle  $\chi$  was initially rather puzzling, in that our simulations showed that if this tilt is maintained throughout the event, *only* the view shown in phase 1, the upper left panel of Fig. 1, is properly matched by the simulation, while the remaining three views are incorrect: particu-



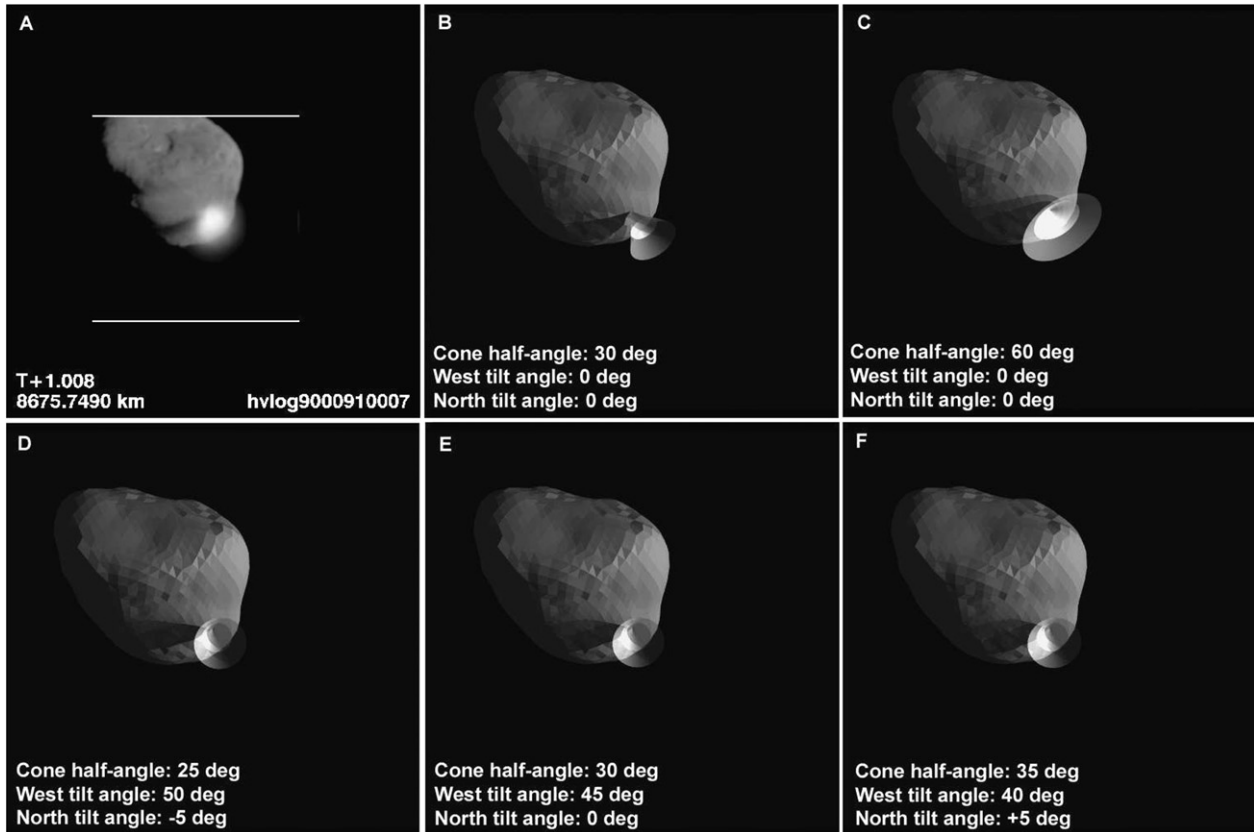


Fig. 13. (*Upper left*) The High Resolution Instrument (HRI) view of Comet Tempel 1 about one second after the impact (image HV9000910.007). In this image we see both the interior of the ejecta cone (somewhat foreshortened on its west side), and its very narrow shadow cast on the surface of the nucleus. (*Test fits A, B*) Two *POV-Ray* model attempts at using the regional surface normal vector as the ejecta cone axis and varying only the cone opening angle. In A, the shadow is narrow, but the cone exterior is viewed. In B, the cone interior is viewed, but the shadow is far too wide. (*Test fits C, D, E*) The three *POV-Ray* model best fits to image HV9000910.007, which permit both the plume opening angle and the plume axis position to be adjusted. These fits indicate an initial plume axis tilt toward the west (upper left in these images) of  $45^\circ \pm 5^\circ$  from the regional surface normal vector, and a plume opening half-angle of  $30^\circ \pm 5^\circ$ : matching the shadow width, shadow clock position, and plume interior view.

larly the final look-back view (lower right panel), in which the ejecta cone ends up tilted severely away from the camera. We therefore searched for a second point in the event at which to constrain the ejecta cone axis tilt angle  $\chi$  and found this in the transition point between phase 2 (Fig. 1, upper right panel) and phase 3 (Fig. 1, lower left panel). This transition point, during which time the dark oval of the plume's base becomes visible (Fig. 14), is primarily a function of the plume orientation and the changing spacecraft position during the flyby. Repeated model iterations indicated a best fit to the plume axis orientation shown in Fig. 14 of  $\chi_w = 5^\circ \pm 5^\circ$  and  $\chi_n = 0^\circ \pm 5^\circ$ , significantly closer to the determined regional surface normal vector. This plume orientation also gives us the best match to viewing phases 2, 3, and 4 of Fig. 1, indicating a significant change in the ejecta plume axis orientation  $\chi$  over the  $\sim 2$  min of phase 1: from  $\chi_w = 45^\circ \pm 5^\circ$  to  $\chi_w = 5^\circ \pm 5^\circ$ .

Fig. 15 summarizes these findings and our interpretation of this apparent change in the ejecta cone's orientation angle  $\chi$  over the course of the first two minutes following the impact. The impact apparently occurred on a *small*, westward-facing slope of roughly 1/3 to 1/2 the size of the transient crater. This irregular topography would have significantly affected the reflection of the impact shock-wave off the target's free surface,

which, in turn, would have severely altered the directions of the ejecta flow-field established. Although this local slope caused a spatial alteration in the ejecta flow-field, which occurred while all of the topography was still intact, we witnessed it as a temporal event due to the diverse power-law distribution of ejecta particle velocities (Fig. 8). From the flyby-spacecraft's perspective, we imaged the effect on the fastest-speed particles first (from the innermost portions of the crater), and then imaged increasingly slower particle populations as the plume evolved over time. Images of the impact area, taken by the impactor-spacecraft during its approach (Fig. 6 of A'Hearn et al., 2005b), do show sufficient irregular topography to support this hypothesis, even though the exact point of impact cannot be identified (Busko et al., 2007). It should be noted, however, that this explanation for the apparent shift in the ejecta cone's orientation angle  $\chi$  has not been validated by either laboratory experiment or CHD modeling, and at this stage amounts to an inference based upon the Maxwell Z-model of excavation flow only (i.e., more work needs to be done in this area).

#### 4.1.2. Ejecta particle launch angles

In addition to constraining the ejecta plume's axis orientation  $\chi$ , we can place constraints on the ejecta particle launch

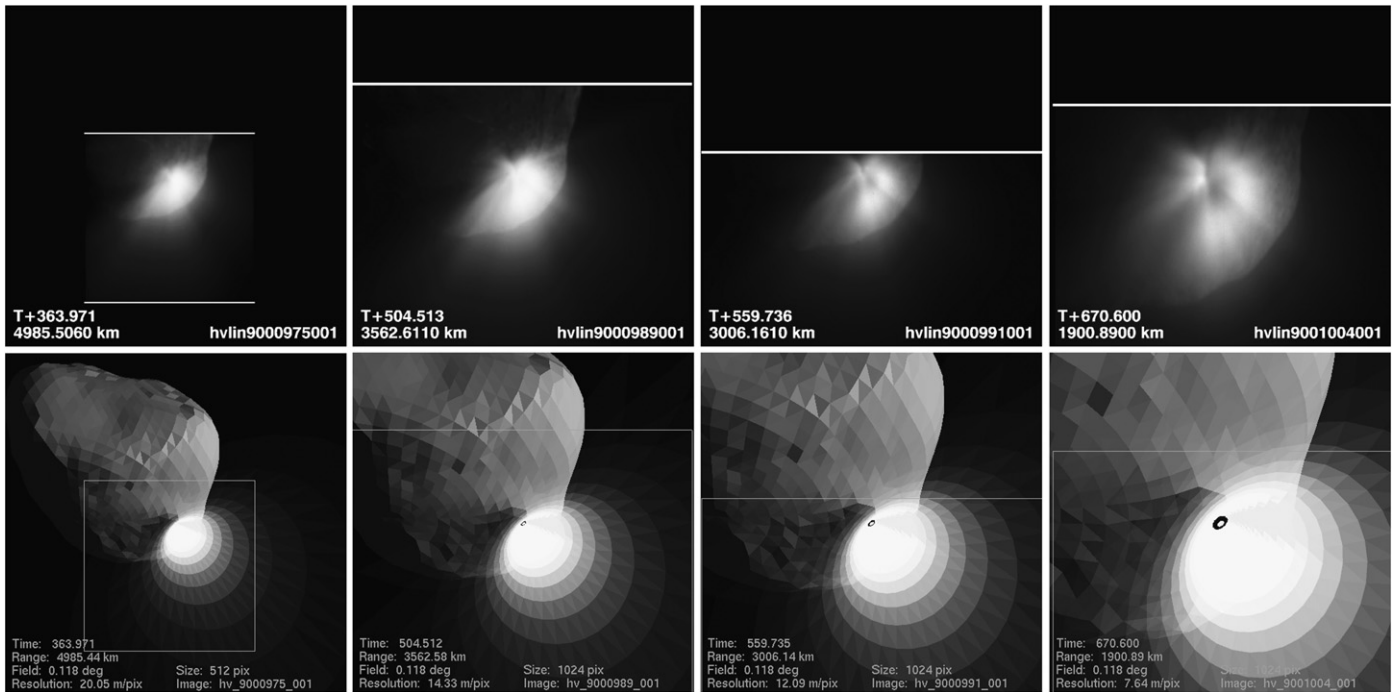


Fig. 14. (*Upper images*) A series of HRI images showing the gradual appearance of the dark, interior base of the ejecta plume during the flyby. A gap in the ejecta plume's southern (lower left) side is also revealed, producing a keyhole-like appearance. This event occurred over a time span of about 1 min, between roughly 9 and 10 min after the impact. The appearance of the plume base at this time is consistent with a final plume axis vector which was tilted to the west by only  $5^\circ \pm 5^\circ$  from the regional surface normal vector. (*Lower images*) A model simulation of the plume base emergence, demonstrating our interpretation of the event. The simulation does not include rays and gaps (ejecta plume irregularities).

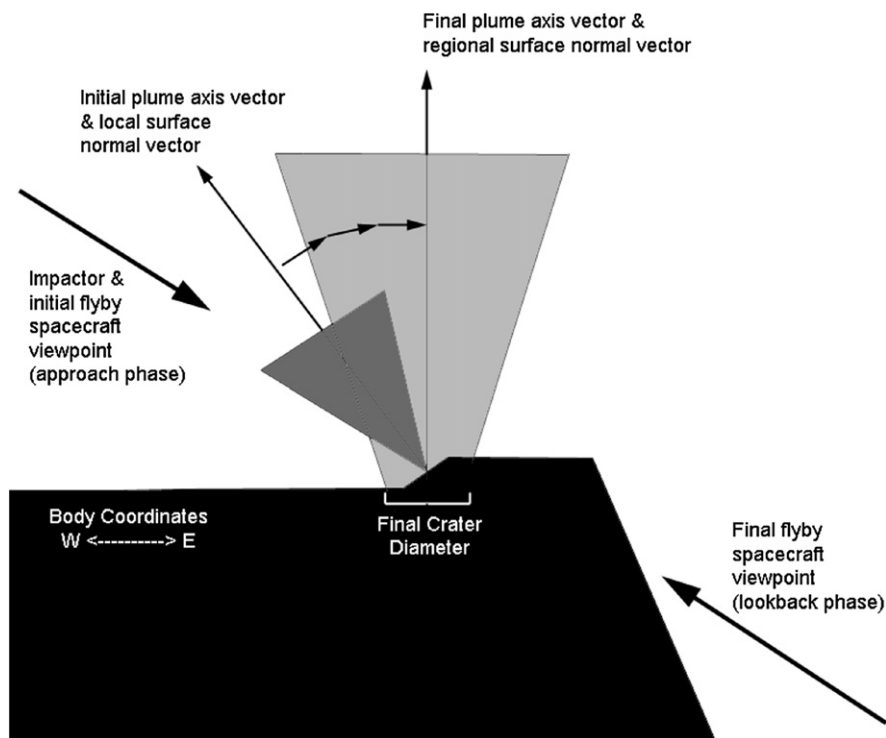


Fig. 15. Interpretation of the ejecta plume geometry presented by the HRI and MRI image sequences, in which the impact apparently occurred on a westward-facing slope roughly  $1/3$ – $1/2$  the size of the final crater produced. This irregular topography affected the reflection of the impact shock-wave off the target's free surface, which in turn altered the ejecta flow-field established. Although this was actually a spatial alteration in the flow-field, which occurred while all of the topography was still intact, we witnessed it as a temporal event, due to the diverse power-law distribution of ejecta particle velocities. Thus, we saw the affect on the fastest-speed particles first, and then "sampled" increasingly slower particle populations as the plume evolved over time.

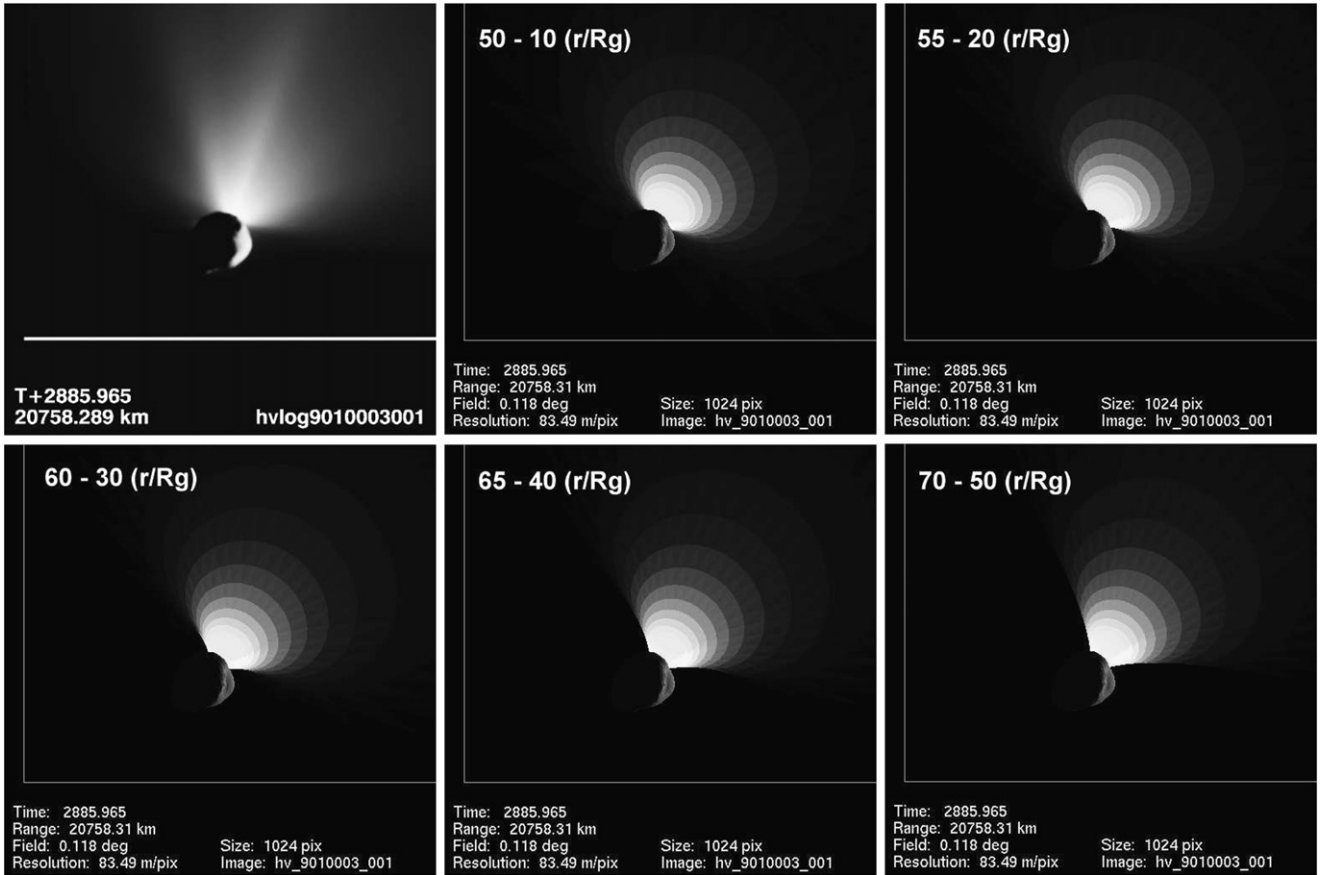


Fig. 16. A series of model simulations used to fit the ejecta plume side angles shown in image HV9010003.001, by varying the parameters of  $\psi_n$  (Eq. (44)) in such as way as to keep the mean ejection angle at  $\bar{\psi} \approx 45^\circ$ . Although the boundaries of the actual ejecta plume are somewhat diffuse, a reasonable fit is achieved at starting angles of  $\psi_o = 60^\circ \pm 5^\circ$  and a total angular drop of  $\psi_d = 30^\circ \pm 10^\circ$ .

angles  $\psi$ . As mentioned earlier, the HRI image of the newly emerging plume (Fig. 13) is best modeled by an ejecta cone opening angle which is consistent with experimentally produced ejecta plumes (Cintala et al., 1999; Anderson et al., 2003, 2004). To further constrain this, we took advantage of the near-profile view of the ejecta plume afforded by the first look-back images (phase 4). As shown in Fig. 16, repeated model iterations indicated that the most straight-forward way to fit the ejecta plume side positions was achieved by varying the parameters of  $\psi_n$  (Eq. (44)) in such as way as to keep the mean ejection angle at  $\bar{\psi} \approx 45^\circ$ . Although the boundaries of the actual ejecta plume are somewhat diffuse, a reasonable fit is achieved at starting angles of  $\psi_o = 60^\circ \pm 5^\circ$  and total angular drops of  $\psi_d = 30^\circ \pm 10^\circ$ . There are two reasons for keeping the mean ejection angle at  $\bar{\psi} \approx 45^\circ$ : first, it keeps our model consistent with experimental findings, in which  $\bar{\psi}$  is generally within the range of  $40^\circ$ – $45^\circ$  (Section 2.4); and second, it keeps our model consistent with our ejecta velocity constant derivation assumptions (Section 2.2) and those of the original Maxwell Z-model (Maxwell and Seifert, 1974; Maxwell, 1977). It should be noted, however, that our solution is non-unique, and we have therefore selected the solution which is most consistent with past experiments and our current model derivation.

#### 4.2. Tempel 1 gravity and bulk density

With the ejecta plume axis orientation  $\chi$  and particle ejection angles  $\psi$  reasonably constrained, the next phase of the analysis was to determine the magnitude of the gravity field in which these particles were ballistically traveling (a function of the comet's bulk density). During the excavation and fallout phases of an impact event, the ejecta plume forms an inverted, hollow cone, and marks the position locus of the solid ejecta particles in flight at that time (Fig. 11): its bottom region is composed of particles nearing the end of their flight and falling out of the plume; its middle region is composed of particles midway through their ballistic flight and traveling nearly radial to the ejecta cone's axis; and its upper region is composed of particles which have not yet reached the apex of their ballistic flights, with the uppermost particles traveling faster than the escape velocity of the comet and therefore never returning to the surface. Because each ejecta particle is following its own ballistic trajectory under the influence of Tempel 1's gravity field, the lateral expansion rate of the *collective* ejecta plume is also a function of the comet's gravity field (Melosh, 2001).

To measure the lateral expansion rate of the ejecta plume produced by Deep Impact, we use the plume's base as our common point of reference and monitor the plume base diameter as a function of time. Fig. 17 shows several model examples

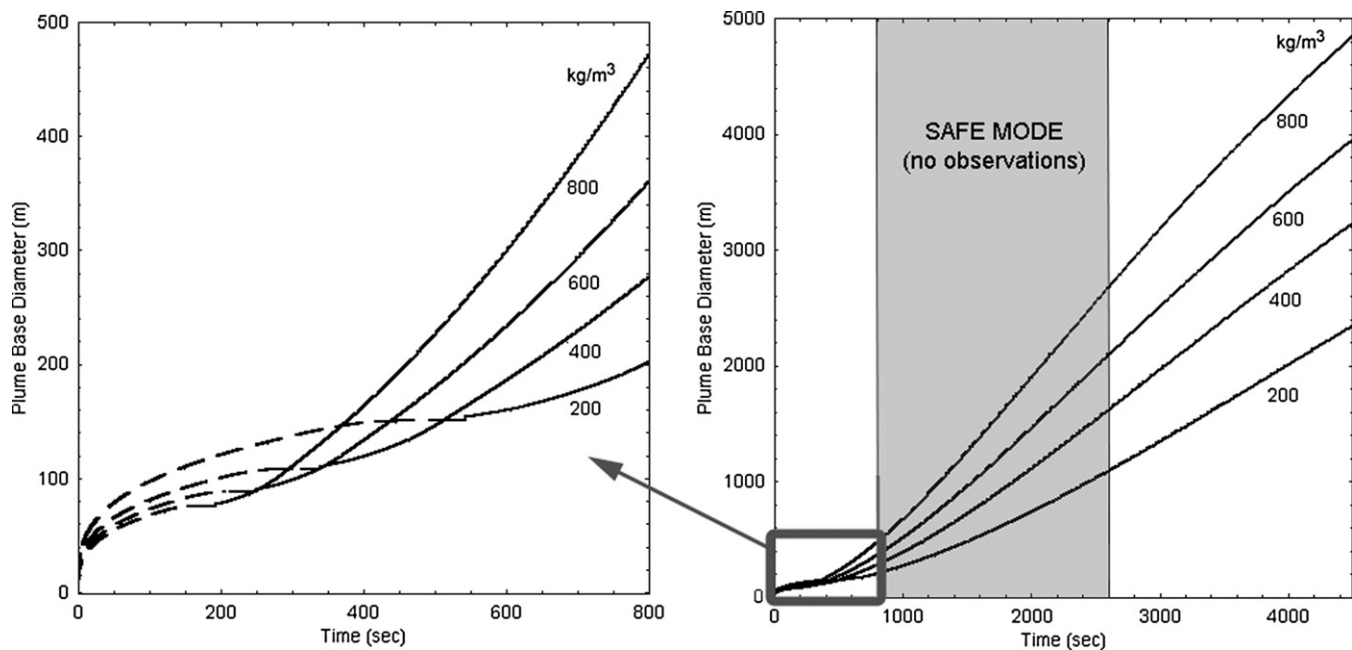


Fig. 17. Expansion of a modeled Deep Impact ejecta plume on the surface of a simple, spherical comet of radius 3.0 km. Each curve marks the diameter of the plume base as it marches along the ground, during both its ejection (*dashed line*) and fallout (*solid line*) phases, for the labeled comet bulk density  $\rho_t$ . At the beginning of crater growth, the plume expands quickly, but this expansion rate slows rapidly as slower moving material is added to the plume while the transient crater rim is approached. Once the crater has formed, the slowest moving particles fall out first, causing the plume to expand at an increasing rate as time passes, until only those particles ejected at the highest speeds remain. The Deep Impact mission comprised two viewing windows for potentially making plume base diameter measurements: from 0 to 800 s after impact during approach, and from about 45 to 75 min after impact during look-back.

of the expansion of an ejecta plume base produced by a Deep Impact-like event on a simple, spherical Tempel 1 shape-model, shown for a variety of different comet bulk densities  $\rho_t$  (and thus different gravity field environments). These curves follow the trailing edge of the ejecta plume, whose base is easier to mark during initial crater growth, and which will lag behind the leading edge of the ejecta plume by only about 20–40 m for a gravity-dominated Deep Impact-like event. At the beginning of crater growth, the plume expands very quickly, but this expansion rate slows as slower moving material is launched into the plume while the transient crater rim diameter  $D$  is approached. Once the crater has formed, the slowest moving particles are the first to fall out, which causes the plume to expand at an increasing rate over time, until only those particles ejected at the highest speeds remain. As depicted in Fig. 17, the Deep Impact mission contained two windows for potentially measuring the plume base diameter: from 0 to 800 s after impact during the approach phase of imaging, and from about 45 to 75 min after impact during the look-back phase of imaging.

As has been previously mentioned, our view of the impact crater and ejecta plume base were heavily obscured during the interior views of the plume obtained about 9 to 13 min after the impact, such that only a vague, dark oval marks the plume base and crater site (Figs. 1, 14, and 22). This plume base is of order 150–350 m in diameter, consistent with the plots shown in Fig. 17 (left panel), but is only able to constrain the comet's bulk density to something of order  $\rho_t = 100\text{--}1000 \text{ kg m}^{-3}$ , if this interpretation of the dark oval is correct. However, the mission was fortuitous in that the impact site produced an ejecta plume whose exterior was observable in near-profile view through-

out the look-back phase of imaging, affording us an excellent means for measuring its expansion rate, as shown in the right panel of Fig. 17.

Fig. 18 (left panel) shows the measured ejecta plume base diameter as a function of time, made by marking the diameter of the ejecta plume's base against the limb of the comet (as close to the actual base as possible), and indicated by the filled-triangles (with  $2\sigma$  error bars attached). Also shown are the measurements made from five sets of synthetic images produced by our model, where each set represents a different comet-model bulk density  $\rho_t$  and associated gravity field. The expansion of the model plumes were measured in the same fashion as the actual images, and are indicated by open-triangles. Because of the diffuse appearance of the actual ejecta plume's leading edge, an Unsharp Mask filter was used to sharpen the edges of the plume in each image, both actual and synthetic (examples are shown in Fig. 18, right panel). These measurements yield a mean surface gravity for Tempel 1 of  $\bar{g} = 0.34 \text{ mm s}^{-2}$  ( $0.17\text{--}0.50 \text{ mm s}^{-2}$ ), which corresponds to a comet mass of  $m_t = 4.5 \times 10^{13} \text{ kg}$  ( $2.3\text{--}6.8 \times 10^{13} \text{ kg}$ ) and a bulk density of  $\rho_t = 400 \text{ kg m}^{-3}$  ( $200\text{--}600 \text{ kg m}^{-3}$ ). This bulk density for Comet 9P/Tempel 1 compares favorably with previously determined comet bulk densities using other techniques, such as  $490 \text{ kg m}^{-3}$  ( $290\text{--}830 \text{ kg m}^{-3}$ ) for Comet 19P/Borrelly (Farnham and Cochran, 2002);  $180\text{--}300 \text{ kg m}^{-3}$  for Comet 19P/Borrelly (Davidsson and Gutiérrez, 2004);  $600\text{--}800 \text{ kg m}^{-3}$  for Comet 81P/Wild 2 (Davidsson and Gutiérrez, 2006);  $450 \pm 250 \text{ kg m}^{-3}$  for Comet 9P/Tempel 1 (Davidsson et al., 2007); and  $\sim 370 \text{ kg m}^{-3}$  for Comet 67P/Churyumov–Gerasimenko (Lamy et al., 2007), to name a few recent examples.



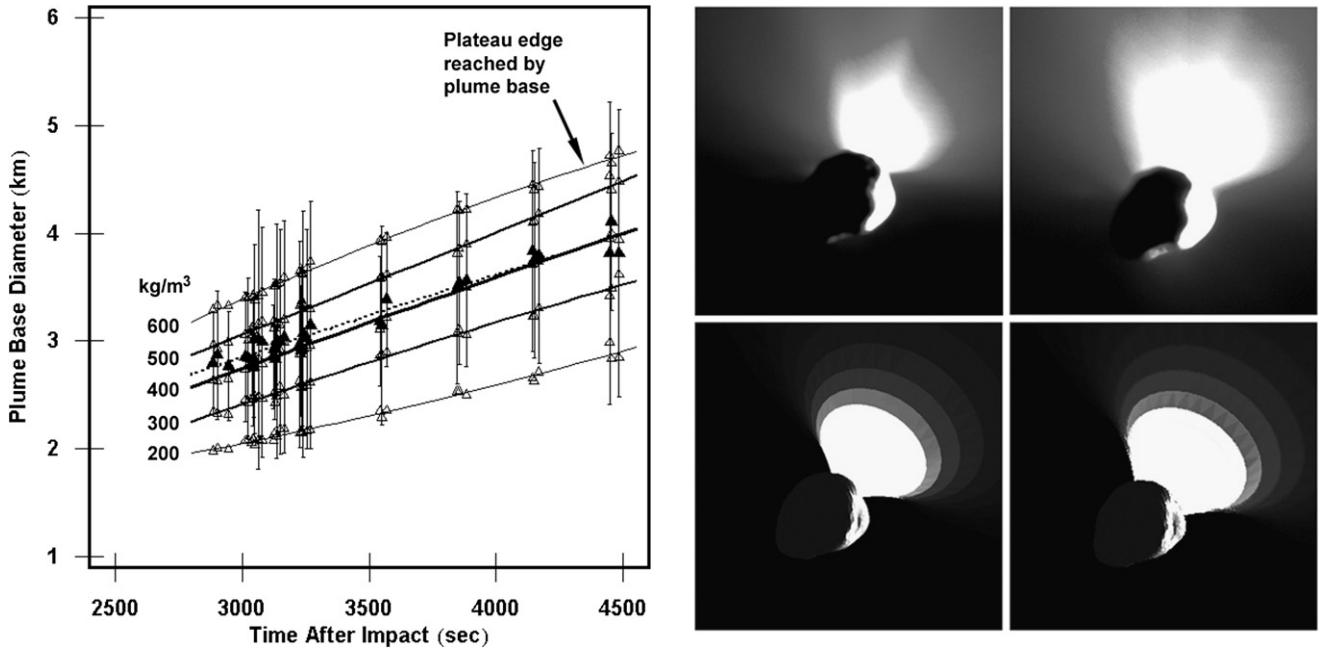


Fig. 18. (Left) Expansion of the actual Deep Impact ejecta plume, measured by marking the diameter of the plume base against the limb of the comet during the look-back phase of imaging. Filled black triangles are measurements from the actual images (HV9010003.001–HV9010052.001), shown with  $2\sigma$  error bars. Open triangles are measurements made from model-produced synthetic images, at five different comet-model bulk densities  $\rho_t$ . Each set of measurements is connecting using a least-squares polynomial fit, the dotted line for the actual image measurements and the solid lines for the synthetic image measurements, with a very good match occurring at a model bulk density of  $\rho_t = 400 \text{ kg m}^{-3}$  (200–600  $\text{kg m}^{-3}$ ). (Right) Four examples of the images used to create this plot, as shown in edge-sharpened, re-scaled actual images (upper) and synthetic model images (lower). The left-hand images are from the beginning of the look-back phase (45 min after impact), while the right-hand images are from the end of the look-back phase (75 min after impact).

Although the agreement of our results with these previous estimates is good, all of these estimates are based on the computation of non-gravitational forces for the various cometary nuclei, computations that involve many assumptions and are generally regarded as very uncertain (Weissman et al., 2004). Because all spacecraft encounters with comets to date, including Deep Impact, have been fast flybys at distances of many nuclear radii, it has not been possible to compute the mass directly from the deflection of the spacecraft. Other methods, such as modeling the unique tidal breakup of Comet SL/9, relations between the rotation period and shape of comet nuclei, and estimates from the density of cometary dust particles plus assumptions about how comets are assembled all yield similar, but also uncertain density estimates (Weissman et al., 2004). Our method of modeling ejecta plume expansion is different than previous methods, but it suffers similarly from many uncertainties, as explained in this paper. Before the Deep Impact encounter with Tempel 1 we had anticipated the ability to track discrete boulders ejected from the impact (Richardson et al., 2005). Indeed, the image sequence we adopted, particularly the look-back imaging, was planned with the expectation of being able to track ballistically ejected boulders and thus get good estimates of the gravitational acceleration near Tempel 1's nucleus. Modeling the ejecta plume expansion to determine gravity was regarded as a “last-ditch” option that we hoped we would not have to exercise, but we developed it in case all else failed. As events turned out, however, boulders were not detected in the ejecta plume, nor did we see coherent boulders on the surface of Tempel 1 at our highest resolution. While

this observation has important consequences for the geology of Tempel 1, it is an unfortunate circumstance for gravity determination. Nevertheless, our careful modeling of the ejecta plume has yielded useful constraints on the density of Tempel 1 that are completely independent of other methods of density determination.

There are four potential sources for error in this comet density estimate: image measurement errors (shown in Fig. 18), comet shape-model errors (Thomas et al., 2007), ejecta plume model errors (this work), and non-gravitational forces (Section 4.4). The rather diffuse plume edge appearance in the HRI look-back images meant that different amounts of edge sharpening change the apparent plume width slightly: creating up to a 50% fractional error in the density measurement ( $2\sigma$ ). The comet shape-model from Thomas et al. (2007), with a mean radius of  $3.0 \pm 0.1 \text{ km}$ , has a volume error of 10%, but in terms of the density (which goes as  $1/\text{radius}$ ) this produces a fractional error of only 3.3% in the density measurement. Model-plume width variations in the synthetic images, created by exercising our model parameters over their full ranges (Tables 2 and 4), produce up to a 10% fractional error in the density measurement. Combining all three quantified sources of error yields a total fractional error of 51% in the density measurement, such that the measurement errors from the HRI look-back images completely outweigh the other potential sources discussed here. The effects of non-gravitational forces on the ejecta plume expansion rate, however, are more difficult to quantify, with the potential effect of coma gas pressure being the most problematic. This will be discussed further in Section 4.4.

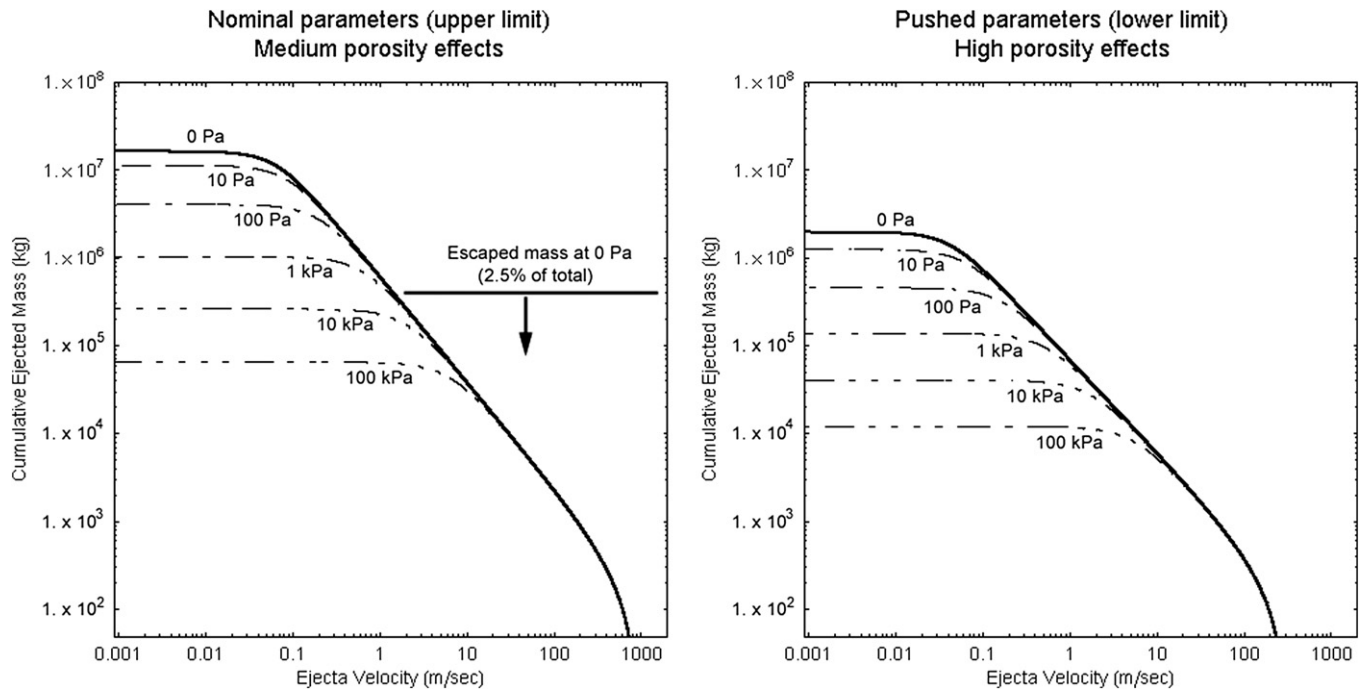


Fig. 19. Model-based plots of the cumulative mass of solid ejecta particles produced by Deep Impact, ejected at greater than a given velocity, for material constants consistent with medium porosity (*left*) and high porosity (*right*). The solid, bold curves represent gravity-dominated events ( $\bar{Y} = 0$  kPa), while the dot-dash curves represent increasing values of effective surface strength  $\bar{Y}$ . Comparison of these values with a variety of Earth-based measurements of the ejecta plume's total mass indicates an upper limit to the comet's surface strength at the impact site of order  $\bar{Y} = 1\text{--}100$  kPa, with the range of  $\bar{Y} = 1\text{--}10$  kPa being most likely.

Table 3  
Deep Impact excavated mass: from various sources

| Study                | Instrument | Wavelength         | Low mass (largest particle)             | High mass (largest particle)              |
|----------------------|------------|--------------------|---|---|
| Harker et al. (2005) | Gemini-N   | 8–13 $\mu\text{m}$ | $7.3 \times 10^4$ kg (1 $\mu\text{m}$ ) | $1.5 \times 10^6$ kg (100 $\mu\text{m}$ ) |
| Keller et al. (2005) | Rosetta    | $648 \pm 43$ nm    | –                                       | $7 \times 10^6$ kg (500 $\mu\text{m}$ )   |
| Lisse et al. (2006)  | Spitzer    | 5–35 $\mu\text{m}$ | $8 \times 10^5$ kg (10 $\mu\text{m}$ )  | $1.3 \times 10^6$ kg (1 m)                |
| Sugita et al. (2005) | Subaru     | 8–20 $\mu\text{m}$ | $5 \times 10^5$ kg (10 $\mu\text{m}$ )  | $7 \times 10^7$ kg (1 m)                  |

#### 4.3. Impact site surface strength

At this point we have values for two of our three desired unknowns; that is, estimates for the gravity field  $\bar{g}$  and target density  $\rho_t$  at the impact site (assuming that the comet's surface density is reasonably close to its bulk density). This modeling work also gives us two methods for estimating an upper limit to the effective strength  $\bar{Y}$  of the material at the impact site: both of which, unfortunately, include large sources of inaccuracy.

##### 4.3.1. Strength via excavated mass

The first method for estimating the effective strength  $\bar{Y}$  is relatively straight-forward: we can compare model estimates of the total excavated (ejected) mass, under varying conditions of strength, to measurements made of this same parameter from a variety of Earth-based and space-based instruments at the time of the Deep Impact event.

Fig. 19 shows a variety of estimates for the cumulative excavated mass from the Deep Impact cratering event using Eq. (49), plotted as a function of ejecta velocity (Eq. (41)) over the radius  $r$  range of  $d$  to  $R_s$  (again omitting the volume of potentially vaporized target material) in steps of  $dr =$

$(R_s - d)/10^4$ . In each case, the impact site surface density is assumed to be equal to the determined comet bulk density  $\rho_t$ . The curves on the left were produced using our nominal (medium porosity) parameter set, while the curves on the right were produced using our “pushed” (high-porosity) parameter set (Table 2). The zero-strength ( $\bar{Y} = 0$  Pa), gravity-dominated curve represents an upper limit to the ejected mass, with a value of  $M_g = 1.8 \times 10^7$  kg ( $1.5\text{--}2.2 \times 10^7$  kg). As the surface's effective strength  $\bar{Y}$  is increased, the crater volume decreases, and the ejected mass drops accordingly. This family of curves can then be compared to the total ejected masses determined from a variety of other Deep Impact studies, which are listed in Table 3.

At first glance, these values would seem to indicate a definite surface strength somewhere in the large range of  $\bar{Y} = 1\text{--}100$  kPa. However, it is important to keep in mind that most of the ejected mass in the plume is contained within its base and involves the slowest moving ejecta, such that these studies may not have seen the full extent of mass excavated. Additionally, the time at which these measurements were made also plays an important role. For a gravity-dominated Deep Impact event, the percentage of ejected mass  $M_g$  landed at time  $t$  after the impact

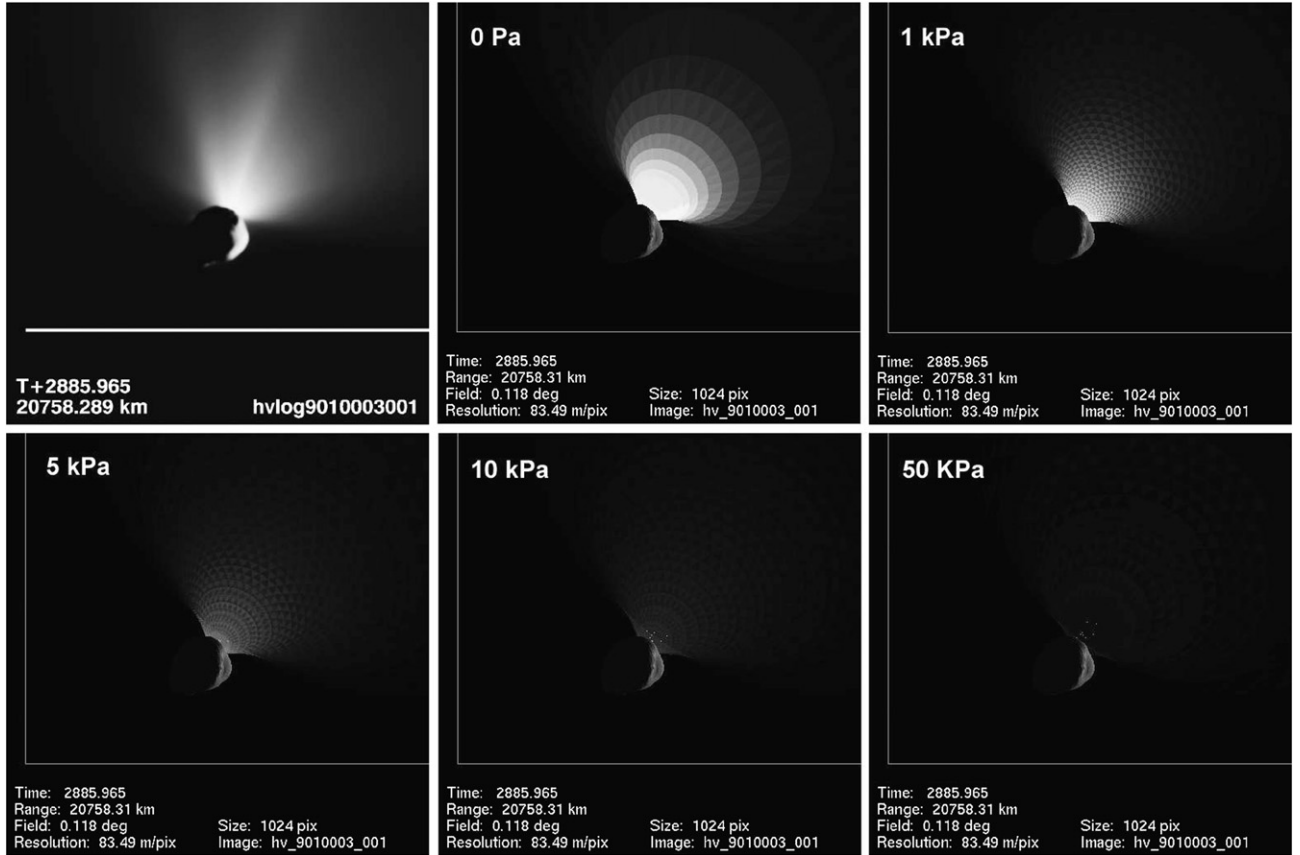


Fig. 20. A series of model simulations used to fit the ejecta plume brightness (opacity) shown in image HV9010003.001, by varying the effective target strength  $\bar{Y}$  and assuming a Spitzer-based particle distribution (Lisse et al., 2006). This exercise indicates an upper limit to the comet’s surface strength at the impact site of order  $\bar{Y} = 1\text{--}10$  kPa, with the range of  $\bar{Y} = 1\text{--}5$  kPa being most likely. Although the best “visual” fit may appear somewhat lower, our plume opacity model is still rather simplistic, with a larger potential error than this figure indicates. Note that the plume base width remains the same regardless of target strength, demonstrating the robustness of our density estimate even in the presence of some target strength.

will roughly be (with landed particle ejection velocities given in parenthesis):

- $t = 9$  min ( $<0.1$  m s $^{-1}$ ): 50%  $M_g$  landed,
- $t = 15$  min ( $<0.2$  m s $^{-1}$ ): 75%  $M_g$  landed,
- $t = 45$  min ( $<0.5$  m s $^{-1}$ ): 91%  $M_g$  landed,
- $t = 1$  h ( $<0.6$  m s $^{-1}$ ): 93%  $M_g$  landed,
- $t = 4$  h ( $<1.0$  m s $^{-1}$ ): 96%  $M_g$  landed,
- $t = 1$  day ( $<1.28$  m s $^{-1}$ ): 97.1%  $M_g$  landed,
- $t = 2$  day ( $<1.33$  m s $^{-1}$ ): 97.3%  $M_g$  landed,

such that  $>90\%$  of the ejected mass never gets more than a few hundred meters off the surface of the comet, and has been redeposited within 45 min after the impact. Thus, the ejected masses determined via remote sensing may be up to an order of magnitude too low, *if* this was a gravity-dominated cratering event. In a strength-dominated event, much of this low-speed ejecta is never ejected in the first place, and the problem is not as severe. Therefore, this method for estimating the comet’s surface strength yields only an *upper limit* of  $\bar{Y} = 1\text{--}100$  kPa, with  $\bar{Y} = 1\text{--}10$  kPa being most likely, such that a gravity-dominated event cannot be ruled out.

Fig. 19 also indicates that the highest speed ejecta particles (shown in the lower right end of these curves) should have been

moving at speeds of hundreds of meters per second. This is consistent with the findings via remote sensing, which measured speeds for the leading edge of the ejecta plume (as seen from their perspective) of  $\sim 190$  m s $^{-1}$  (Mason et al., 2007);  $\sim 200$  m s $^{-1}$  (Milani et al., 2007);  $197 \pm 16$  m s $^{-1}$  (Bauer et al., 2007);  $200\text{--}230$  m s $^{-1}$  (Knight et al., 2007);  $<230$  m s $^{-1}$  (Schleicher et al., 2006);  $\sim 200$  m s $^{-1}$  (Keller et al., 2007); and  $230\text{--}250$  m s $^{-1}$  (Lisse et al., 2006), to name a few of these observations. As Fig. 19 indicates, however, these speeds only represent the “tip of the iceberg,” such that the majority of particles in the plume were ejected at speeds of one to three orders of magnitude *below* these values. Even in a more energy-efficient, gravity-dominated cratering event, our modeling indicates that  $<5\%$  of the impactor–spacecraft’s kinetic energy would have been transferred to the solid particles in the ejecta plume.

#### 4.3.2. Strength via ejecta plume opacity

The second method for estimating an upper limit to the strength of the material at the impact site is to model the effect of surface strength on the ejecta plume’s brightness. As Fig. 11 shows, the mass-loading (thickness) of the ejecta plume will be a function of the transient crater volume, which is, in turn, a function of the effective surface strength  $\bar{Y}$ . Therefore,

Table 4  
Model determined parameters

| Name  | Symbol      | Nominal value           | Value range                          |
|---|-------------|-------------------------|--------------------------------------|
| Initial plume axis N–S tilt                 | $\chi_{no}$ | 0°                      | ±5°                                  |
| Initial plume axis W–E tilt                 | $\chi_{wo}$ | 45°                     | ±5°                                  |
| Final plume axis N–S tilt                   | $\chi_{nf}$ | 0°                      | ±5°                                  |
| Final plume axis W–E tilt                   | $\chi_{wf}$ | 5°                      | ±5°                                  |
| Initial particle ejection angle             | $\psi_o$    | 60°                     | ±5°                                  |
| Particle ejection angle drop                | $\psi_d$    | 30°                     | ±10°                                 |
| Impact site surface strength                | $\bar{Y}$   | 0–5 kPa                 | 0–10 kPa                             |
| Tempel 1 mean gravity                       | $\bar{g}$   | 0.34 mm s <sup>-2</sup> | 0.17–0.90 mm s <sup>-2</sup>         |
| Tempel 1 bulk density                       | $\rho_t$    | 400 kg m <sup>-3</sup>  | 200–1000 kg m <sup>-3</sup>          |
| Tempel 1 mass                               | $m_t$       | $4.5 \times 10^{13}$ kg | $2.3\text{--}12.0 \times 10^{13}$ kg |
| Crater diameter ( $\bar{Y} = 0$ Pa)         | $D_g$       | 100 m                   | 85–140 m                             |
| Crater formation time ( $\bar{Y} = 0$ Pa)   | $T_g$       | 330 s                   | 250–550 s                            |
| Crater excavated mass ( $\bar{Y} = 0$ Pa)   | $M_g$       | $1.8 \times 10^7$ kg    | $1.5\text{--}2.2 \times 10^7$ kg     |
| Crater diameter ( $\bar{Y} = 1$ kPa)        | $D_s$       | 37 m                    | 35–41 m                              |
| Crater formation time ( $\bar{Y} = 1$ kPa)  | $T_s$       | 11 s                    | 8–12 s                               |
| Crater excavated mass ( $\bar{Y} = 1$ kPa)  | $M_s$       | $0.91 \times 10^6$ kg   | $0.60\text{--}1.2 \times 10^6$ kg    |
| Crater diameter ( $\bar{Y} = 10$ kPa)       | $D_s$       | 24 m                    | 22–26 m                              |
| Crater formation time ( $\bar{Y} = 10$ kPa) | $T_s$       | 2 s                     | 1–3 s                                |
| Crater excavated mass ( $\bar{Y} = 10$ kPa) | $M_s$       | $2.3 \times 10^5$ kg    | $1.5\text{--}2.9 \times 10^5$ kg     |

we can use the opacity of the ejecta plume (Eq. (56)) as a means to gauge its mass-loading, provided that we have an independent means for determining the ejecta particle size distribution (PSD).

Fig. 20 shows a comparison between the first look-back image obtained by the HRI instrument and several model runs of varying effective surface strength  $\bar{Y}$ . Each of these synthetic images uses the particle size distribution (PSD) determined via the space-based Spitzer telescope (Lisse et al., 2006), which uses an ejecta particle size range of 0.1 to at least 20  $\mu\text{m}$ , with a peak at 1.0  $\mu\text{m}$ . We have also assumed an individual particle density of  $\rho_p = 1750 \text{ kg m}^{-3}$ : a 50% mixture of ice and silicate dust (Sunshine et al., 2007). These synthetic image comparisons place an *upper limit* on the comet's surface strength at the impact site of  $\bar{Y} = 1\text{--}10$  kPa, with the range of  $\bar{Y} = 1\text{--}5$  kPa being most likely; where again, a gravity-dominated event cannot be ruled out. This strength determination is consistent with the estimate from the cumulative excavated mass model (Section 4.3.1), and the strength determined by Holsapple and Housen (2007). Note that although the best “visual” fit occurs in the top images of Fig. 20, for  $\bar{Y}$  values of up to 1 kPa, our current ejecta plume opacity model is somewhat simplistic (Section 3.2), and the potential error remains large at this point.

#### 4.4. The effects of non-gravitational forces

Up to this point, the ejecta ballistics model has contained only the acceleration due to gravity  $g$  as an external force act-

ing on the ejecta particles once they are launched. However, because Deep Impact occurred on a cometary nucleus, and produced an ejecta plume composed of very fine particles, there are five potential sources for additional forces on the ejecta particles in flight which need to be considered, especially with regard to their potential effect on the Tempel 1 gravity and bulk density estimate (Section 4.2). Two of these potential sources, solar radiation pressure and coma gas pressure, are inherent to the cometary environment in which the impact took place. The remaining three potential sources were produced by the impact event itself: the initial vapor plume, water-gas sublimation from icy grains within the ejecta plume, and impact-induced cometary activity following the cratering event.

##### 4.4.1. Solar radiation pressure

Solar radiation pressure will show its effect as an acceleration in the anti-solar direction, affecting all insolated ejecta particles proportional to their (surface area)  $\times$  (photon absorption-scattering efficiency)/(mass) product. The most pronounced effect will be on small particles with sizes 0.1–1.0  $\mu\text{m}$ , which have very little mass but possess high scattering efficiency due to a similar size to the wavelengths of visual light. The relative effect of solar radiation pressure is usually expressed in comparison to the force of solar gravity at the comet's location:  $\beta = F_{\text{Radiation pressure}}/F_{\text{Solar gravity}}$ . Beta is also related to the surface/volume ratio of a dust particle, since the radiation pressure force depends on the surface area of the particle absorbing sunlight, while the gravitational force depends on the particle's volume. Typical values of Beta are  $\sim 1$  for particles of 0.5–1.5  $\mu\text{m}$  in radius, falling off inversely with radius for larger particles, and typical time scales for the importance of this effect in cometary dust comae and tails at 1 AU is on the order of days to weeks (Lisse et al., 1998). Since the measured Deep Impact ejecta size distribution consisted of a majority of particles of this size (Lisse et al., 2006), we expect this to be an important force, but since the timescale over which the observations were made was short, 1/50th to 1/500th the typical amount of time, the overall effect may not be very large.

In examining the Deep Impact HRI images, we do find indications of a small, anti-solar drift in the ejecta plume base by the time of the first look-back images, when compared to model-produced synthetic images (Figs. 18 and 20). This drift is not more than about 400–800 m, which corresponds to an acceleration of 0.1–0.2 mm s<sup>-2</sup> in the anti-solar direction. Note however, that this motion appears to involve *all* particles in the ejecta plume, such that the entire plume is slightly displaced, and thus the ejecta cone's expansion rate (used in the gravity estimate) is not affected. Additional model iterations were performed which included this apparent acceleration (Section 3.3), and although there are small measurement changes due to the model plume being located behind a slightly different portion of the comet's limb, these changes do not effect the overall expansion rate or best-fit gravity/density solution.

The observed small drift in ejecta plume position can, however, be used to estimate the mean particle size in the ejecta plume at the time of the look-back observations. At the distance of Tempel 1 from the sun at the time of encounter, an anti-solar



acceleration of  $0.1\text{--}0.2\text{ mm s}^{-2}$  corresponds to a mean particle size of order  $6\text{--}12\text{ }\mu\text{m}$ , for particles in the base of the ejecta cone at the time of these observations. This is about a factor of 3 larger than the particle sizes derived from the Spitzer observations, which found a mean particle size of  $0.1\text{--}2\text{ }\mu\text{m}$  for the higher speed particles ejected earlier in the excavation process (Lisse et al., 2006), but is not grossly out of line, and is consistent with the suite of ejecta particle sizes estimated via long-range remote sensing (Table 3).

#### 4.4.2. Coma gas pressure

The force on a lofted dust particle due to comet out-gassing is directed outward from the surface of the comet and will therefore act in roughly the anti-gravity direction. This implies that in our gravity determination, we did not measure the acceleration due to gravity  $g$  alone, but rather  $(f_c - g)$ , where  $f_c$  is the outward directed acceleration on the ejecta particles due to coma gas drag, and  $|g| > |f_c|$  by the amount that we determined in Section 4.2. Thus, the question arises: how significant is this force to the observed evolution of the Deep Impact ejecta plume?

Under normal circumstances, dust is entrained by the sublimation of cometary volatile ices: this is what propels dusty material on the surface into the coma. Finson and Probst (1968) modeled the flow of cometary dust assuming simple hydrodynamic flow. This approximation works well for a low activity comet such as Tempel 1, with an out-gassing rate of  $\sim 10^{28}\text{ mol s}^{-1}$ . The net effect is to accelerate dust at rest on the surface up to speeds of  $v = 300\text{ m s}^{-1} \sqrt{\beta/r_h}$ , where  $r_h$  is the heliocentric distance of the comet in AU. For a  $0.5\text{ }\mu\text{m}$  radius particle, with  $\beta \approx 1.0$ , this implies a terminal velocity for the particle of  $\sim 200\text{ m s}^{-1}$ , reached within the gas-dust decoupling distance of  $r_d \approx 100\text{ km}$  from the comet. Using  $v^2 = v_o^2 + 2f_c r_d$ , a decoupling radius of  $r_d = 100\text{ km}$ , and an initial velocity of zero for dust at rest on the surface, this implies a net acceleration due to gas drag of  $\sim 0.2\text{ m s}^{-2}$ , operating over a time period of  $\sim 1000\text{ s}$ . This estimated magnitude for the coma gas-induced acceleration is roughly 3 orders of magnitude more important than the acceleration due to radiation pressure. For a particle 100 times larger, about  $100\text{ }\mu\text{m}$  in radius with  $\beta \sim 0.01$ , the terminal velocity will be 10 times lower,  $\sim 20\text{ m s}^{-1}$ , and the acceleration a factor of 100 less: so this effect is very strongly size dependent, going linearly in the parameter  $\beta$ . The largest particle detected during a comet flyby,  $\sim 1\text{ cm}$  in the coma of Comet Halley, would have a  $\beta$  value  $\sim 10^{-4}$ , and thus a coma terminal velocity of  $\sim 2\text{ m s}^{-1}$ , similar in magnitude to the escape velocity for a cometary body.

It is important to recognize, however, that in the vicinity of the ejecta plume where the gravity measurements were made, the dust density will have been quite high (compared to where it normally is, sans impact event), so that mass-loading on the outward flowing gas, from the surface of the comet in the vicinity of the impact site, will also have been quite high, and the affect of coma gas drag on individual ejecta particles significantly mitigated. For example, if we assume that under normal circumstances, coma gas outflow is able to accelerate a comet-dust output flux of  $200\text{ kg s}^{-1}$  per  $2\pi$  steradians to terminal velocity

(defined above), and that the Deep Impact event rapidly injected  $\sim 1.0 \times 10^7\text{ kg}$  of dust into a  $0.24\pi$  steradian area (a  $3\text{ km}$  diameter area at the comet's surface), then coma gas accelerations on the ejecta particles of order  $f_c = 0.04\text{--}0.4\text{ mm s}^{-2}$  can be roughly estimated. The upper limit in this estimate corresponds to particles of  $1\text{ }\mu\text{m}$  in size, the peak of the Spitzer particle distribution (Lisse et al., 2006), and as such, coma gas pressure may have had a significant effect on our gravity determination. As stated previously, our gravity measurement is, in effect, measuring the difference force  $(f_c - g)$  and not just  $g$  alone, such that the actual gravity is potentially higher than what we measured by up to a factor of about two. We must therefore extend the error range of our measured values to include this uncertainty, to obtain:  $\bar{g} = 0.34\text{ mm s}^{-2}$  ( $0.17\text{--}0.90\text{ mm s}^{-2}$ ), which corresponds to a comet mass of  $m_t = 4.5 \times 10^{13}\text{ kg}$  ( $2.3\text{--}12.0 \times 10^{13}\text{ kg}$ ) and a bulk density of  $\rho_t = 400\text{ kg m}^{-3}$  ( $200\text{--}1000\text{ kg m}^{-3}$ ). Further investigation and more sophisticated modeling beyond the scope of this work will be required to constrain the magnitude of this force further, and re-tighten the potential error in our Tempel 1 gravity/mass/density determination.

#### 4.4.3. Impact vapor plume

As discussed in Section 1.1, the excavation stage begins with the expulsion of a high-speed, rapidly expanding bubble of vapor and entrained melt droplets, which is then followed by the high-speed portion of the solid-particle excavation flow. Interaction between these two components of the excavation stage should be considered, although such interaction is unlikely because the main body of the vapor plume moves away from the impact site at speeds of roughly an order of magnitude higher than the fastest moving solid ejecta particles (Melosh et al., 2006). Any remaining energetic gas trailing the main body of this bubble would tend to push radially outward on the fastest moving solid material, such that particle velocities on the high-speed edge of the ejecta plume (the “leading edge” as seen from Earth) may have been affected by this rapid gas evolution. However, the high-speed portion of the ejecta plume represents only a tiny fraction of the total ejected mass (Fig. 19), such that this potential effect is deemed not relevant to either the remaining evolution of the ejecta plume, which involved much slower moving particles that remained close to the comet's surface, or our determination of the comet's gravity.

#### 4.4.4. Ice particle sublimation

The overall amount of water-gas created by the impact event, as measured by the in-flight ROSETTA spacecraft, is  $\sim 6 \times 10^5\text{ kg}$ : equivalent to about 10 h of normal coma out-gassing (Küppers et al., 2005). However, much of this must have been released in the form of solid, water-ice, as the total amount of energy delivered by the impactor,  $\sim 19\text{ GJ}$ , is much less than that required to vaporize this much water (Keller et al., 2005). Other observations confirm that the solid-particle ejecta plume in the approach and look-back images contained a large fraction of solid ice particles mixed in with the dust (Küppers et al., 2005; Sunshine et al., 2007; Fernández et al., 2007). Once ejected from the comet, this ice

would have started to sublime, potentially applying additional accelerations to the attached dust particles.

In general, when we look at the icy fragments that break off comets under other circumstances, as were seen for Comet 73P/SW3 in 2006 or Comet C/Hyakutake 1996B2 in 1996 (fragments of order 50–200 m in radius), we see what appears to be a strong directed jet force, presumably due to sublimation, directed towards the sunward side of the body. The cause of this is direct heating of the fragment surface by incident sunlight, coupled with the very low thermal inertia of the cometary fragment material (Lisse et al., 2005; Groussin et al., 2007), so that the out-gassing occurs at local noon on the fragment, and the body is accelerated by jet reaction forces in the anti-solar direction. However, no large fragments were detected in the Deep Impact ejecta; the vast majority of material was of much smaller size, 0.1–10  $\mu\text{m}$  in radius (Lisse et al., 2006). These particles, despite having a low thermal inertia, cannot support a significant thermal gradient across their radius, and are also tumbling very rapidly if they are in virial equilibrium with the out-flowing gas. We would thus expect these particles to have little, if any, directed motion due to ice sublimation. What common acceleration there may have been should have occurred in the anti-solar direction, and would thus have combined itself with our estimates of the solar radiation pressure (Section 4.4.1).

As noted above, abundant solid-water ice was clearly detected as part of the impact ejecta plume by the flyby-spacecraft during both the approach and look-back phases of imaging (Sunshine et al., 2007), a detection also confirmed by the Spitzer telescope (Lisse et al., 2006). Water-gas was also detected in the ejecta plume at this time, and it is reasonable to assume that this gas would have sublimed from the icy grains after they were lifted into the coma and exposed to sunlight. Because these icy grains were ballistically launched, they (and the gas derived from them) would have had a center-of-mass motion similar to that of the long-lived grains within the ejecta plume, resulting in two ice-grain populations which could potentially affect our gravity determination: ice grains ejected early enough in the excavation process to form part of the sides of the ejecta plume at the time of the look-back images, and ice grains ejected late in the excavation process and which formed part of the landed, ejecta blanket at the time of the look-back images.

Regarding ice sublimation from grains still in flight as part of the ejecta plume, since there is nothing to direct these forces on the tumbling and rotating particles, we envision these as randomly directed forces, accelerating some particles radially outward, some radially inward, some axially upward, some axially downward, and some tangentially. The overall effect would be a gradual diffusion of the ejecta plume from an initially thin shell about 20–40 m in thickness to a Gaussian distribution of particles on the order of a couple hundred meters in thickness. This “fuzzing” of the plume is thought to be a primary source for the image-measurement error in our gravity determination, making the actual outer edges of the ejecta plume somewhat diffuse and difficult to define, as discussed in Section 4.2. Thus, this water ice sublimation did affect this measurement by giv-

ing us a larger fractional measurement error; however, the *peak* of the Gaussian distribution would have continued to follow the shell’s original trajectory, and would therefore not have systematically altered the gravity measurement.

Solid ice inclusion within the most massive and lowest speed portions of the ejecta plume presents a different situation, since this ejecta will have landed to form part of the ejecta blanket around the transient crater rim. On the one hand, the time-scale for this redeposition is on the order of several minutes: recall from Section 4.3.1 that 50% of the excavated mass from a gravity-dominated cratering event will have landed within about 9 min of the time of impact. On the other hand, the time-scale for sublimation of this ice is comparable to the time over which we conducted observations via the flyby-spacecraft (75 min). Thus, the primary effect of the water-gas liberated from the ejecta blanket around the newly-formed crater would be a hemispherical expansion force emanating from the impact area that would tend to drive solid ejecta particles still in flight upwards and radially outward—with this force following a typical inverse square law reduction with distance.

If we consider these two components of acceleration, the upward acceleration on any grain should, as it travels ballistically, lead to us underestimating gravity because the grain falls back later than it otherwise should. The radial acceleration leads to the grain falling back at roughly the “right” time, but further from the crater, and this would cause us overestimate the gravity. Due to the inverted-cone geometry of the ejecta plume, the radial component of this outward gas pressure would have the more severe effect on the measured plume expansion rate, such that we are more likely to have potentially overestimated the gravity due to this force. This effect is, however, thought to be quite minor because most of the ejecta blanket would have been concentrated within about 1–4 crater radii of the impact site (Fig. 12), that is, within about 50–200 m, while the ejecta plume at the time of the first look-back images was more than a kilometer in radius and growing (Fig. 18). Additionally, once the icy ejecta particles had landed again to form part of the ejecta blanket, many of these particles would have been buried and no longer in direct sunlight, reducing their sublimation rate. Nonetheless, further investigation of this effect is warranted in future studies.

#### 4.4.5. Impact-induced cometary activity

Despite many early misinterpretations of the appearance of the impact ejecta plume in the look-back images, there is no indication of an on-going outflow of material having occurred as a result of our impact on Comet Tempel 1. All of the dust observed can be reasonably assumed to have been launched ballistically in an impulsive event, and the measured plume masses are consistent with this (Section 4.3.1). The comet itself had definitely returned to normal gas/dust levels within about 24 h (and most certainly within 48 h); Keller et al. (2005); Küppers et al. (2005); Lisse et al. (2006); Schleicher et al. (2006). This is also consistent with the clearing timescale for ballistically launched ejecta particles, in that  $86,400 \text{ s day}^{-1} \times 1 \text{ m s}^{-1}$  particle velocity = 87 km, so that it would have taken about 1–2 days for the slowest escaping ejecta to leave the collisionally

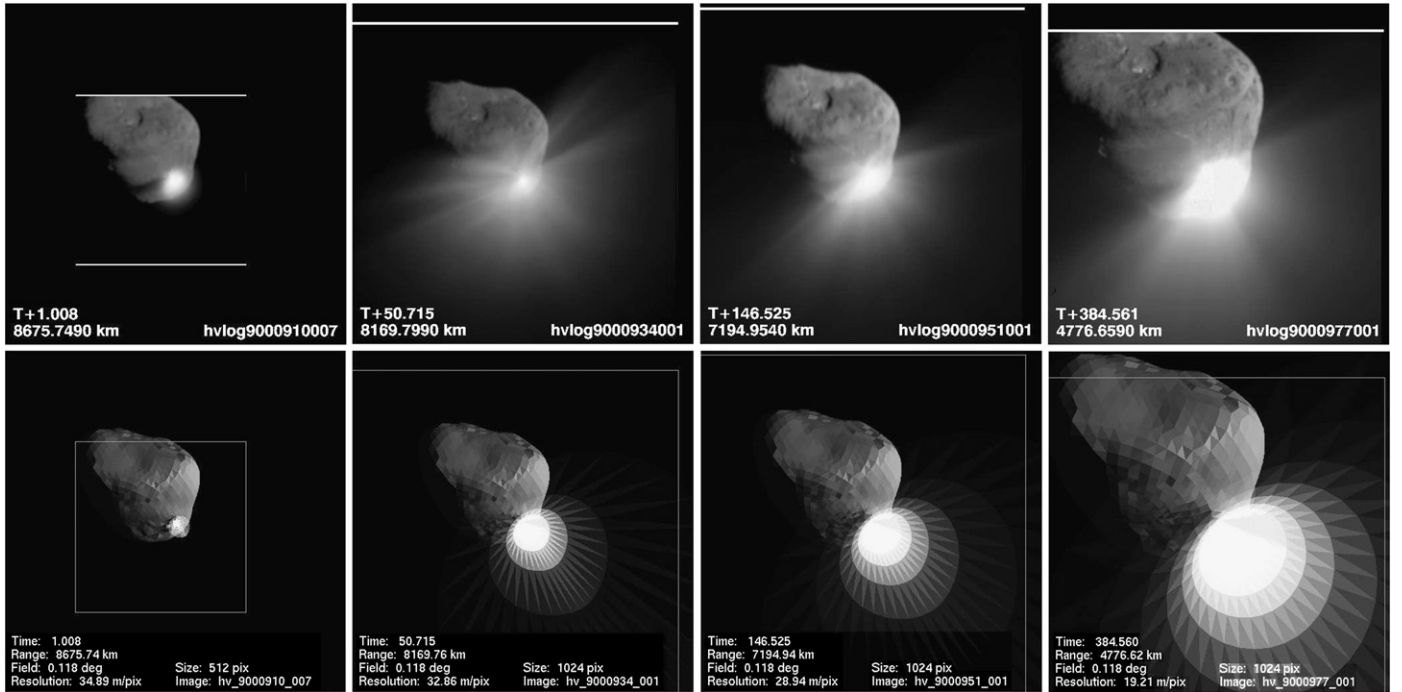


Fig. 21. Deep Impact image sequence, part 1: a comparison between the actual HRI image sequence (*upper images*) and the best-fit modeled image sequence (*lower images*), using a Spitzer-based particle distribution (Lisse et al., 2006). The two pairs of images on the left show the early interior view of the ejecta plume (phase 1), while the two pairs of images on the right show a near edge-on view of the plume’s west (upper left) side (phase 2).

thick zone of the coma and decouple fully from the nucleus outflow. Also note that sublimation of water ice from the ejecta blanket around the impact crater (Section 4.4.4) would appear to act like impact-induced activity from the crater itself, so care in identifying the correct source is necessary. Barring additional evidence to the contrary, impact-induced cometary activity is not considered to have had a significant effect on the observed ejecta plume behavior.

## 5. Conclusion

In the process of this work, we felt it important to keep our model conservative with regard to the number of model parameters, self-consistent throughout, and well grounded theoretically: from the application of the  $\pi$  group scaling relationships for crater volume and formation time (Section 1.3), to the application of the Maxwell Z-model of excavation flow (Section 2.1), to the development of constants for the ejecta velocity scaling relationships (Section 2.2), to the addition of gravity and strength affects to the model (Section 2.3), and finally to the empirically-based determination of ejecta launch angles (Sections 2.4 and 2.5). Throughout its development, the number of experimentally determined constant values used by the model has been kept to a minimum, making use only of constants which are widely accepted and applicable to a wide range of impact environments (Table 2). At each point possible, we have checked our model against previous work and the ejecta behavior recorded in recent experimental studies (Figs. 9–11).

Following model development, our stated goal in Section 1 was to adjust the parameters of this model (over many iterations) to match the flyby-spacecraft observations of the ac-

tual plume behavior, image by image. Figs. 21 and 22 show eight examples from the final HRI image-sequence simulation, using the nominal model inputs from Table 2 and the determined model parameters listed in Table 4. Also included is the Spitzer-based particle size distribution (PSD) from Lisse et al. (2006). The result is a synthetic image sequence which agrees quite well with the actual image sequence, despite the fact that second-order effects, such as gaps and rays in the ejecta plume, have not been included: the ejecta plume goes smoothly through all four viewing phases initially introduced in Fig. 1. While further refinements could be made, particularly in the area of ejecta plume opacity, the first-order match between actual and synthetic image sets is sufficient to meet the goals of this study.

This modeling exercise has indicated that Deep Impact produced a reasonably “well-behaved” oblique-impact cratering event: one in which the impactor–spacecraft apparently struck a small, westward-facing slope of roughly 1/3–1/2 the size of the final crater produced (determined from the initial ejecta plume geometry), and possessing an effective yield strength of not more than  $\bar{Y} = 1\text{--}10$  kPa (estimated via two different methods). The resulting ejecta plume followed well-established scaling relationships for cratering in a medium-to-high porosity target material, consistent with a transient crater of not more than 85–140 m diameter, formed in not more than 250–550 s, for the case of  $\bar{Y} = 0$  Pa (gravity-dominated cratering), and not less than 22–26 m diameter, formed in not less than 1–3 s, for the case of  $\bar{Y} = 10$  kPa (strength-dominated cratering). At  $\bar{Y} = 0$  Pa, an upper limit to the total ejected mass of  $1.8 \times 10^7$  kg ( $1.5\text{--}2.2 \times 10^7$  kg) is consistent with measurements made via long-range remote sensing, after taking into account that 90% of this mass would have stayed close to the

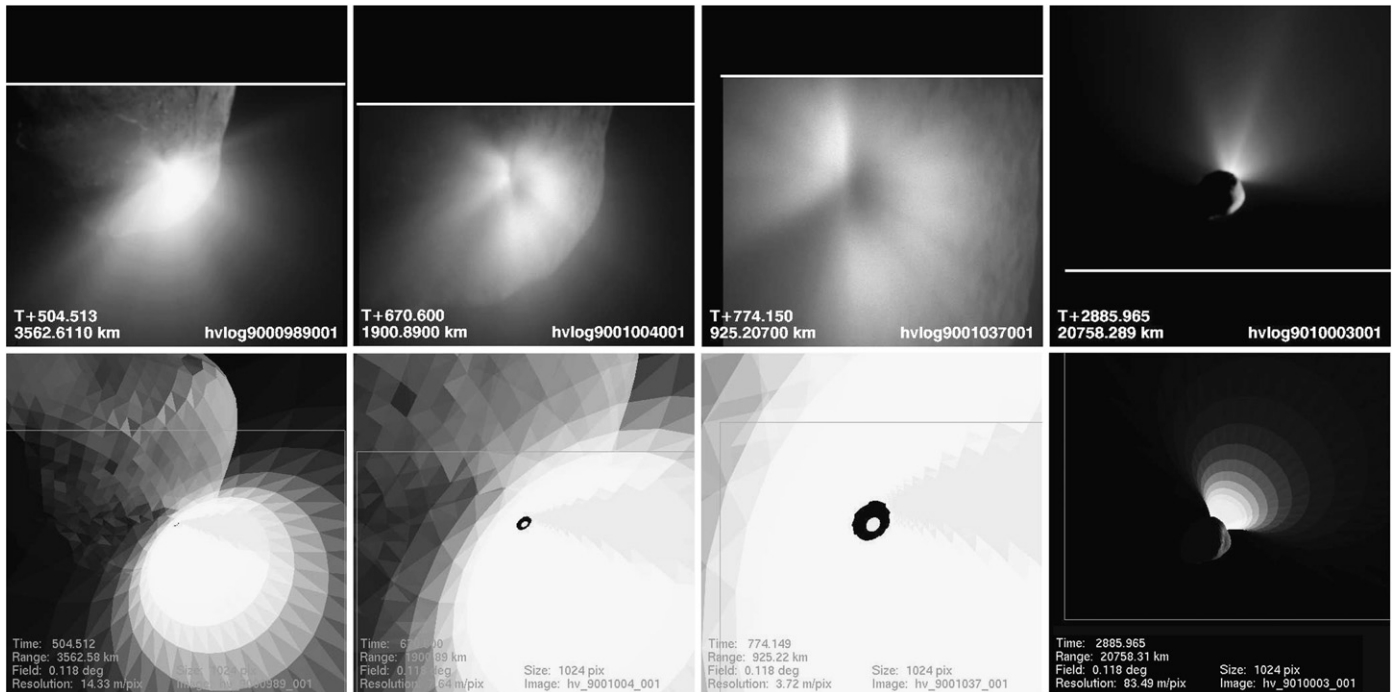


Fig. 22. Deep Impact image sequence, part 2: a comparison between the actual HRI image sequence (*upper images*) and the best-fit modeled image sequence (*lower images*), using a Spitzer-based particle distribution (Lisse et al., 2006). The first pair of images on the left show the beginning of the transition from an edge-on view of the plume's west side (phase 2) to the late interior view of the plume's dark, oval base (phase 3): which is shown in the middle two pairs of images. The small gray circle near the center of the middle two synthetic images marks the position of the impact crater, which the actual (upper) images failed to resolve due to obscuring dust. The final pair of images on the right show the beginning of the look-back phase of observations (phase 4).

surface and then landed within 45 min after the time of impact. However, at  $\bar{Y} = 10$  kPa, a lower limit to the total ejected mass of  $2.3 \times 10^5$  kg ( $1.5\text{--}2.9 \times 10^5$  kg) is also consistent with the remote sensing measurements—making this result somewhat ambiguous. The expansion rate of the ejecta plume imaged during the look-back phase of observations leads to an estimate of the comet's mean surface gravity of  $\bar{g} = 0.34$  mm s $^{-2}$  ( $0.17\text{--}0.90$  mm s $^{-2}$ ), which corresponds to a comet mass of  $m_t = 4.5 \times 10^{13}$  kg ( $2.3\text{--}12.0 \times 10^{13}$  kg) and a bulk density of  $\rho_t = 400$  kg m $^{-3}$  ( $200\text{--}1000$  kg m $^{-3}$ ), consistent with the bulk densities estimated for other cometary nuclei, and where the high-end error is due to uncertainties in the magnitude of coma gas pressure effects on the impact ejecta particles in flight (Section 4.4.2). These results are summarized in Table 4.

However, this work is a mathematical model of a physical phenomena, and as such, it is important to keep in mind the assumptions that have gone into creating it: (1) the crater volume follows the point-source assumption inherent in the  $\pi$  group scaling relationships; (2) the  $\pi$  group scaling relationships can be extended, reasonably well, into the realm of strength-dominated cratering in porous target materials for small impacts which produce simple craters; (3) the cratering event follows the Maxwell Z-model of excavation flow to first-order; and (4) the target material produces particle ejection angles which are consistent with those produced by experimental impacts into granular target materials, at both normal- and oblique-incidence. As with any such model, it is possible to find cases where the model breaks down: where its inherent assumptions have been pushed too far. Of particular relevance to this work is

that our current understanding of the impact cratering process in highly porous targets, or targets possessing strength (particularly “weak” strength), is just at its beginning stages, and much more theoretical and experimental work needs to be done in this area. In that respect, it was somewhat surprising to the authors that the cratering event produced by Deep Impact could be modeled as well as it can be—that the theory we have now works as well as it does. Nonetheless, there are still many aspects of this event which are not understood, such as: what can we learn from the prominent rays and gaps in the ejecta plume? How can the strength of the target at the impact site be constrained further? Are there further temporal variations in the ejecta plume which reflect additional spatial variations at the impact site (such as layering)? What further role did volatiles play in modifying the evolution of the impact ejecta plume? And, how can we better constrain the affects on the evolution of the ejecta plume specifically due to the comet nucleus environment? Even with a good first-order understanding of the Deep Impact event, which we believe we have reached with this work, there is still much to be learned.

## Acknowledgments

The authors would like to sincerely thank Keith Holsapple, Paul Weissman, and Mark Boslough for their patience and insightful reviews of this (large) work. They have helped to make this a much better analysis and presentation than it was initially, and we have learned much in the process. We would also like



to thank Garrett Elliot for his assistance with the initial image processing and data reduction necessary for this analysis.

## References

- A'Hearn, M.F., Belton, M.J.S., Delamere, A., Blume, W.H., 2005a. Deep Impact: A large-scale active experiment on a cometary nucleus. *Space Sci. Rev.* 117, 1–21.
- A'Hearn, M.F., Belton, M.J.S., Delamere, W.A., Kissel, J., Klaasen, K.P., McFadden, L.A., Meech, K.J., Melosh, H.J., Schultz, P.H., Sunshine, J.M., Thomas, P.C., Veverka, J., Yeomans, D.K., Baca, M.W., Busko, I., Crockett, C.J., Collins, S.M., Desnoyer, M., Eberhardy, C.A., Ernst, C.M., Farnham, T.L., Feaga, L., Groussin, O., Hampton, D., Ipatov, S.I., Li, J.-Y., Lindler, D., Lisse, C.M., Mastrodemos, N., Owen, W.M., Richardson, J.E., Wellnitz, D.D., White, R.L., 2005b. Deep Impact: Excavating Comet Tempel 1. *Science* 310, 258–264.
- Anderson, J.L.B., Schultz, P.H., Heineck, J.T., 2003. Asymmetry of ejecta flow during oblique impacts using three-dimensional particle image velocimetry. *J. Geophys. Res.* 108 (E8), doi:10.1029/2003JE002075.5094.
- Anderson, J.L.B., Schultz, P.H., Heineck, J.T., 2004. Experimental ejection angles for oblique impacts: Implications for the subsurface flow-field. *Meteorit. Planet. Sci.* 39, 303–320.
- Asphaug, E., Melosh, H.J., 1993. The Stickney impact of PHOBOS—A dynamical model. *Icarus* 101, 144–164.
- Austin, M.G., Thomsen, J.M., Ruhl, S.F., Orphal, D.L., Schultz, P.H., 1980. Calculational investigation of impact cratering dynamics: Material motions during the crater growth period. *Lunar Planet. Sci.* 11, 46–48.
- Austin, M.G., Thomsen, J.M., Ruhl, S.F., Orphal, D.L., Borden, W.F., Larson, S.A., Schultz, P.H., 1981. Z-model analysis of impact cratering—An overview. In: Merrill, R.B., Schultz, P.H. (Eds.), *Multi-Ring Basins: Formation and Evolution*, Proceedings of the Lunar Planetary Science Conference, Houston, TX, November 10–12, 1980, Pergamon Press, New York, pp. 197–205.
- Bauer, J.M., Weissman, P.R., Choi, Y.-J., Troy, M., Young, J.W., Lisse, C.M., Dekany, R., Hanner, M.S., Buratti, B.J., 2007. Palomar and Table Mountain observations of 9P/Tempel 1 during the Deep Impact encounter: First results. *Icarus* 187, 296–305.
- Buckingham, E., 1914. On physically similar systems; illustrations of the use of dimensional equations. *Phys. Rev.* 4 (4), 345–376.
- Busko, I., Lindler, D., A'Hearn, M.F., White, R.L., 2007. Searching for the Deep Impact crater on Comet 9P/Tempel 1 using image processing techniques. *Icarus* 187, 56–68.
- Chamberlain, J.W., Hunten, D.M., 1987. *Theory of Planetary Atmospheres*. Academic Press, San Diego.
- Chapman, C.R., McKinnon, W.B., 1986. Cratering of planetary satellites. In: Burns, J.A., Matthews, M.S. (Eds.), *Satellites*, Univ. of Arizona Press, Tucson, pp. 492–580.
- Cintala, M.J., Berthoud, L., Horz, F., 1999. Ejection-velocity distributions from impacts into coarse-grained sand. *Meteorit. Planet. Sci.* 34, 605–623.
- Collins, G.S., Wünnemann, K., 2007. Numerical modeling of impact ejection processes in porous targets. *Lunar Planet. Sci.* 38, 1789.
- Croft, S.K., 1980. Cratering flow fields—Implications for the excavation and transient expansion stages of crater formation. *Lunar Planet. Sci.* 11, 2347–2378.
- Croft, S.K., 1981. The excavation stage of basin formation—A qualitative model. In: Merrill, R.B., Schultz, P.H. (Eds.), *Multi-Ring Basins: Formation and Evolution*, Proceedings of the Lunar Planetary Science Conference, Houston, TX, November 10–12, 1980, Pergamon Press, New York, pp. 207–225.
- Davidsson, B.J.R., Gutiérrez, P.J., 2004. Estimating the nucleus density of Comet 19P/Borrelly. *Icarus* 168, 392–408.
- Davidsson, B.J.R., Gutiérrez, P.J., 2006. Non-gravitational force modeling of Comet 81P/Wild 2. *Icarus* 180, 224–242.
- Davidsson, B.J.R., Gutiérrez, P.J., Rickman, H., 2007. Nucleus properties of Comet 9P/Tempel 1 estimated from non-gravitational force modeling. *Icarus* 187, 306–320.
- Dienes, J.K., Walsh, J.M., 1970. Theory of impact: Some general principles and the method of Eulerian codes. In: Kinslov, K. (Ed.), *High-Velocity Impact Phenomena*. Academic Press, New York, pp. 1–579.
- Durda, D.D., 2004. Ejecta generation and redistribution on 433 Eros: Modeling ejecta launch conditions. *Lunar Planet. Sci.* 35, 1096.
- Elbeshausen, D., Wünnemann, K., Collins, G.S., 2007. Three-dimensional numerical modeling of oblique impact processes: Scaling of cratering efficiency. *Lunar Planet. Sci.* 38, 1952.
- Farnham, T.L., Cochran, A.L., 2002. A McDonald Observatory study of Comet 19P/Borrelly: Placing the Deep Space 1 observations into a broader context. *Icarus* 160, 398–418.
- Fernández, Y.R., Lisse, C.M., Kelley, M.S., Dello Russo, N., Tokunaga, A.T., Woodward, C.E., Wooden, D.H., 2007. Near-infrared light curve of Comet 9P/Tempel 1 during Deep Impact. *Icarus* 187, 220–227.
- Finson, M.L., Probst, R.F., 1968. A theory of dust comets. I. Model and equations. *Astrophys. J.* 154, 353–380.
- Gault, D.E., Wedekind, J.A., 1978. Experimental studies of oblique impact. *Lunar Planet. Sci.* 9, 374–376.
- Geissler, P., Petit, J., Durda, D.D., Greenberg, R., Bottke, W., Nolan, M., Moore, J., 1996. Erosion and ejecta reaccretion on 243 Ida and its moon. *Icarus* 120, 140–157.
- Grady, D.E., Kipp, M.E., 1987. Dynamic rock fragmentation. In: Atkinson, B.K. (Ed.), *Fracture Mechanics of Rock*. Academic Press, London, pp. 429–475.
- Groussin, O., A'Hearn, M.F., Li, J.-Y., Thomas, P.C., Sunshine, J.M., Lisse, C.M., Meech, K.J., Farnham, T.L., Feaga, L.M., Delamere, W.A., 2007. Surface temperature of the nucleus of Comet 9P/Tempel 1. *Icarus* 187, 16–25.
- Hampton, D.L., Baer, J.W., Huisjen, M.A., Varner, C.C., Delamere, A., Wellnitz, D.D., A'Hearn, M.F., Klaasen, K.P., 2005. An overview of the instrument suite for the Deep Impact mission. *Space Sci. Rev.* 117, 43–93.
- Harker, D.E., Woodward, C.E., Wooden, D.H., 2005. The dust grains from 9P/Tempel 1 before and after the encounter with Deep Impact. *Science* 310, 278–280.
- Holsapple, K.A., 1993. The scaling of impact processes in planetary sciences. *Annu. Rev. Earth Planet. Sci.* 21, 333–373.
- Holsapple, K.A., Housen, K.R., 2007. A crater and its ejecta: An interpretation of Deep Impact. *Icarus* 187, 345–356.
- Holsapple, K.A., Schmidt, R.M., 1980. On the scaling of crater dimensions. I. Explosive processes. *J. Geophys. Res.* 85, 7247–7256.
- Holsapple, K.A., Schmidt, R.M., 1982. On the scaling of crater dimensions. II. Impact processes. *J. Geophys. Res.* 87, 1849–1870.
- Holsapple, K.A., Schmidt, R.M., 1987. Point source solutions and coupling parameters in cratering mechanics. *J. Geophys. Res.* 92, 6350–6376.
- Housen, K.R., Holsapple, K.A., 2003. Impact cratering on porous asteroids. *Icarus* 163, 102–119.
- Housen, K.R., Schmidt, R.M., Holsapple, K.A., 1983. Crater ejecta scaling laws—Fundamental forms based on dimensional analysis. *J. Geophys. Res.* 88 (17), 2485–2499.
- Keller, H.U., Jorda, L., Küppers, M., Gutiérrez, P.J., Hviid, S.F., Knollenberg, J., Lara, L.-M., Sierks, H., Barbieri, C., Lamy, P., Rickman, H., Rodrigo, R., 2005. Deep Impact observations by OSIRIS onboard the Rosetta spacecraft. *Science* 310, 281–283.
- Keller, H.U., Küppers, M., Fornasier, S., Gutiérrez, P.J., Hviid, S.F., Jorda, L., Knollenberg, J., Lowry, S.C., Rengel, M., Bertini, I., Cremonese, G., Ip, W.-H., Koschny, D., Kramm, R., Kürt, E., Lara, L.-M., Sierks, H., Thomas, N., Barbieri, C., Lamy, P., Rickman, H., Rodrigo, R., A'Hearn, M.F., Angrilli, F., Barucci, M.-A., Bertaux, J.-L., de Deppo, V., Davidsson, B.J.R., de Cecco, M., Debei, S., Fulle, M., Gliem, F., Groussin, O., Lopez Moreno, J.J., Marzari, F., Naletto, G., Sabau, L., Sanz Andrés, A., Wenzel, K.-P., 2007. Observations of Comet 9P/Tempel 1 around the Deep Impact event by the OSIRIS cameras onboard Rosetta. *Icarus* 187, 87–103.
- Knight, M.M., Walsh, K.J., A'Hearn, M.F., Swaters, R.A., Zauderer, B.A., Samarasinha, N.H., Vázquez, R., Reitsema, H., 2007. Ground-based visible and near-IR observations of Comet 9P/Tempel 1 during the Deep Impact encounter. *Icarus* 187, 199–207.
- Küppers, M., Bertini, I., Fornasier, S., Gutiérrez, P.J., Hviid, S.F., Jorda, L., Keller, H.U., Knollenberg, J., Koschny, D., Kramm, R., Lara, L.-M., Sierks,

- H., Thomas, N., Barbieri, C., Lamy, P., Rickman, H., Rodrigo, R., A'Hearn, M.F., Angrilli, F., Bailey, M.E., Barthol, P., Barucci, M.A., Bertaux, J.-L., Burns, J.A., Cremonese, G., Curdt, W., De Cecco, M., Debei, S., Fulle, M., Gliem, F., Ip, W.-H., Kürt, E., Llebaria, A., Lopez Moreno, J.J., Marzari, F., Naletto, G., Sabau, L., Sanz Andrés, A., Sivan, J.P., Tondello, G., Wenzel, K.-P., 2005. A large dust/ice ratio in the nucleus of Comet 9P/Tempel 1. *Nature* 437, 987–990.
- Lamy, P.L., Toth, I., Davidsson, B.J.R., Groussin, O., Gutiérrez, P., Jorda, L., Kaasalainen, M., Lowry, S.C., 2007. A portrait of the nucleus of Comet 67P/Churyumov–Gerasimenko. *Space Sci. Rev.* 128, 23–66.
- Larson, E.E., 1977. *The Relationship of Rock Properties to Explosive Energy Coupling*, UCRL-52204. University of California Research Labs, New York.
- Lisse, C.M., A'Hearn, M.F., Hauser, M.G., Kelsall, T., Lien, D.J., Moseley, S.H., Reach, W.T., Silverberg, R.F., 1998. Infrared observations of comets by COBE. *Astrophys. J.* 496, 971–991.
- Lisse, C.M., A'Hearn, M.F., Groussin, O., Fernández, Y.R., Belton, M.J.S., van Cleve, J.E., Charmandaris, V., Meech, K.J., McGleam, C., 2005. Rotationally resolved 8–35 micron Spitzer Space Telescope observations of the nucleus of Comet 9P/Tempel 1. *Astrophys. J.* 625, L139–L142.
- Lisse, C.M., VanCleve, J., Adams, A.C., A'Hearn, M.F., Fernández, Y.R., Farnham, T.L., Armus, L., Grillmair, C.J., Ingalls, J., Belton, M.J.S., Groussin, O., McFadden, L.A., Meech, K.J., Schultz, P.H., Clark, B.C., Feaga, L.M., Sunshine, J.M., 2006. Spitzer spectral observations of the Deep Impact ejecta. *Science* 313, 635–640.
- Mason, K.O., Chester, M., Cucchiara, A., Gronwall, C., Grupe, D., Hunsberger, S., Jones, G.H., Koch, S., Nousek, J., O'Brien, P.T., Racusin, J., Roming, P., Smith, P., Wells, A., Willingale, R., Branduardi-Raymont, G., Gehrels, N., 2007. Swift ultraviolet photometry of the Deep Impact encounter with Comet 9P/Tempel 1. *Icarus* 187, 123–131.
- Maxwell, D., Seifert, K., 1974. Modeling of cratering, close-in displacements, and ejecta. Report DNA 3628F, Defense Nuclear Agency, Washington, DC.
- Maxwell, D.E., 1977. Simple Z model of cratering, ejection, and overturned flap. In: Roddy, D.J., Pepin, R.O., Merrill, R.B. (Eds.), *Impact and Explosion Cratering*. Pergamon, Elmsford, NY, pp. 1003–1008.
- McEwen, A.S., 1991. Photometric functions for photoclinometry and other applications. *Icarus* 92, 298–311.
- Melosh, H.J., 1989. *Impact Cratering: A Geologic Process*. Oxford Univ. Press, New York.
- Melosh, H.J., 2001. Gravitational modification of ejecta curtain expansion. *Lunar Planet. Sci.* 32, 2135.
- Melosh, H.J., Ryan, E.V., Asphaug, E., 1992. Dynamic fragmentation in impacts—Hydrocode simulation of laboratory impacts. *J. Geophys. Res.* 97, 14735–14759.
- Melosh, H.J., A'Hearn, M.F., Belton, M.J.S., Delamere, W.A., Kissel, J., Klaasen, K.P., McFadden, L.A., Meech, K.J., Schultz, P.H., Sunshine, J.M., Thomas, P.C., Veverka, J., Yeomans, D.K., Baca, M.W., Busko, I., Crockett, C.J., Collins, S.M., Desnoyer, M., Eberhardy, C.A., Ernst, C.M., Farnham, T.L., Feaga, L., Groussin, O., Hampton, D., Ipatov, S.I., Li, J.-Y., Lindler, D., Lisse, C.M., Mastrodemos, N., Owen, W.M., Richardson, J.E., Wellnitz, D.D., White, R.L., 2006. Deep Impact: The first second. *Lunar Planet. Sci.* 37, 1165.
- Milani, G.A., Szabó, G.M., Sostero, G., Trabatti, R., Ligustri, R., Nicolini, M., Facchini, M., Tirelli, D., Carosati, D., Vinante, C., Higgins, D., 2007. Photometry of Comet 9P/Tempel 1 during the 2004/2005 approach and the Deep Impact module impact. *Icarus* 187, 276–284.
- Nolan, M.C., Asphaug, E., Melosh, H.J., Greenberg, R., 1996. Impact craters on asteroids: Does gravity or strength control their size? *Icarus* 124, 359–371.
- Pierazzo, E., Melosh, H.J., 2000. Understanding oblique impacts from experiments, observations, and modeling. *Annu. Rev. Earth Planet. Sci.* 28, 141–167.
- Press, W.H., Teukolsky, S.A., Vetterling, W.T., Flannery, B.P., 1992. *Numerical Recipes in FORTRAN 77*. Cambridge Univ. Press, Cambridge.
- Richardson, J.E., Melosh, H.J., Artemeiva, N.A., Pierazzo, E., 2005. Impact cratering theory and modeling for the Deep Impact mission: From mission planning to data analysis. *Space Sci. Rev.* 117, 241–267.
- Schleicher, D.G., Barnes, K.L., Baugh, N.F., 2006. Photometry and imaging results for Comet 9P/Tempel 1 and Deep Impact: Gas production rates, postimpact light curves, and ejecta plume morphology. *Astron. J.* 131, 1130–1137.
- Schmidt, R.M., Housen, K.R., 1987. Some recent advances in the scaling of impact and explosion cratering. *Int. J. Impact Eng.* 5, 543–560.
- Schultz, P.H., Ernst, C.M., Anderson, J.L.B., 2005. Expectations for crater size and photometric evolution from the Deep Impact collision. *Space Sci. Rev.* 117, 207–239.
- Schultz, P.H., Eberhardy, C.A., Ernst, C.M., A'Hearn, M.F., Sunshine, J.M., Lisse, C.M., 2007. The Deep Impact oblique impact cratering experiment. *Icarus* 190, 295–333.
- Sugita, S., Ootsubo, T., Kadono, T., Honda, M., Sako, S., Miyata, T., Sakon, I., Yamashita, T., Kawakita, H., Fujiwara, H., Fujiyoshi, T., Takato, N., Fuse, T., Watanabe, J., Furusho, R., Hasegawa, S., Kasuga, T., Sekiguchi, T., Kinoshita, D., Meech, K.J., Wooden, D.H., Ip, W.H., A'Hearn, M.F., 2005. Subaru Telescope observations of Deep Impact. *Science* 310, 274–278.
- Sunshine, J.M., Groussin, O., Schultz, P.H., A'Hearn, M.F., Feaga, L.M., Farnham, T.L., Klassen, K.P., 2007. The distribution of water ice in the interior of Comet Tempel 1. *Icarus* 190, 284–294.
- Thomas, P.C., Veverka, J., A'Hearn, M.F., McFadden, L., Belton, M.J.S., Sunshine, J.M., 2005. Comet geology with Deep Impact remote sensing. *Space Sci. Rev.* 117, 193–205.
- Thomas, P.C., Veverka, J., Belton, M.J.S., Hidy, A., A'Hearn, M.F., Farnham, T.L., Groussin, O., Li, J.-Y., McFadden, L.A., Sunshine, J., Wellnitz, D., Lisse, C., Schultz, P., Meech, K.J., Delamere, W.A., 2007. The shape, topography, and geology of Tempel 1 from Deep Impact observations. *Icarus* 187, 4–15.
- Thomsen, J.M., Austin, M.G., Ruhl, S.F., Orphal, D.L., Schultz, P.H., 1980a. The detailed application of Maxwell's Z-model to laboratory-scale impact cratering calculations. *LPI Contribution* 414, p. 92.
- Thomsen, J.M., Austin, M.G., Schultz, P.H., 1980b. The development of the ejecta plume in a Laboratory-Scale Impact Cratering Event. *Lunar Planet. Sci.* 11, 1146–1148.
- Turcotte, D.L., Schubert, G., 2002. *Geodynamics*. In: Turcotte, D.L., Schubert, G. (Eds.), *Geodynamics*. Cambridge Univ. Press, Cambridge, UK, ISBN 0521661862, p. 472.
- Weissman, P.R., Asphaug, E., Lowry, S.C., 2004. Structure and density of cometary nuclei. In: Feston, M.C., Keller, H.U., Weaver, A. (Eds.), *Comets II*. Univ. of Arizona Press, Tucson, pp. 337–357.
- Werner, R.A., 1994. The gravitational potential of a homogeneous polyhedron or don't cut corners. *Celest. Mech. Dynam. Astron.* 59, 253–278.
- Wünnemann, K., Collins, G.S., Melosh, H.J., 2006. A strain-based porosity model for use in hydrocode simulations of impacts and implications for transient crater growth in porous targets. *Icarus* 180, 514–527.